THE $^{16}O + ^{16}O$ REACTION

Thesis by

Harold Spinka

In Partial Fulfillment of the Requirements

for the Degree of

Doctor of Philosophy

California Institute of Technology

Pasadena, California

1971

(Submitted November 23, 1970)

ACKNOWLEDGMENTS

I would like to thank the Kellogg Radiation Laboratory faculty, staff and graduate students for assistance and encouragement during this research. I am thankful to Professor W.A. Fowler and Drs. J.W. Truran and W.D. Arnett for their interest and insight into the astrophysical aspects of the problem. I would also like to express my gratitude to Professor T.A. Tombrello for his supervision and suggestions and to Dr. J.R. Patterson for his help in the early stages of the experiments.

I am especially indebted to Dr. Hubert Winkler for his active and enthusiastic participation in all phases of this work.

Finally, I wish to gratefully acknowledge the financial assistance from the National Science Foundation during my graduate studies. This research was supported in part by the National Science Foundation (GP - 9114, GP - 19887) and the Office of Naval Research (Nonr - 220(47)).

ABSTRACT

The $^{16}O + ^{16}O$ total reaction cross section was measured at six energies between E_{cm} = 6.80 to 11.85 MeV near the astrophysical region of interest. Angular distributions and cross sections for the production of protons, alphas and deuterons were obtained with counter telescopes in a differentially pumped gas target. No ^{3}He or ^{3}H were observed. Cross sections for the formation of ^{31}S and ^{30}P were measured by detecting the betas from their radioactive decays. The angular distribution and cross section for production of neutrons was obtained with a "long counter" at E_{cm} = 12 MeV, demonstrating that the ^{16}O (^{16}O,pn) process accounts for over 90 % of the ^{30}P formed at this energy. The presence of such three body breakup reactions made the experimental determination of the total cross section difficult. Finally, the $^{16}O + ^{16}O \rightarrow ^{12}C$ (g.s.) + ^{20}Ne (g.s.) reaction was studied with a coincidence technique at E_{cm} = 12 MeV.

Gamma spectra were taken at several energies for a number of targets using Ge(Li) counters. Gamma lines from nuclei produced in both two and three body exit channels from $^{16}O + ^{16}O$ reactions were observed. In addition, the gamma yield as a function of bombarding energy was measured in 50 keV (C.M.) steps for both $^{16}O + ^{16}O$ and $^{12}C + ^{12}C$. The $^{16}O + ^{16}O$ gamma yield is smoothly varying, indicating that the $^{16}O + ^{16}O$ reaction cross section does not have large fluctuations with energy similar to the structure seen in

$^{12}C + ^{12}C$ reactions.

Nearly all cross sections were measured relative to the $^{16}O + ^{16}O$ elastic scattering at $\theta_{lab} = 45^{o}$ to avoid the problems with direct current integration of heavy ion beams in gas targets. A new, more precise determination of the elastic scattering cross section at $\theta_{cm} = 90^{o}$ was made for $E_{cm} = 7.3$ to 14.4 MeV in steps of 100 keV (C.M.). A previously unknown anomaly was observed near $E_{cm} = 10.5$ MeV. Elastic scattering cross sections were also obtained for $^{12}C + ^{12}C$ in steps of 60 keV C.M. energy from $E_{cm} = 3.9$ to 8.0 MeV at $\theta_{cm} = 90^{o}$. In both cases, gas mixtures were used in the differentially pumped system as the target.

TABLE OF CONTENTS

INTRODUCTION

The Problem

A study of the $^{16}O + ^{16}O$ reaction was made at energies near and below the Coulomb barrier (E_{cm} = 7 - 12 MeV) because of its possible importance in astrophysics. Cross sections to all exit channels as a function of energy are the quantities of interest for astrophysics, and numerous experimental techniques were employed to measure these cross sections.

The astrophysical interest in this reaction is related to the quest to explain the observed elemental abundances. Nucleosynthesis is presently believed to occur in large bodies of gas (stars, the primeval fireball, etc.). In high temperature regions of these bodies Hydrogen is converted to Helium, Helium to Carbon and Oxygen, and these to heavier elements up to the iron region. Specifically, conditions are currently envisioned ($T \simeq 2 - 4 \times 10^9\ ^oK$, $\rho \sim 10^5 - 10^8\ gm/cm^3$ and time scales of seconds to days) at a certain evolutionary stage in some stars where Oxygen is present in large quantities and burns by $^{16}O + ^{16}O$ nuclear reactions.

Quiescent Oxygen burning in evolved stars was studied by Cameron (1959) and Tsuda (1963). The important exit channels for these calculations and the respective estimated branching ratios were $^{31}S + n$ 10%, $^{31}P + p$ 50%, $^{30}Si + 2p$ 10%, $^{28}Si + \alpha$ 30% at E_{cm} = 5 MeV. (The interaction radius used to compute

the $^{16}O + {}^{16}O$ total reaction cross section varied from 7 to 9 fm.) The physical conditions in the star were a central temperature of $T \sim 1.3 \times 10^9\ ^oK$, a density of $\rho \sim 10^5\ gm/cm^3$ and a time scale of $10^5 - 10^7$ years. The main products of Oxygen burning were the α-nuclei ^{24}Mg, ^{28}Si and ^{32}S.

The inclusion of a number of neutrino formation processes by Fowler and Hoyle (1964a) for temperatures above about $1 \times 10^9\ ^oK$ altered the previous conclusions. Higher burning temperatures are required for quiescent Oxygen burning in order to counterbalance the neutrino energy losses from the star. The particular physical conditions considered were a star of total mass $M \gtrsim 10$ solar masses, temperatures of $T \simeq 2.1 - 3.0 \times 10^9\ ^oK$ and time scales on the order of days. Above $T \sim 3 \times 10^9\ ^oK$ photodisintegration of the Oxygen via $^{16}O(\gamma,\alpha)$ reactions was expected to become important, limiting the temperature range for Oxygen burning. Chiu (1968, 1966) also considered this case for a more massive star ($M \sim 30$ solar masses) and a similar temperature $T \sim 2.5 \times 10^9\ ^oK$. In addition, a number of Oxygen burning stellar models were constructed by Rakavy, Shaviv and Zinamon (see Rakavy (1967a,b,c)).

Truran and Arnett (1970) discussed nucleosynthesis in explosive Oxygen burning as a means of producing elements with $14 \leq Z \leq 20$ from supernovae. They were able to reproduce both the elemental and isotopic abundance features observed in the solar system for these nuclei by assuming densities of $10^5 \lesssim \rho \lesssim 10^6$ gm/cm^3 and a restricted temperature range about $T = 3.6 \times 10^9\ ^oK$.

The time scales were on the order of seconds to minutes. Truran and Arnett speculated that the Oxygen burning might occur in a shell of matter not necessarily at the center of the supernova (see also Arnett (1969a,b)).

Most of these reactions do not occur at $E_{cm} = kT \simeq 250$ keV because the cross section at this energy is extremely small. Instead, the majority take place near E_o, which is the energy at the maximum of the product

$$\left(\begin{array}{c}\text{Maxwell-Boltzmann distribution} \\ \text{of } {}^{16}O \text{ energies}\end{array}\right) \cdot \left(\begin{array}{c}\text{Coulomb barrier penetration} \\ \text{factor for } {}^{16}O + {}^{16}O\end{array}\right)$$

The full energy width at $1/e$ maximum of the distribution of the number of reactions occurring is Δ (see Fowler and Vogl (1964b) or Fowler, Caughlan and Zimmerman (1967)). For ${}^{16}O + {}^{16}O$ reactions at $T = 3 \times 10^9\ ^oK$

$$E_o = 8.1 \text{ MeV} \qquad \Delta = 3.4 \text{ MeV}$$

Most astrophysical nuclear reactions have a cross section too small to be measured at or near the corresponding E_o. Consequently, cross sections must be extrapolated down many orders of magnitude to the vicinity of E_o. A very unusual feature of ${}^{16}O + {}^{16}O$ reactions is that they can be measured over part of the energy range where they are important astrophysically. This means that it is not mandatory to have the high precision normally needed for extrapolation of the cross sections to lower energies. It is also quite fortunate

since the large number of open exit channels and the presence of three body breakup reactions make the experimental determination of the total cross section difficult.

The $^{16}O + ^{16}O$ reactions are also interesting from the point of view of nuclear physics. Heavy ion reactions are quite complicated because of the large number of nucleons in both target and projectile. Yet considerable information on nuclear structure of the heavier elements has been derived from heavy ion reaction data. Elastic and inelastic scattering, Ericson fluctuations, transfer reactions and excited state lifetimes are commonly measured. However, few heavy ion reactions have been studied to derive cross sections and angular distributions for all exit channels present. Such a task is monumental at energies far above the Coulomb barrier where there are a large number of open channels, and normally reaction cross section measurements are confined to cases where at least one reaction product is radioactive. A thorough study has been made at sub-Coulomb barrier energies of the $^{12}C + ^{12}C$ system and strong cross section fluctuations were observed (see Almqvist (1960, 1963), Bromley (1960, 1961) and Patterson, Winkler and Zaidins (1969)). Weaker structure has been seen in $^{12}C + ^{16}O$, but none was apparent in the $^{16}O + ^{16}O$ case in the vicinity of the Coulomb barrier. These facts have caused considerable theoretical research to understand the origin of these fluctuations (see Davis (1960), Vogt (1960), Kompaneets (1961), Wildermuth (1961), Imanashi (1969), and Michaud (1969)), and a thorough study of $^{16}O + ^{16}O$

reactions near the Coulomb barrier would be useful to compare with $^{12}C + {}^{12}C$.

The Expected Results

Before discussing the experimental methods, the results will be anticipated using ideas from elementary quantum mechanics and simple compound nucleus theory. This will provide a basis for understanding the experimental methods used and the choice of the various quantities measured.

In astrophysical calculations a cross section variation of the form

$$\sigma(E) \approx \frac{\tilde{S}(E)}{E} \exp(-2\pi\eta - gE),$$

where

$$\eta = \frac{Z_1 Z_2 e^2}{\hbar v_{rel}} \quad \text{and} \quad g = \frac{2}{3\hbar}\sqrt{\frac{2MR^3}{Z_1 Z_2 e^2}}$$

is often assumed. v_{rel} is the relative velocity of the incoming particles, R is the interaction radius, M is the reduced mass, and E is the center-of-mass energy. The relation follows from the WKB approximation for a charged particle with orbital angular momentum $L = 0$ penetrating a Coulomb barrier ($V = Z_1 Z_2 e^2/r$ for $r > R$ and $= 0$ for $r < R$). The factor $\tilde{S}(E)$ contains the energy dependence from purely nuclear effects, as well as from nonnuclear effects not properly taken into account by the exponential.

$\tilde{S}(E)$ is usually assumed to be nearly constant if there are no resonances in the nuclear system. The final measured cross sections are used to obtain $\tilde{S}$ (see the Conclusions Section). However, most of the measurements were made at energies not very far below the Coulomb barrier ($E_{cm} \sim 10.5$ MeV, $R \sim 8.8$ fm), where the exponential factor does not give a good approximation to the barrier penetration energy dependence. Furthermore, for $^{16}O + ^{16}O$ reactions there is a considerable angular momentum involved (classically, $L \simeq 6$ at $E_{cm} = 12$ MeV), so some variation of $\tilde{S}$ with E is not unexpected. Using the equation above, the drop in cross section from $E_{cm} = 10.5$ MeV to the lowest energy measured, $E_{cm} = 7$ MeV, is about a factor of 5000.

The exit channels available to $^{16}O + ^{16}O$ reactions up to $E_{cm} = 12$ MeV are shown in Figure 1. Note that there may be competition between compound nucleus formation and direct reactions. In the former case the 32 nucleons momentarily form ^{32}S, the compound nucleus. The energy becomes spread among the constituent nucleons so that there is no "memory" of the incoming channel. Then one or more particles "evaporate" from the compound nucleus. In the case of direct reactions the ^{32}S intermediate state is not formed. Examples of the latter are perhaps $^{12}C + ^{20}Ne$ (α-transfer) and $^{24}Mg + ^{8}Be$ (2α-transfer). The neutron and proton transfer channels $^{15}O + ^{17}O$ and $^{15}N + ^{17}F$ are open only at the highest bombarding energy used. Buchler (1969) calculated that less than 20% of the total $^{16}O + ^{16}O$ reaction cross section could be accounted

Figure 1

$^{16}O + {}^{16}O$ Exit Channels.

All $^{16}O + {}^{16}O$ exit channels with $Q > -10$ MeV and γ transitions from low lying levels in some residual nuclei are shown. Additional exit channels not illustrated are

$^{28}Si + p + t$	$Q = -10.222$ MeV
$^{29}Si + 2p + n$	-10.229
$^{28}Si + {}^{3}He + n$	-10.985
$^{23}Na + p + 2\alpha$	-12.084

All Q values were computed from the mass table of Mattauch (1965) and the range of energies studied was E_{cm} = 7 to 12 MeV. Levels for the $^{12}C + {}^{20}Ne$ exit channel correspond to excited states in both nuclei.

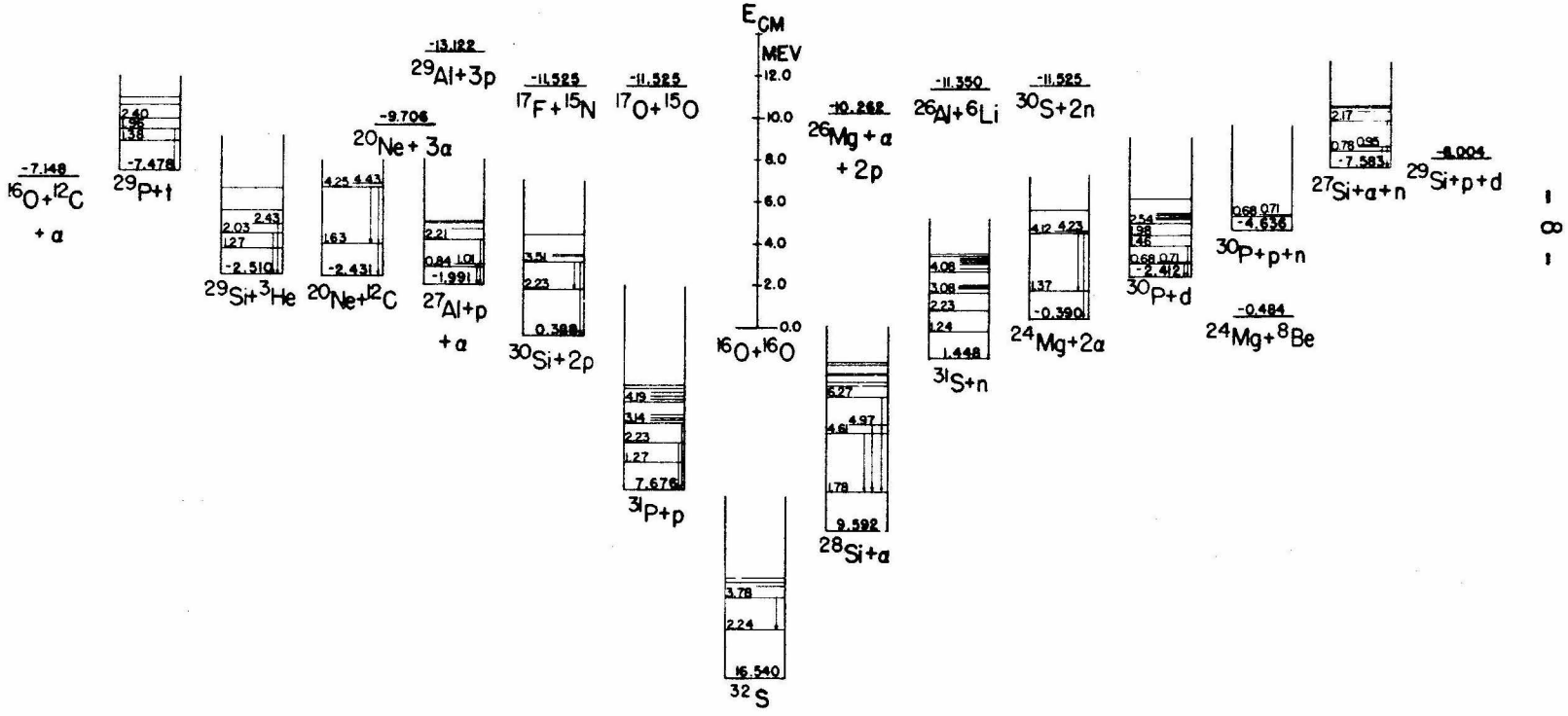
E_CM
MEV
12.0
10.0
8.0
6.0
4.0
2.0
0.0
-7.148
16O+12C
+α
2.40
1.38
-7.478
29P+t
2.43
2.03
1.27
-2.510
29Si+3He
4.25 4.43
1.63
-2.431
20Ne+12C
-9.706
20Ne+3α
-13.122
29Al+3p
2.21
0.84 1.01
-1.991
27Al+p
+α
-11.525
17F+15N
3.51
2.23
0.388
30Si+2p
-11.525
17O+15O
4.19
3.14
2.23
1.27
7.676
31P+p
16O+16O
3.78
2.24
16.540
32S
-10.262
26Mg+α
+2p
6.27
4.97
4.61
1.78
9.592
28Si+α
-11.350
26Al+6Li
4.08
3.08
2.23
1.24
1.448
31S+n
-11.525
30S+2n
4.12 4.23
1.37
-0.390
24Mg+2α
2.54
1.38
1.48
0.68 0.71
-2.412
30P+d
0.68 0.71
-4.636
30P+p+n
-0.484
24Mg+8Be
2.17
0.78 0.95
-7.583
27Si+α+n
-8.004
29Si+p+d

for by the α-transfer channel, so compound nucleus formation is expected to be important.

The energy spectrum of light particles b "evaporating" from the compound nucleus can be estimated from Blatt and Weisskopf (1952)

$$\#(E) \cdot dE = \text{const} \cdot E \cdot \sigma_c(E) \cdot \omega_Y(E_{exc}) \cdot dE$$

Here E_{exc} is the excitation energy of the resulting nucleus Y corresponding to E, the total C.M. kinetic energy of the outgoing particles b + Y. The value of σ_c is the cross section for formation of the compound system by particles b incident on the target nucleus Y and can be expressed in terms of charged particle or neutron penetrabilities. The level density in the nucleus Y was taken to be that of a Fermi gas with angular momentum I = 0:

$$\omega_Y(E_{exc}) = \frac{\text{const}}{E_{exc}^2} \cdot \exp\left(2\sqrt{aE_{exc}}\right),$$

with $a = 4\ \text{MeV}^{-1}$ (see Bohr and Mottelson (1969), especially page 187 and Fig. 2-12). The computed neutron, proton and alpha spectra with thresholds for secondary reactions are shown in Figs. 2 - 4. It is evident that three body breakup reactions may have large cross sections, especially at the higher bombarding energies.

The Coulomb barrier E_{coul} for the mass region $A \sim 30$, $Z \sim 15$ for protons is about 2.5 MeV and for alphas is about 4.5 MeV.

Figures 2 - 4

Neutron, Proton and Alpha Evaporation Spectra

From $^{16}O + ^{16}O$.

The C.M. spectra of light particles emitted from $^{16}O + ^{16}O$ reactions was calculated on the basis of a compound nucleus model at E_{lab} = 16, 20 and 24 MeV (see the text page 9). All particles with energies less than the indicated three body thresholds leave the residual nucleus with sufficient energy to permit a second evaporation.

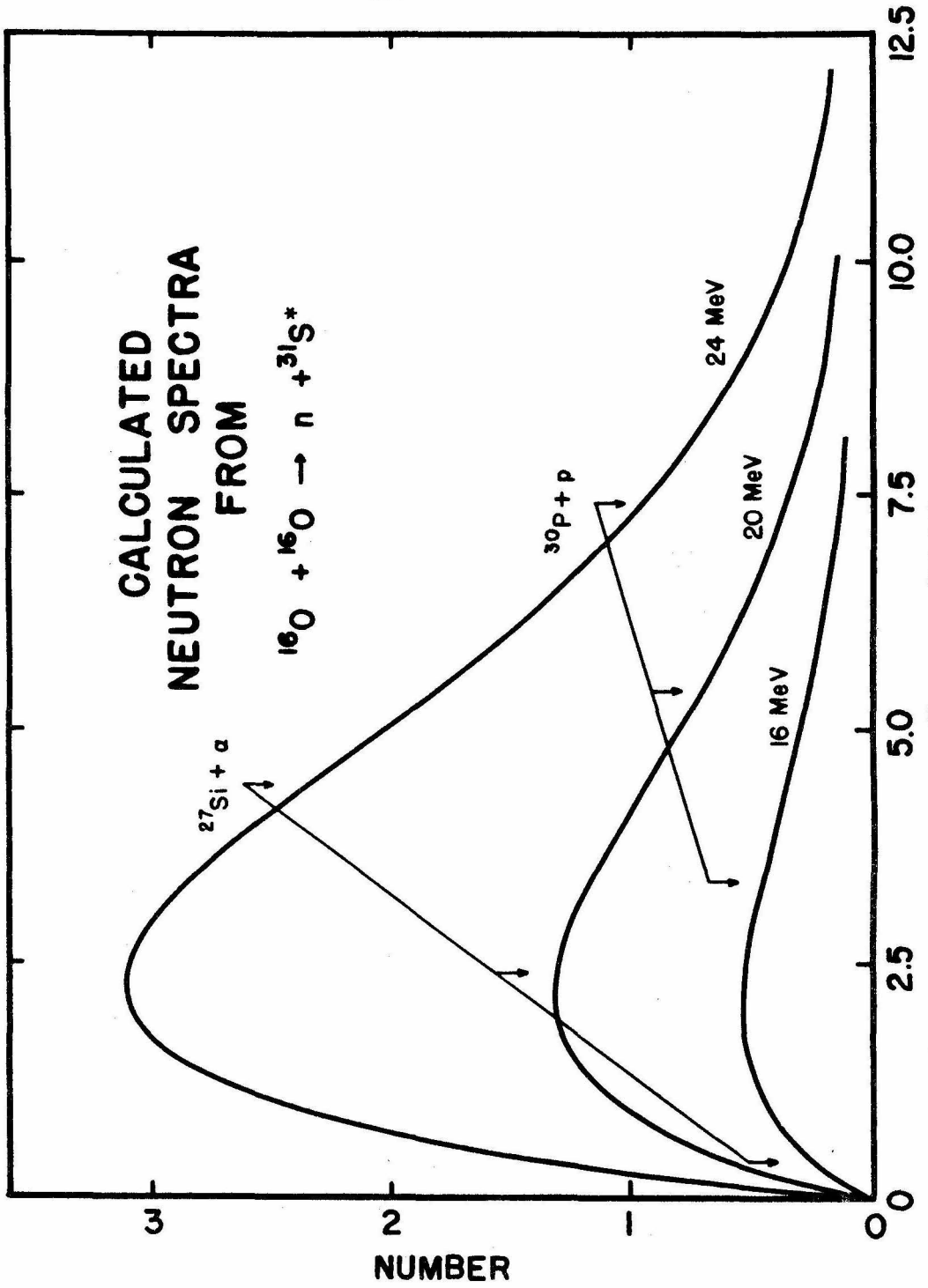
CALCULATED
NEUTRON SPECTRA
FROM
$^{16}O + {}^{16}O \rightarrow n + {}^{31}S^*$
$^{27}Si + \alpha$
$^{30}P + p$
24 MeV
20 MeV
16 MeV
NUMBER
0
1
2
3
0
2.5
5.0
7.5
10.0
12.5
E_{cm} (MeV)

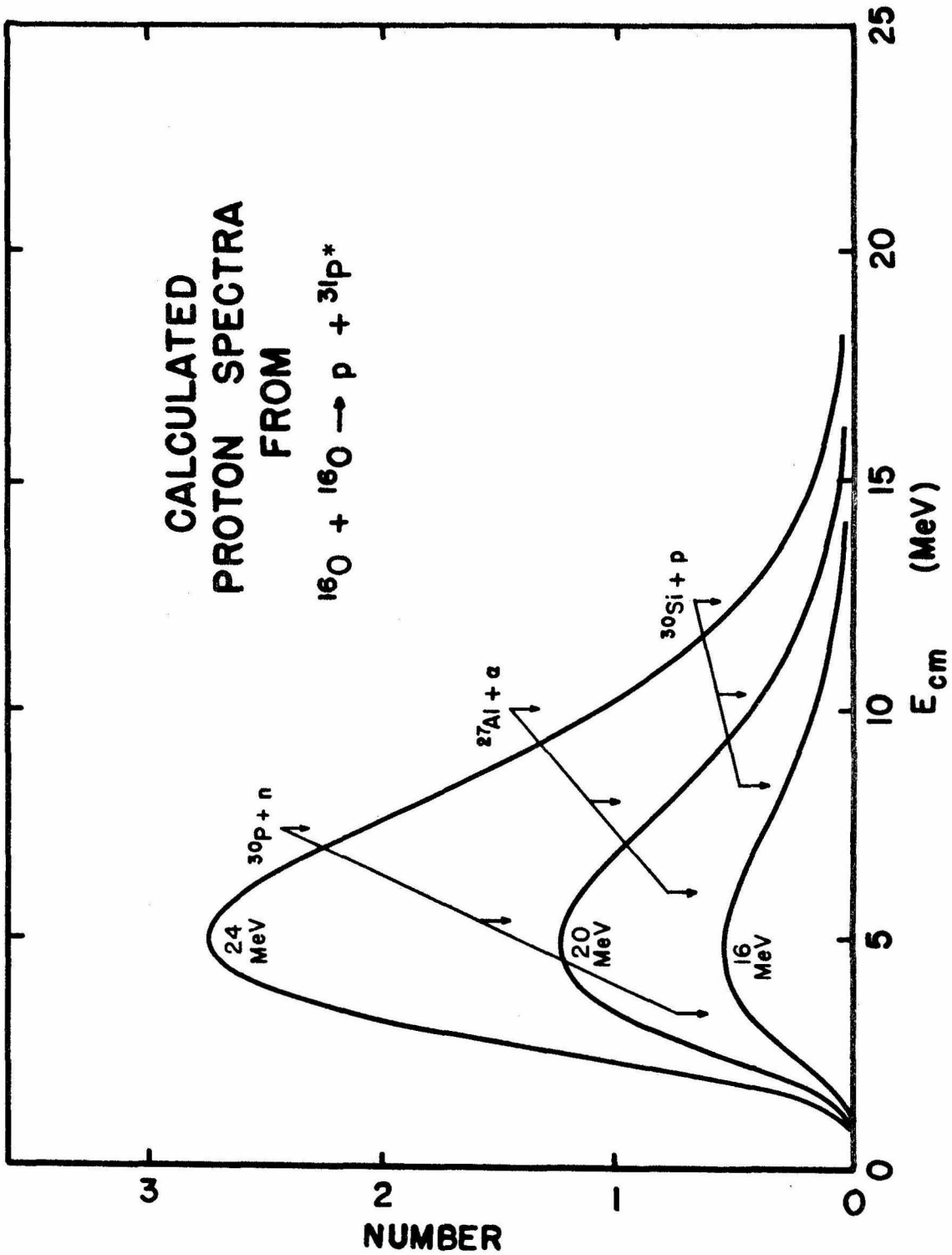
CALCULATED
PROTON SPECTRA
FROM
$^{16}O + {}^{16}O \rightarrow p + {}^{31}P^*$
$^{30}P + n$
$^{27}Al + \alpha$
$^{30}Si + p$
24 MeV
20 MeV
16 MeV
NUMBER
E_{cm} (MeV)
0
1
2
3
5
10
15
20
25

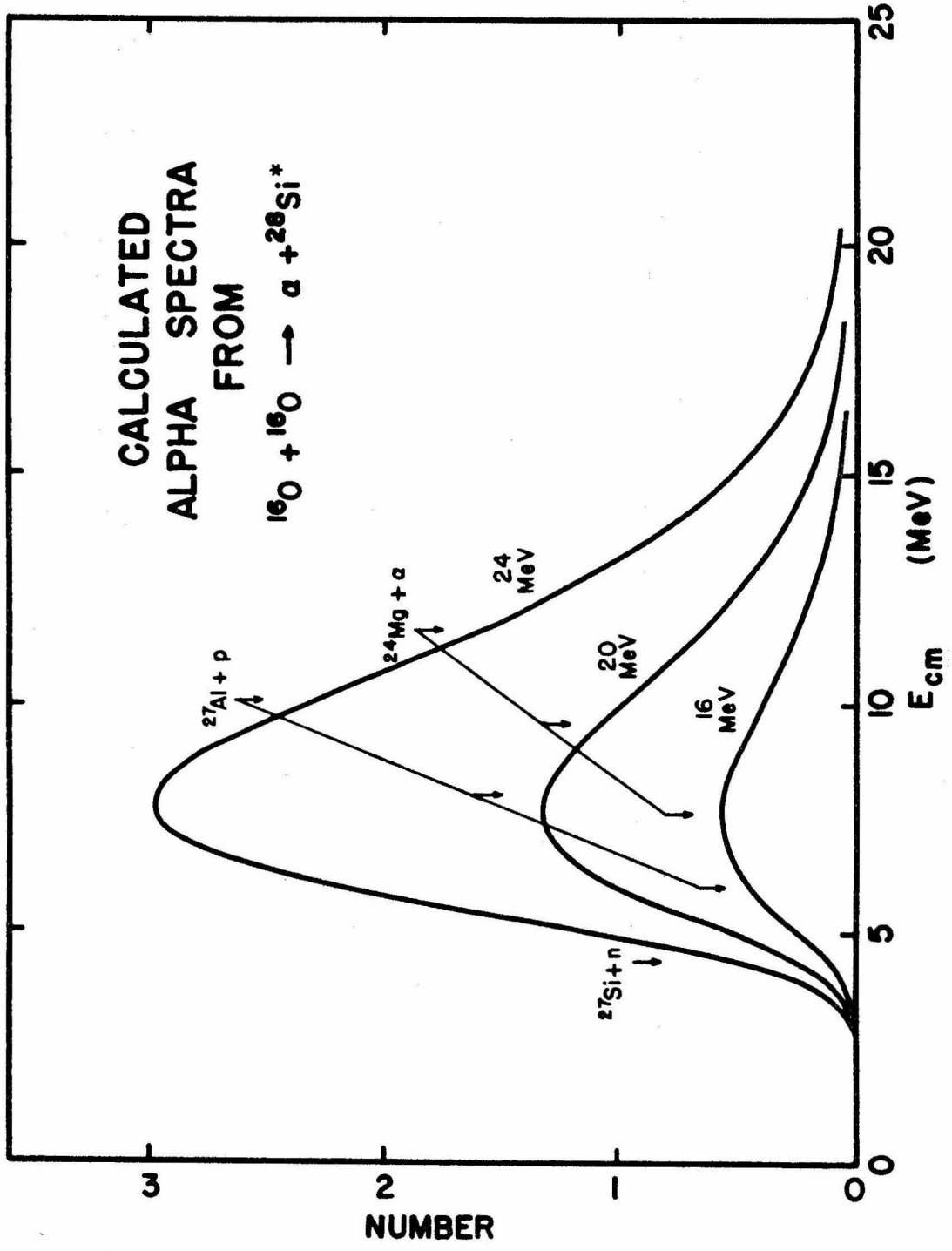
CALCULATED
ALPHA SPECTRA
FROM
$^{16}O + ^{16}O \rightarrow \alpha + ^{28}Si^*$
$^{27}Al + p$
$^{24}Mg + \alpha$
24 MeV
20 MeV
16 MeV
$^{27}Si + n$
NUMBER
E_{cm} (MeV)
0
1
2
3
0
5
10
15
20
25

A useful quantity to compare the different exit channels is $Q_{eff} = Q - E_{coul}$. With these values and the computed particle spectra, the branching ratios can be estimated. The ^{32}S compound nucleus will probably emit roughly equal numbers of protons and alphas (the alphas will compete because the positive Q value is higher for $^{28}Si + \alpha$ than $^{31}P + p$, counterbalancing the larger E_{coul} for alphas -- i.e., $Q_{eff} \sim 5$ MeV for both), with somewhat fewer neutrons ($Q_{eff} \sim 1.5$ MeV), still fewer deuterons, etc. Thus the main nuclei Y left after the first evaporation should be ^{31}P, ^{28}Si, and ^{31}S. Some of these will have an excitation energy above a particle breakup threshold and will generally have a second evaporation. For example, those ^{31}S will go to $^{30}P + p$, and ^{28}Si preferentially to $^{27}Al + p$ and somewhat less to $^{24}Mg + \alpha$, etc. in the same way as before. These arguments based on Q_{eff} suggest the following "branching ratios" for a bombarding energy corresponding to $E_{cm} \sim 12$ MeV:

Exit Channel	Q	Q_{eff}	"B.R."
$^{28}Si + \alpha$	9.592 MeV	+ 5 MeV	lots
$^{31}P + p$	7.676	+ 5	lots
$^{31}S + n$	1.448	+ 1.5	some
$^{30}Si + 2p$	0.388	- 4.5	lots
$^{30}P + d$	- 2.412	- 5	some
$^{29}Si + ^{3}He$	- 2.510	- 7	little
$^{30}P + p + n$	- 4.636	- 7	lots
$^{27}Al + p + \alpha$	- 1.991	- 9	some
$^{24}Mg + 2\alpha$	- 0.390	- 9.5	some
$^{29}P + t$	- 7.478	- 11	very little
$^{12}C + ^{20}Ne$	- 2.431		some (?)
Everything else		<- 11.5	~ none

The Experimental Methods

A large proportion of these exit channels involve one or more light charged particles. Angular distributions and cross sections for the production of protons, deuterons and alphas were measured using counter telescopes. This technique, described in the Charged Particle Section (page 62), provides the bulk of the cross section data.

Two radioactive nuclei, ^{30}P and ^{31}S, were produced by $^{16}O + ^{16}O$ reactions. Cross sections for their production were measured by counting the emitted beta particles as a function of time after the beam was turned off. The decay curves were analyzed using the known halflives to separate the two activities. Experimental details and results are given in the Activation Section (page 109).

A cross check between the previous two methods was afforded by the set of channels

$$^{30}P + d \qquad ^{30}P + p + n \qquad ^{31}S + n .$$

In the Neutrons Section (page 141) is described a determination of the neutron production cross section using a flat response detector. The cross check

$$\sigma(^{30}P) + \sigma(^{31}S) = \sigma(d) + \sigma(n)$$

is established and conclusions on the number of three body reactions are made.

The $^{12}C + ^{20}Ne$ exit channel cannot be studied with the previous techniques. Its branching ratio is hard to estimate theoretically because it may be a direct reaction, yet both $^{16}O + ^{16}O \rightarrow ^{12}C + ^{20}Ne$ and the inverse $^{12}C + ^{20}Ne \rightarrow ^{16}O + ^{16}O$ may be of astrophysical interest. Thus, the angular distribution of the former reaction leading to the ground states of ^{12}C and ^{20}Ne was measured using a coincidence technique (see $^{12}C + ^{20}Ne$ Production Section, page 152). No data on the total cross section to excited states were obtained.

A number of important semiquantitative results were also obtained from the γ's emitted in $^{16}O + ^{16}O$ reactions. The Gammas Section (page 42) presents results which roughly verify the expected branching ratios. In addition, measurements of the total γ emission from $^{16}O + ^{16}O$ were made at narrow energy steps (ΔE_{cm} = 50 keV). No evidence for structure similar to that in the $^{12}C + ^{12}C$ reactions was seen, so large steps in bombarding energy for the reaction cross section measurements were justified.

All cross sections were measured relative to the elastic scattering cross section for $^{16}O + ^{16}O$, because direct current integration of heavy ion beams, especially in gas targets, always presents problems and was completely avoided except for the $^{12}C + ^{20}Ne$ measurements. The $\theta_{cm} = 90^{o}$ relative maximum in the $^{16}O + ^{16}O$ Mott scattering angular distribution provided a convenient and easily reproducible point to use for the normalization. Although there are elastic scattering cross section data at this

angle in the literature, a new, more precise determination was made for E_{cm} = 7.35 - 14.35 MeV. The Elastic Scattering Section (page 18) describes these experiments.

The large number of exit channels and energetically accessible excited states in the reaction products made it very difficult to exclude contaminant reactions. Therefore a differentially pumped gas target of high purity O_2 was used whenever possible. The low target density was partly compensated for by the much higher beam currents possible in an open gas target. Also, energy losses and target uniformity are more easily controlled in such a system. The target design is described in the Elastic Scattering Section (page 21). Several examples of problems that can arise from solid targets are given in the Activation Section.

Finally, two appendixes contain $^{12}C + ^{12}C$ γ ray and elastic scattering data to compare with the $^{16}O + ^{16}O$ case. Striking differences can be seen between Figures 9 and 42 and in Figure 12. The final cross sections are contained in Table 15 of the Conclusions Section.

ELASTIC SCATTERING

Introduction

Some means of determining the number of incident and target nuclei was necessary for measuring $^{16}O + ^{16}O$ reaction cross sections. Direct integration of the beam current is often used to obtain the number of incident particles, but this is difficult for heavy ion beams because of the uncertainty of the beam's charge state distribution after passing through the target. Thus the relationship between the current and the number of particles per second is poorly known. Another solution was to determine the heat deposited by the beam with a calorimeter. However, elastic scattering of the beam from the target region gives a more direct measurement of the combined beam intensity and target thickness. The reaction cross section can be written as

$$\left(\frac{d\sigma}{d\Omega}\right)_{\text{reaction}} \propto \left(\frac{d\sigma}{d\Omega}\right)_{\substack{\text{elastic} \\ \text{scattering}}} \cdot \frac{(\#\text{ reaction products})}{\left(\#\text{ elastically scattered} \atop \text{particles}\right)}$$

with the constant of proportionality depending on geometrical and kinematic factors only. This method was used for determining nearly all the $^{16}O + ^{16}O$ reaction cross sections, requiring a knowledge of the differential cross section for elastic scattering.

The elastically scattered ^{16}O nuclei were always detected at $\theta_{cm} = 90^{\circ}$ ($\theta_{lab} = 45^{\circ}$). This angle was chosen because the Mott

scattering has a relative maximum there for all energies with a differential cross section just four times the Rutherford value, and because the angle could be easily located experimentally. As a test of the differentially pumped gas target system, the elastic scattering of $^{16}O + ^{16}O$ was measured at $\theta_{cm} = 90^{o}$. Our preliminary results disagreed with values in the literature (Bromley (1960, 1961)) near the Coulomb barrier, so more complete data with higher precision were taken.

In these experiments the ^{16}O nuclei were scattered from a mixture of Oxygen and Argon gas and were detected with the same counter and collimation as in the other charged particle measurements. The ratio of $^{16}O + ^{16}O$ elastic scattering to pure Rutherford scattering ($^{16}O + ^{40}Ar$) was obtained from a ratio of counts in the one detector at $\theta_{lab} = 45^{o}$. The difference in the angular distributions for $^{16}O + ^{16}O$ and $^{16}O + ^{40}Ar$ near $\theta_{lab} = 45^{o}$ required special precautions to keep the angle constant and to obtain reproducible data with good statistical accuracy. Data were taken from $E_{cm} = 7.3 - 14.4$ MeV in steps of 100 - 250 keV (C.M.) with O^{4+} and O^{5+} beams of 3 to 7 μa from the CIT - ONR tandem accelerator. The energy distribution of the beam in the target region was estimated to have a FWHM of < 60 keV (C.M.) that arose from target thickness and straggling. The position and incident angle of the beam were continuously monitored. Final data are given in Table 1 and Figure 9. Each data point in the region 9.5 - 11.5 MeV (C.M.) represents 4 to 6 different measurements of at least 40 minutes total counting

time. The results show that the 90^{o} (C.M.) cross section is not as smooth near the Coulomb barrier as formerly thought.

Previous elastic scattering data for $^{16}O + ^{16}O$ were taken by Bromley, Kuehner and Almqvist (1960, 1961) for E_{cm} = 5.0 - 17.5 MeV at angles of $\theta_{cm} = 38^{o}$, 58^{o}, and 90^{o} using a solid target. Over part of this energy range Carter, Stelson, Mehta and Bernard (1965) searched for fast changing structure in the $^{16}O + ^{16}O$ elastic scattering at $\theta_{cm} = 48^{o}$, 58^{o}, 80^{o}, and 90^{o} with a differentially pumped gas target. Carter, et al. reported general agreement with Bromley, but no new absolute differential cross sections were given. At higher energies, E_{cm} = 10 - 35 MeV, Maher, Sachs, Siemssen, Weidinger and Bromley (see Siemssen (1967) and Maher (1969) made measurements of angular distributions and excitation functions and found strong resonance structure.

Recently there has been theoretical interest in the $^{16}O + ^{16}O$ elastic scattering. Rickertsen, Block, Clark and Malik (1969) used a nuclear molecular potential to fit the differential cross sections at $\theta = 49^{o}$, 60^{o}, 70^{o}, 80^{o}, and 90^{o} for E_{cm} = 10 to 22 MeV. Brueckner, Buchler and Kelley (1968) and Chatwin, Eck, Richter and Robson (1969, 1970) tried to fit the 90^{o} excitation function and some angular distributions for E_{cm} = 10 to 15 MeV. In both cases the experimental data of Bromley were used to compare to the theoretical fits, since no other data were available in this energy region at that time. Block and Malik (1967) discussed the resonance structure observed at higher energies in the data of Maher, et al., and the problem of

the nuclear surface in connection with heavy ion scattering was discussed by Gadioli-Erba and Sona (1969).

The Differentially Pumped Gas Target

The differentially pumped gas target system is shown in Figure 5. The target chamber was 29.3 cm I.D. with 6.4 mm thick steel walls. The first canal was between the chamber and the Roots pump and was 6.4 mm I.D. by 2.5 cm long. The second was 3.6 mm I.D. by 10.2 cm long and the third was 9.5 mm I.D. by 12.0 cm long. At each end of the second canal was an 0.5 mm thick tantalum collimator 2.5 mm in diameter which was responsible for determining the size of the beam in the chamber. Using the light produced by the beam in the gas, it was checked visually that the beam did not hit the sides of the first canal. A set of adjustable slits, set at a total width of 4.1 mm and separated from the second canal by 104 cm, gave a maximum permissible angular deviation of $\pm 0.18^{o}$ in the beam relative to the central axis of the system. Initial alignment of the canals was performed with a telescope zeroed on these slits. Attached to the first pumpout was a Roots pump with a pumping speed of about 70 liter/sec at 0.2 torr. The second pump was a 1200 liter/sec diffusion pump with a cold water baffle and the third one was a 750 liter/sec diffusion pump with Freon-22 baffle. The largest absolute pressure drop was across the first canal because of the high capacity of the Roots pump. The pressure in the gas target was measured by a 0 - 20 torr Wallace and Tiernan precision

Figure 5

Schematic of the Differentially Pumped Gas Target.

The parts of the differentially pumped system are drawn to the scale shown. The beam entered the target through three canals with typical pressures of 10^{-5} torr in the region of the slits, 10^{-4} torr between canals 2 and 3, 0.1 torr between canals 1 and 2, and 3 torr at the gas inlet. Several detectors were normally in the target chamber. The monitor (45°) counter was mounted on the inner aluminum cylinder in the chamber bottom. A teflon sleeve and two O-rings permitted it to rotate without breaking the chamber vacuum. Another counter could be mounted on the brass rod which rotated inside this aluminum cylinder. The counter telescopes were rigidly connected to the lucite top, which could also be rotated without breaking the vacuum because of another teflon sleeve and pair of O-rings.

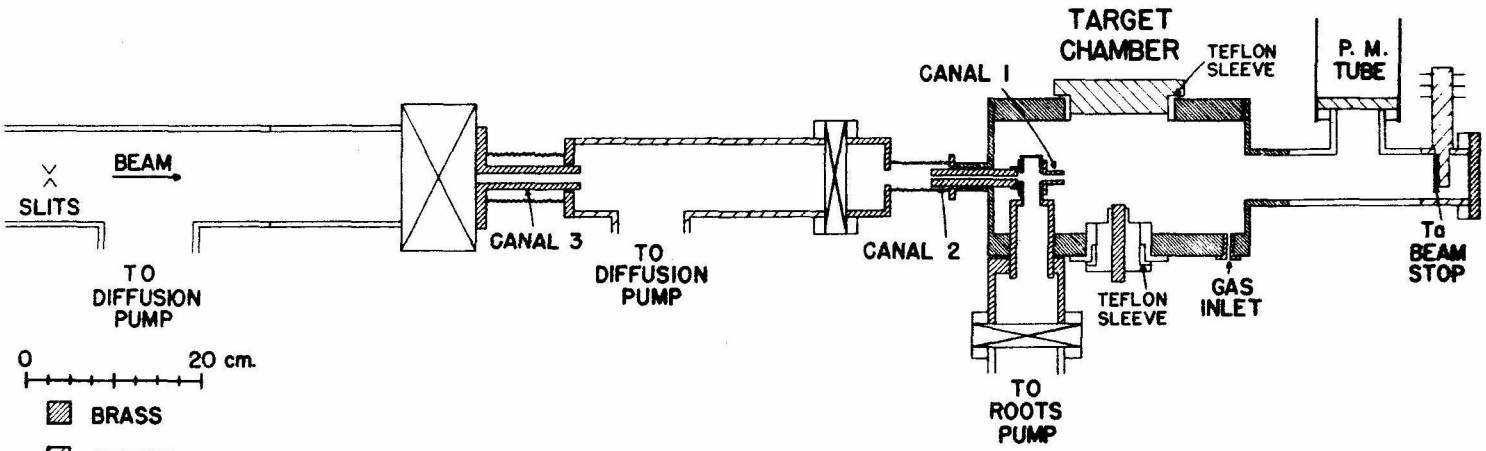

DIFFERENTIALLY PUMPED GAS TARGET

aneroid gauge, checked against a McLeod manometer.

The energy loss of the beam before arriving at the target chamber center was estimated by taking the full chamber pressure from the target region to the middle of the first canal and zero pressure beyond. With this approximation, the beam traversed 7 cm in the gas before reaching the center of the chamber. For pure O_2 gas at a chamber pressure of 3 torr, using Northcliffe's (1963) energy loss curves, a 22 MeV ^{16}O beam would lose about 320 keV before reaching the target. The straggling would be about 40 keV (FWHM). For a target length of 3 mm seen by the detector the target thickness would be about 14 keV (lab). The target length for the counter telescopes described in the Charged Particles Section was roughly an order of magnitude larger than this.

In the measurement of reaction cross sections, ultra high purity (> 99.99 % by volume) O_2 gas was flowed through the chamber at about 20 liter atm/hr for a chamber pressure of 3 torr. Small leaks, outgassing, and pump oil backstreaming were estimated at $< 4 \times 10^{-3}$ liter atm/hr total. The ratio of the number of hydrogen atoms to the number of oxygen atoms in the chamber was estimated to be $< 5 \times 10^{-3}$ from the observed hydrogen recoils from $^{16}O + {}^{1}H$ elastic scattering seen in forward angle proton spectra.

Light was emitted as the beam passed through the gas. The current from a photomultiplier viewing this light was used as an indication of the beam intensity, especially for purposes of focusing

and steering the beam into the target chamber. The photomultiplier current was proportional to the beam current within a factor of two over the entire energy range used in these experiments. Direct current integration with gas in the chamber was not attempted.

In a gas target there is an angle at which the number of counts from Rutherford scattering is independent of angle for a given detector collimator configuration. This useful fact was employed in part for monitoring the beam's angle in the chamber during the elastic scattering measurements. It was also used for the experimental determination of the ratio of geometrical factors for two different counters (see Charged Particle Section, page 70).

In a gas target the number of counts N in a counter is proportional to

$$N \propto \left(\begin{matrix}\text{solid angle} \\ d\Omega\end{matrix}\right) \cdot \left(\begin{matrix}\text{gas length} \\ L\end{matrix}\right) \cdot \left(\begin{matrix}\text{current} \\ i\end{matrix}\right) \cdot \left(\begin{matrix}\text{cross section} \\ d\sigma/d\Omega\end{matrix}\right).$$

Two defining collimators are needed per counter to restrict the length of the beam path seen. For a counter at $\theta_{lab} = 90^{o}$

$$L \cdot d\Omega = \langle \Omega L \rangle_{90^{o}} = A \cdot w/d \cdot D$$

with A = area of the back collimator, w = width of the front slit, d = distance between collimators, and D = distance from the beam line to the far collimator. At other laboratory angles

$$L \cdot d\Omega \simeq \langle \Omega L \rangle_{90^{o}} / \sin \theta_{lab},$$

because the path length seen by the counter increases. In the special case of pure Rutherford scattering of light particles by heavy targets

$$\frac{d\sigma}{d\Omega} \approx 1/\sin^4\left(\frac{\theta_{lab}}{2}\right)$$

so the angular dependence of N is

$$N \approx \frac{1}{\sin\theta_{lab} \cdot \sin^4\left(\frac{\theta_{lab}}{2}\right)}$$

and

$$\frac{dN}{d\theta_{lab}} = 0 \quad \text{for} \quad \tan^2\left(\frac{\theta_{lab}}{2}\right) = 5, \quad \theta_{lab} = 132^o.$$

Therefore, the number of counts N is nearly independent of angle for $\theta_{lab} \approx 132^o$ and pure Rutherford scattering of light beam particles on heavy targets (see Dwarakanath (1968)). Making corrections for the mass of the bombarding particle M_1, and of the target M_2, the corresponding angle is a solution of the equation

$$0 = 5 - \sin^2\theta_{lab} \cdot \left[9 + 20\left(\frac{M_1}{M_2}\right)^2\right] + \sin^4\theta_{lab} \cdot \left[24\left(\frac{M_1}{M_2}\right)^2 + 16\left(\frac{M_1}{M_2}\right)^4\right] - \sin^6\theta_{lab} \cdot \left[16\left(\frac{M_1}{M_2}\right)^4\right] .$$

In the particular case of ^{16}O on ^{40}Ar the correct angle is 135.6^o instead of 132^o, causing a difference in the number of counts of

$< 0.7\%$. Figure 6 plots the value of θ_{lab} as a function of M_1/M_2.

Experimental

The $^{16}O + ^{16}O$ elastic scattering was measured using various mixtures of ultra high purity Oxygen and Argon gases in the differentially pumped target. The ratio of pressures was typically $O_2 : Ar = 3 : 1$ to $1 : 1$. A special gas mixing bottle was used to make sure that the gases were well mixed (to within $\pm 0.25\%$). Mixtures containing a larger percentage of O_2 were employed especially at higher energies where the ratio of elastic to Mott scattering was less than 0.9.

Heat deposited along the beam path may cause changes in the gas density and perhaps in composition. Since only a ratio of counts was used for elastic scattering cross sections, density changes were unimportant. The continuous gas flow in the chamber also reduced composition changes along the beam path. Typical beams in the chamber varied from 3 - 7 μa of O^{4+}, corresponding to a loss of 0.13 to 0.30 watts/cm. It is estimated that these differences in heat loss could lead to $<< 0.1\%$ changes in the gas composition.

The energy loss of the beam before reaching the target region was determined experimentally using elastic scattering. The scattered particles' energy was measured for chamber pressures of 3.0 and 0.5 torr. Correcting for the 10.8 cm of gas between the target and counter, and using the measured energy shift, the energy loss

Figure 6

Special Scattering Angle vs. M_1/M_2.

The laboratory angle at which the number of counts from pure Rutherford scattering in a gas target is independent of angle is plotted against the ratio of the incident to the target masses M_1/M_2 (see the text page 26 and Figure 7). No such angle exists for $M_1/M_2 \geq 1.0$.

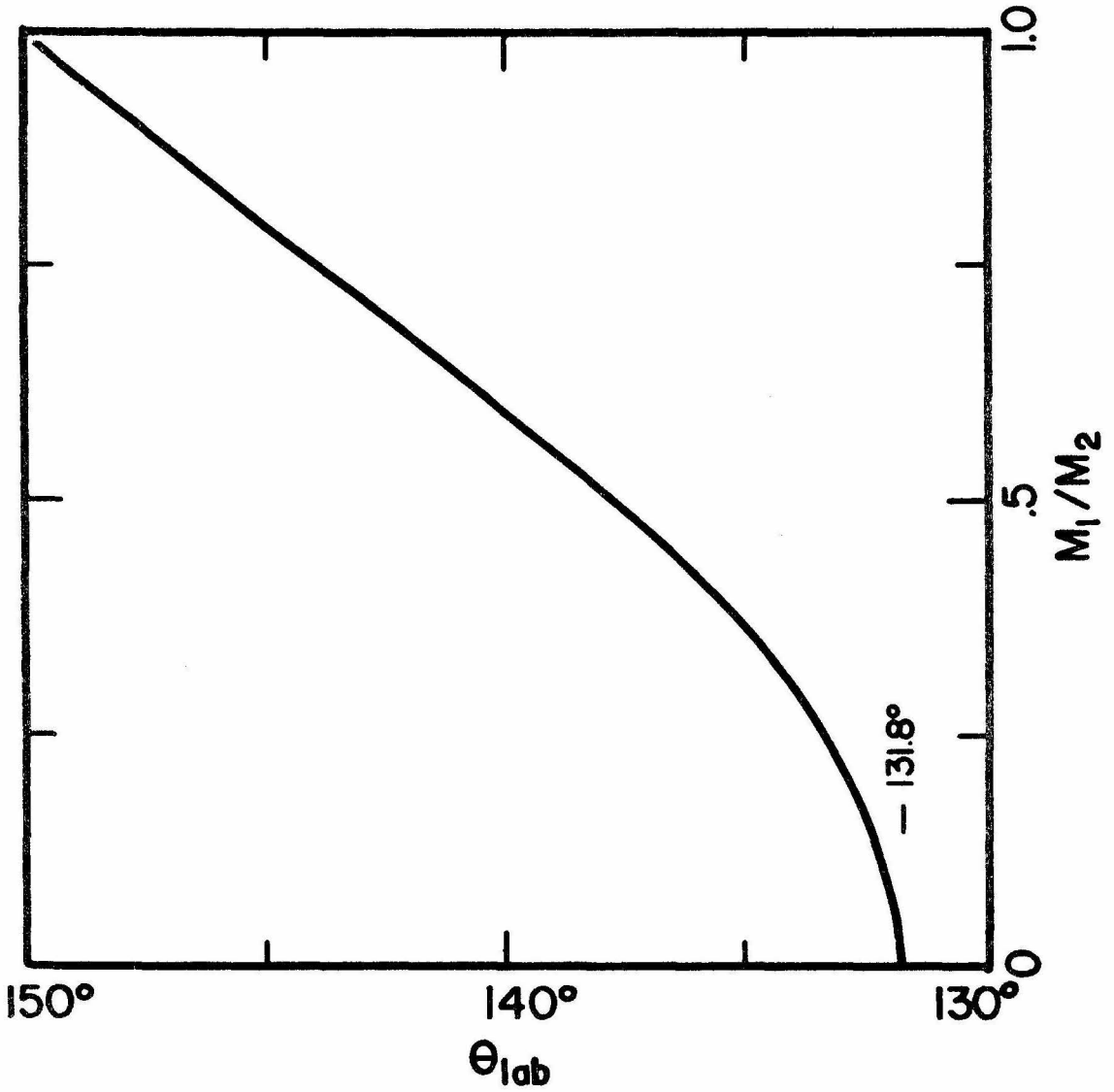
1.0
.5
0
M_1/M_2
— 131.8°
150°
140°
130°
θ_{lab}

of a 23 MeV ^{16}O beam to the center of the target was found to be 330 ± 60 keV (lab). Using Northcliffe's curves (1963), the energy loss and straggling are 310 keV and 40 keV (FWHM, lab) respectively.

The elastically scattered particles were observed simultaneously with three solid state counters (see Figure 7). Two were placed on one side of the beam to check on its position in the chamber: One counter was at 132^{o}, where the number of counts is nearly independent of angle, and the other was at a forward angle ($\theta_{lab} \approx 24^{o}$), where the count rate is a strong function of angle. The ratio of the ^{16}O beam particles scattered from the Argon gas into the 24^{o} counter, $N(Ar, 24^{o})$, to the number entering the 132^{o} counter, $N(Ar, 132^{o})$, changes by about 20%/degree and is a good indicator of beam angle changes. Experimental values of this ratio agreed within the statistical fluctuations expected from the numbers $N(Ar, 24^{o})$ and $N(Ar, 132^{o})$. The standard deviation in this ratio was ± 1.6%. This indicated beam angle changes of less than ± 0.08%, whereas the geometrically allowed change was ± 0.18^{o}. Furthermore, $N(Ar, 24^{o})/N(Ar, 132^{o})$ provided a check on whether or not the scattering of ^{16}O from Ar was purely Rutherford at higher bombarding energies. Deviations were found above E_{lab} = 27 MeV; however, the ratio $N(Ar, 24^{o})/N(Ar, 45^{o})$ did not change up to the highest energies measured. Thus $N(Ar, 45^{o})$ was taken to follow the $1/E^{2}$ law over the full range of energies used.

The third silicon detector was at $\theta_{lab} = 45^{o}$ on the other side of the beam from the 24^{o} and 132^{o} counters. (This same counter and

Figure 7

Arrangement of the Counters for the

Elastic Scattering Measurements.

The actual elastic scattering data were taken with the 45^{o} counter, but the other two detectors were used simultaneously to check for variations in the incident beam angle (see the text page 30). Also shown is the relative number of scattered protons calculated for p + Ar Rutherford scattering as a function of laboratory angle in a gas target (see the text pages 26 and 70).

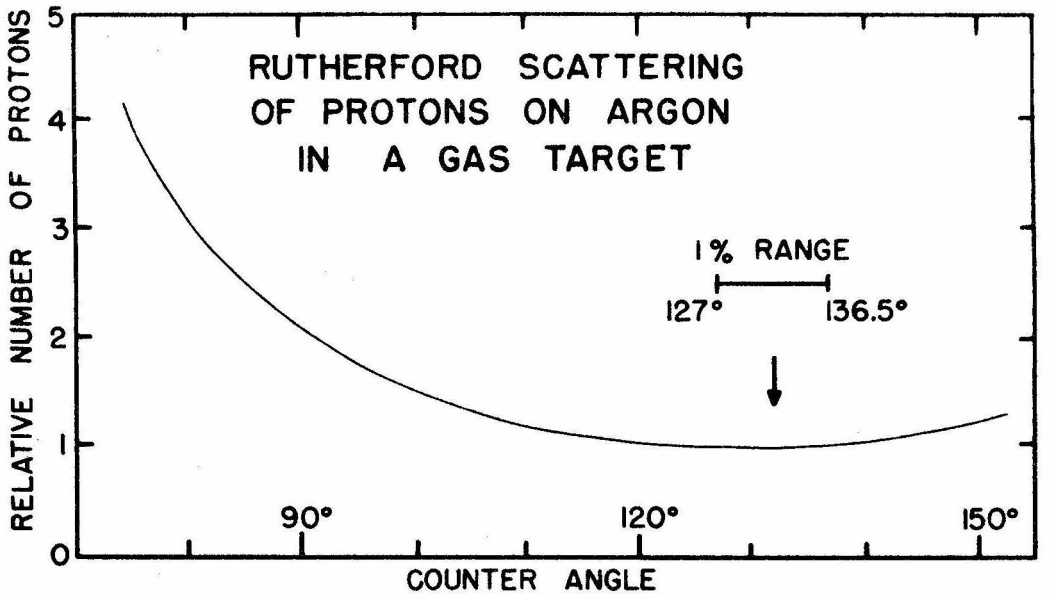
RUTHERFORD SCATTERING
OF PROTONS ON ARGON
IN A GAS TARGET
1% RANGE
127°
136.5°
RELATIVE NUMBER OF PROTONS
0
1
2
3
4
5
90°
120°
150°
COUNTER ANGLE

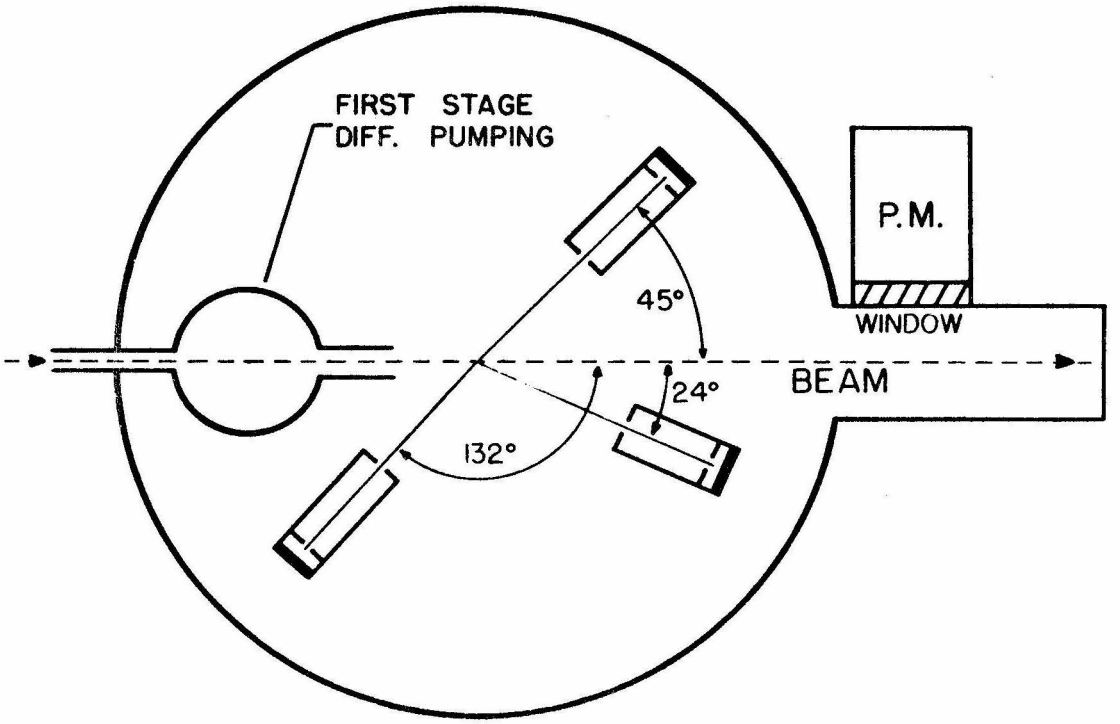
FIRST STAGE
DIFF. PUMPING
P.M.
WINDOW
45°
24°
BEAM
132°

collimator arrangement was used to monitor the target thickness and beam intensity in the other charged particle measurements.) Its collimation was $\pm 0.67^{\circ}$. The correct angle of this counter relative to the beam was determined by taking data in 1° steps over a set of angles near $\theta_{lab} = 45^{\circ}$. In the Mott scattering of $^{16}O + ^{16}O$, the number of ^{16}O scattered from ^{16}O nuclei into the 45° counter, $N(O,45^{\circ})$ exhibits a relative maximum when the counter is at 45° (see Figure 8). (The actual angle is about 44.9° because of the variation in the center-of-mass solid angle conversion factor with angle.) However $N(Ar,45^{\circ})$ varies monotonically with angle, so the ratio $N(O,45^{\circ})/N(Ar,45^{\circ})$, which gives the final data, has a maximum at an angle slightly greater than 45.0°. This difference was found to be 0.5°, in good agreement with calculations. In order to decrease the influence of small changes in the beam angle on the results, the counter was set between the two maxima at 45.2° relative to the beam. $N(O,45.2^{\circ})$ differs from $N(O,45.0^{\circ})$ by less than 1.3%.

All elastic scattering and recoil peaks in the spectra were well separated. These spectra from each of the counters were stored in multichannel analyzers, and the counts in the peaks were summed later and used in the data analysis.

Results

The theoretical angular distribution for pure Mott scattering is given by

Figure 8

Mott Scattering Angular Distribution Calculated for $^{16}O + ^{16}O$.

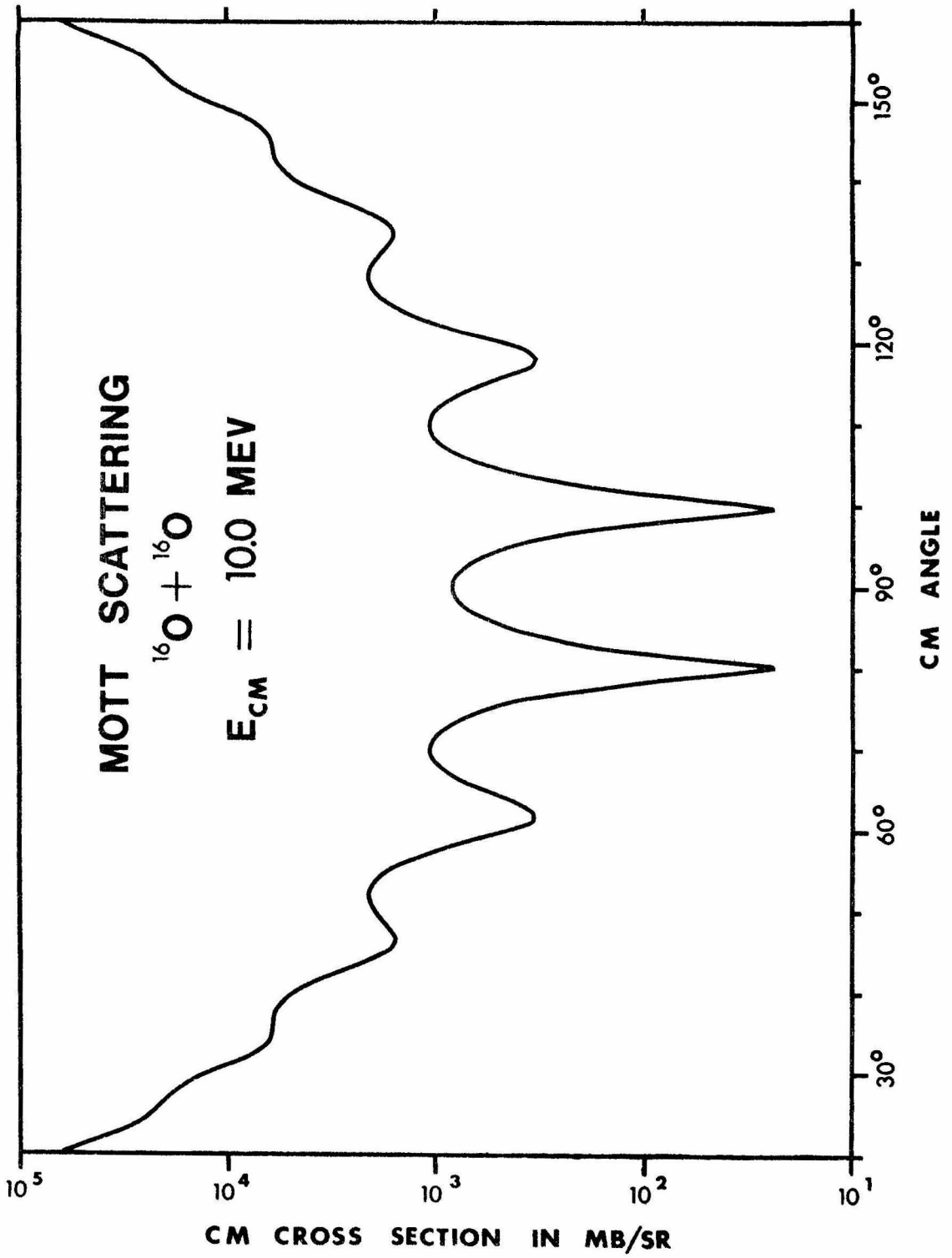
MOTT SCATTERING
$^{16}O + ^{16}O$
$E_{CM} = 10.0$ MEV
CM CROSS SECTION IN MB/SR
10^5
10^4
10^3
10^2
10^1
30°
60°
90°
120°
150°
CM ANGLE

$$\left(\frac{d\sigma}{d\Omega}\right)_{cm} = \left(\frac{Z^2e^2}{4E_{cm}}\right)^2 \cdot \left\{ \frac{1}{\sin^4\frac{\theta}{2}} + \frac{1}{\cos^4\frac{\theta}{2}} + (-1)^{2I}\frac{2}{2I+1}\frac{\cos\left(\eta\,\ell n\tan^2\frac{\theta}{2}\right)}{\sin^2\frac{\theta}{2}\cos^2\frac{\theta}{2}} \right\}$$

where

$$\eta = Z^2e^2/\hbar v_{rel}$$

θ = center of mass angle, and I = nuclear spin = 0 in this case. The interference term causes relative maxima and minima in the angular distribution (see Figure 8), and these change in angle with energy. However, at $\theta_{cm} = 90^o$ there is always a relative maximum and constructive interference, and the Mott prediction is just four times the pure Rutherford value there. That fact makes this particular angle ideal for monitoring beam intensity and target thickness in the case of the $^{16}O + {}^{16}O$ reactions.

The ratio of the $^{16}O + {}^{16}O$ elastic scattering to Mott scattering at $\theta_{cm} = 90^o$ is shown in Figure 9. Almost all points are the average of 2 to 6 measurements, or about 5 - 80 minutes counting time. Data in the region $E_{cm} = 9.5 - 11.5$ MeV are the results of 4 to 6 such measurements. These data were taken in several passes over the energy region covered to average out possible changes in the incident beam angle. A statistical analysis of all the results demonstrated that the beam angle was always within $\pm 0.08^o$ of the

Figure 9

$^{16}O + ^{16}O$ Elastic Scattering.

The ratio of the differential cross section for $^{16}O + ^{16}O$ elastic scattering at $\theta_{cm} = 90^{o}$ to the Mott scattering cross section is plotted. All errors are total errors (see Table 1). Energy losses in the gas have been subtracted and produce an overall uncertainty in the energy scale of $\pm$ 50 keV (C.M.). Data plotted as solid circles are exhibited on an expanded scale as well.

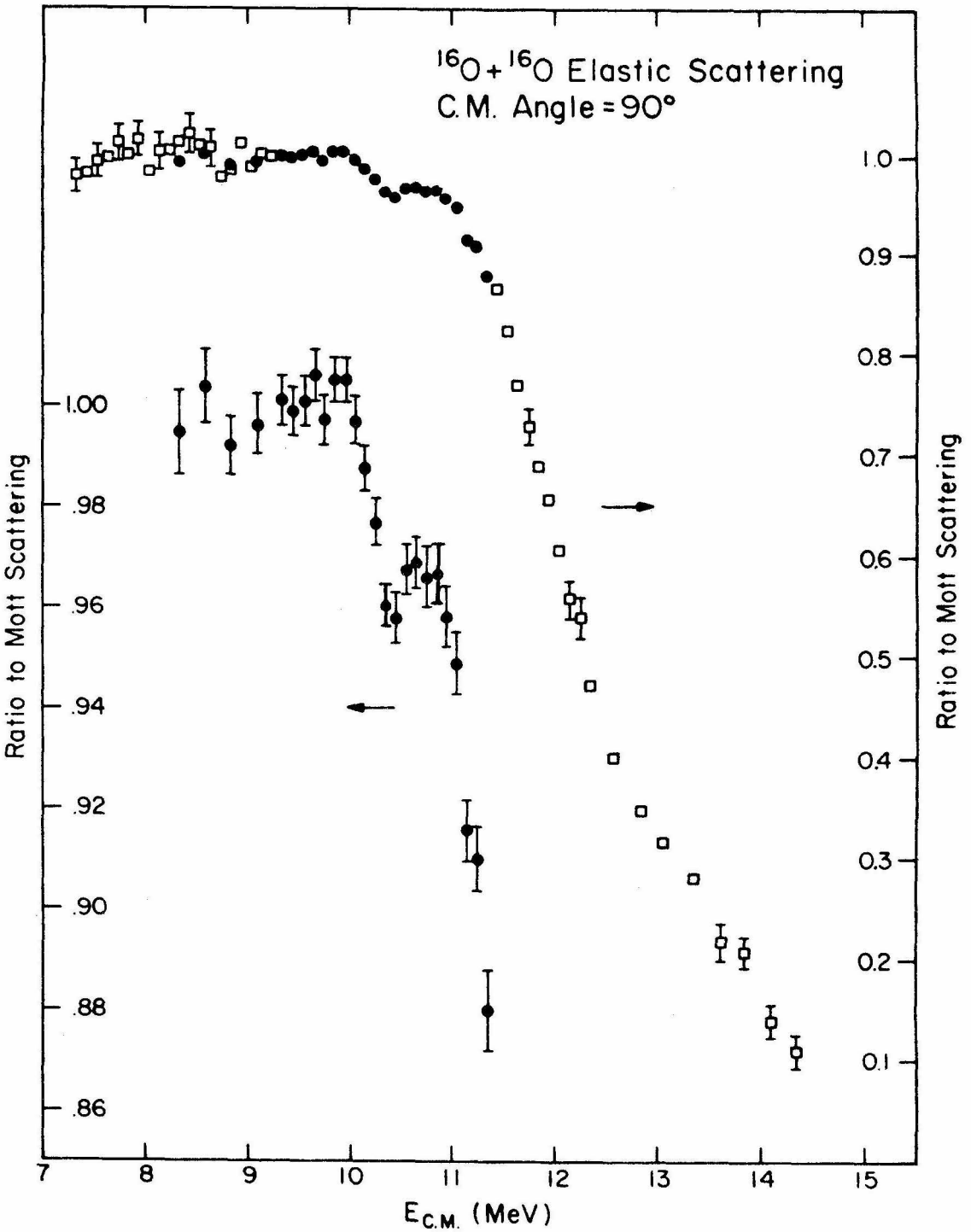
$^{16}O + ^{16}O$ Elastic Scattering
C.M. Angle = 90°
Ratio to Mott Scattering
1.00
.98
.96
.94
.92
.90
.88
.86
1.0
0.9
0.8
0.7
0.6
0.5
0.4
0.3
0.2
0.1
Ratio to Mott Scattering
7
8
9
10
11
12
13
14
15
$E_{C.M.}$ (MeV)

correct value. Changes in the intensity distribution of the beam across the entrance collimator, changes in the gas pressure, or rapid fluctuations in beam current affecting the dead time of the electronics, did not influence the results. This was because the ratio $N(O,45^{o})/N(Ar,45^{o})$ was obtained from one counter alone. Therefore, the error bars on the data of Figure 9 and Table 1 correspond only to statistical errors calculated from the total number of counts at each energy and the uncertainty in the normalization constant. The energy loss was taken to be the measured value of 330 ± 60 keV (lab) at E_{lab} = 23 MeV and was extrapolated to other energies using Northcliffe's curves (1963). An overall uncertainty in the C.M. energy scale for all points of ± 50 keV is estimated from the energy loss correction. The elastic scattering results permitted another check on the energy loss to the ^{16}O beam before reaching the target. The ratio $N(O_2,45^{o})/N(Ar,45^{o})$ was measured with 3.1 torr and with 0.7 torr chamber pressures at E_{cm} = 11.7 MeV, on the steep portion of the curve in Figure 9. The change in the ratio indicated a total energy loss before the target of 250 ± 100 keV, in agreement with the other, independent technique.

The average value of $N(O,45^{o})/N(Ar,45^{o})$ for $E_{cm} \leq 10.0$ MeV was used to normalize the data of Table 1 to 1.00 below the Coulomb barrier. The normalization factor agreed to within 2% with the value calculated for pure Coulomb and Mott scattering from the mixing ratio of the gases. The small difference is well within the uncertainty in the gas mixing percentages.

The numerical values of the data presented in the paper of Bromley, et al. (1961) are no longer available. Therefore, points were read off Figure 13 of that paper and then compared to values in Table 1. When this was done, the data of Bromley, et al. seem to be shifted up in energy by 150 - 250 keV (C.M.) from the gas target data for points above the Coulomb barrier. Part of this shift may be the result of reading the values from Figure 13.

However, it is also believed that the values of Bromley et al. should be shifted to lower energies by 50 - 100 keV (C.M.), or more, based on more recent energy loss information. The targets were quoted to be "~ 100 μ gm/cm^2 thick" SiO foils with an estimated energy loss of "~ 250 keV" (C.M.). The curves of Northcliffe (1963) predict an energy loss of 350 keV (C.M.) at E_{lab} = 24 MeV for such targets. With the larger energy loss estimate, the older data should be shifted down by 50 keV (C.M.) (half the error in the target thickness, since an average energy loss over the target is used). If the foils were actually 130 μ gm/cm^2, the predicted energy loss is 450 keV and the corresponding shift is 100 keV. Note that the data in Table 1 are shifted down in energy from the data of Bromley, et al. even without the correction for energy loss of the beam before reaching the target region.

Moving the energy scale down by 100 keV for the data of Bromley, et al. gives agreement within one standard deviation with the gas target results at energies above E_{cm} = 13 MeV; the older data are about 5 to 10% higher for E_{cm} = 11.5 - 13 MeV. This is

adequate agreement within their estimated errors, and the precision their values can be read from their Figure 13.

More recently, Maher, et al. (1969) measured the $^{16}O + ^{16}O$ elastic scattering at $\theta_{cm} = 90^{o}$ from $E_{cm} = 10$ to 35 MeV using a SiO foil target. Both particles were detected in coincidence. A fairly thick target was used by Maher in order to get sufficient yield at higher energies. These values are systematically shifted up in energy by about 250 keV C.M. from the gas target data. They are also shifted up in energy from Bromley's (1961) data. The reason for these discrepancies is not certain, but may be the result of poor knowledge of the solid target thickness and the energy loss. The gas target energy loss is believed to be well known.

The $^{16}O + ^{16}O$ elastic scattering curve should be compared to the one for $^{12}C + ^{12}C$ taken with the same apparatus (see Appendix I). The elastic scattering minima in $^{12}C + ^{12}C$ correspond to maxima in the reaction cross section and in α, p, n and γ yields. The lack of such structure in $^{16}O + ^{16}O$ elastic scattering (except for the single anomaly near $E_{cm} = 10.5$ MeV) suggests there may be a corresponding lack of fluctuations in the reaction cross section. See the Gamma Rays Section for a further indication that this is true.

GAMMA RAYS

Introduction

Gammas emitted from $^{16}O + ^{16}O$ reactions gave additional information on which exit channels are important and on the variation of the cross section with bombarding energy. Two different techniques were employed.

In one case, several spectra were taken with Ge(Li) detectors for ^{16}O beams bombarding various targets containing Oxygen. Only specific energy γ's were looked for, namely those from the first few excited states of nuclei formed in $^{16}O + ^{16}O$ reactions. Many levels can be populated in these nuclei; hundreds are energetically allowed in ^{31}P and ^{28}Si, for example. However, highly excited states will often decay by a cascade of γ's, proceeding through one of the low lying levels to the ground state, so transitions from the first few states are expected to be strong. Although branching ratios to the various exit channels could not be obtained from these observations, semiquantitative information based on the intensities of the observed lines indicated that the most important exit channels are $p + ^{31}P$ and/or $2p + ^{30}Si$, $\alpha + ^{28}Si$, $d + ^{30}P$ and/or $pn + ^{30}P$, $2\alpha + ^{24}Mg$, and $\alpha p + ^{27}Al$. There was also evidence for $n + ^{31}S$. Very rough estimates of the relative strength of these channels were made, but Doppler broadening of lines and similarities in characteristic γ energies prevented more definite conclusions. The most

important finding was the significant number of three body breakup reactions present and the sizeable increase in the two body reaction percentage at lower bombarding energies.

The total γ yield as a function of C.M. energy in $^{16}O + ^{16}O$ was measured in 50 keV (C.M.) steps with a NaI (Tl) scintillator placed just above the beam line in the differentially pumped target. The number of γ's emitted increases with the total reaction cross section, but a strict proportion is not expected because of cascades from highly excited states, significant changes in angular distributions, and possibly a preferential population of certain levels. The γ yield will be sensitive to fluctuations in the reaction cross section over restricted energy intervals, such as those observed in the $^{12}C + ^{12}C$ system (see Patterson, Winkler and Zaidins (1969) and Almqvist (1960, 1963)) since there are so many excited states that can be fed. The γ yield data suggest that the $^{16}O + ^{16}O$ total reaction cross section varies smoothly with energy and fluctuations, if present, are less than the errors for the charged particle measurements.

Ge (Li) Detector Spectra

Several high resolution γ spectra were obtained for $^{16}O + ^{16}O$ reactions at E_{cm} = 12 MeV with 40 and 55 cc coaxial Ge (Li) detectors for a number of different targets.

One spectrum in Figure 10 was taken using the differentially

Figure 10

$^{16}O + O_2$ Gas and ^{16}O + NiO Gamma Spectra.

These spectra were taken with a Ge(Li) counter at a bombarding energy of 24 MeV (E_{cm} = 12 MeV). The targets were O_2 gas at 1.5 torr pressure in the differentially pumped system and a 90 $\mu gm/cm^2$ nickel foil oxidized by heating in an Oxygen atmosphere. The same gain was used in both spectra, and the energies of some identified lines are shown. Doppler line broadening is especially noticeable in the $^{16}O + O_2$ gas spectrum.

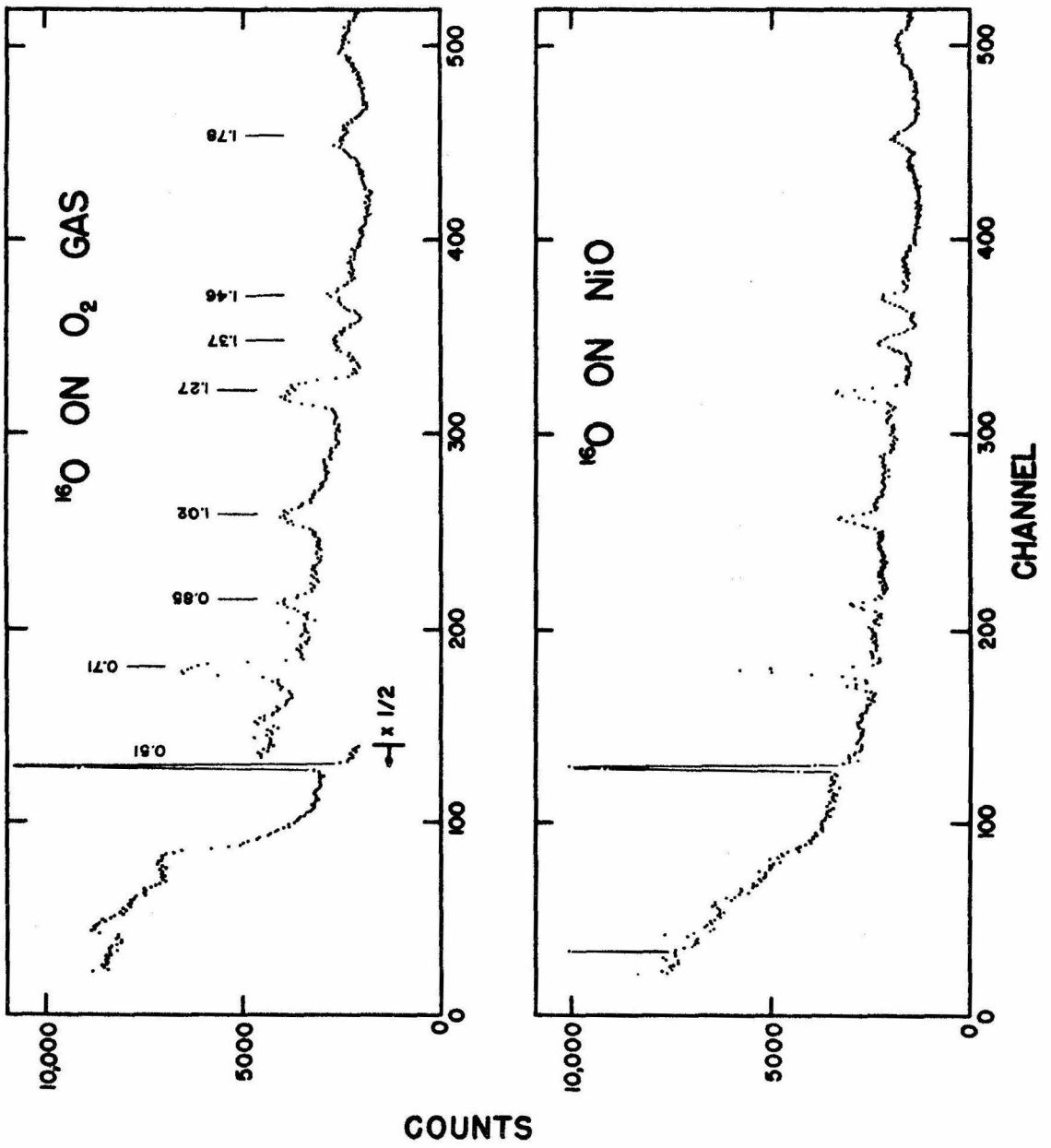
^{16}O ON O_2 GAS
0.61
0.71
0.86
1.02
1.27
1.37
1.46
1.78
x 1/2
^{16}O ON NiO
0
100
200
300
400
500
5000
10,000
COUNTS
CHANNEL

pumped gas target with a gas pressure of 1.5 torr. The front surface of the detector was placed about 5 cm from the beam path and 48 cm beyond the target chamber center. Shielding from γ's produced upstream and downstream was 11 cm of lead arranged so the target length was about 15 cm or 340 keV (lab). The tantalum beam stop was 97 cm from the detector. Energy calibrations for this and other spectra were made using ^{22}Na, ^{54}Mn, ^{60}Co, ^{88}Y and ^{137}Cs sources to an accuracy of ± 5 keV.

Most γ lines in Figure 10 are much wider than expected from the actual detector resolution. The main contribution to the line width is Doppler broadening because the heavy reaction products have velocities relative to the detector when they decay. For the case of $^{16}O + {}^{16}O \rightarrow \alpha + {}^{28}Si^*$ (1.78) the Doppler shift is expected to be up to 65 keV or 3.6%, and for $^{16}O + {}^{16}O \rightarrow p + {}^{31}P^*$ (1.27) it is up to 35 keV or 2.7%. The observed widths (FWHM) of both lines are about 4.0% from Figure 10. The 70 keV (FWHM) straggling in the beam energy acquired from passage through 55 cm of O_2 gas to the target region caused no significant further broadening of the γ lines.

In a thick solid target the γ energy resolution is better than for the gas target because the density is much higher, so the heavy nuclei are slowed down much more quickly and the Doppler broadening corresponds to the slower velocity at the time of the γ decay. Since the lifetime of the $^{31}P^*$ (1.27) level is 0.73 ± .07 ps and of $^{28}Si^*$ (1.78) is 0.63 ± .03 ps (Endt and van der Leun (1967)), only

about 10^{-3} μ gm/cm^2 of O_2 gas is traversed before a γ decay from these states in the gas target. The corresponding thickness for a solid target is on the order of 1 μ gm/cm^2. The difference in γ line widths is apparent between the spectra of the ^{16}O beam bombarding O_2 gas and a NiO foil (made by oxidizing a 1000 Å commercial Ni foil in a pure O_2 atmosphere with a collimated light source) in Figure 10 and a thick piece of quartz shown in Figure 11.

The advantage of better resolution resulting from thick solid targets is partly offset by the uncertainty in the origin of some γ lines. Since solid targets cannot be made of pure Oxygen, they are susceptible to the production of undesired γ's from reactions with other nuclei in the target. For example, with hydrocarbon contaminants on the target surface, the reactions $^{16}O + {}^{12}C \rightarrow p + {}^{27}Al$ and $^{16}O + {}^{16}O \rightarrow \alpha p + {}^{27}Al$ would lead to the same characteristic γ's and could not be distinguished.

The Ge (Li) detector was always at right angles to the beam with at least a 1 cm thick cylindrical lead shield around the detector housing as some protection against background. The distance between the counter's front surface and the beam spot varied from spectrum to spectrum and ranged from 2 to 10 cm with about 1 mm of aluminum in between. The beam intensity was generally kept below 200 na of charge 5+ ^{16}O because of both the high neutron fluxes and the high counting rates.

Figure 11

^{16}O + Quartz Gamma Ray Spectrum.

This spectrum was taken with a 55 cc coaxial Ge(Li) detector for 24 MeV ^{16}O nuclei bombarding a thick piece of quartz (SiO_2). Energies of the more prominent peaks were determined from the energy calibration, which is good to about ± 5 keV. The 0.511 MeV Compton edge obscures most gamma lines below about 0.4 MeV. However, two strong low energy lines are present and are believed to be X-rays from lead.

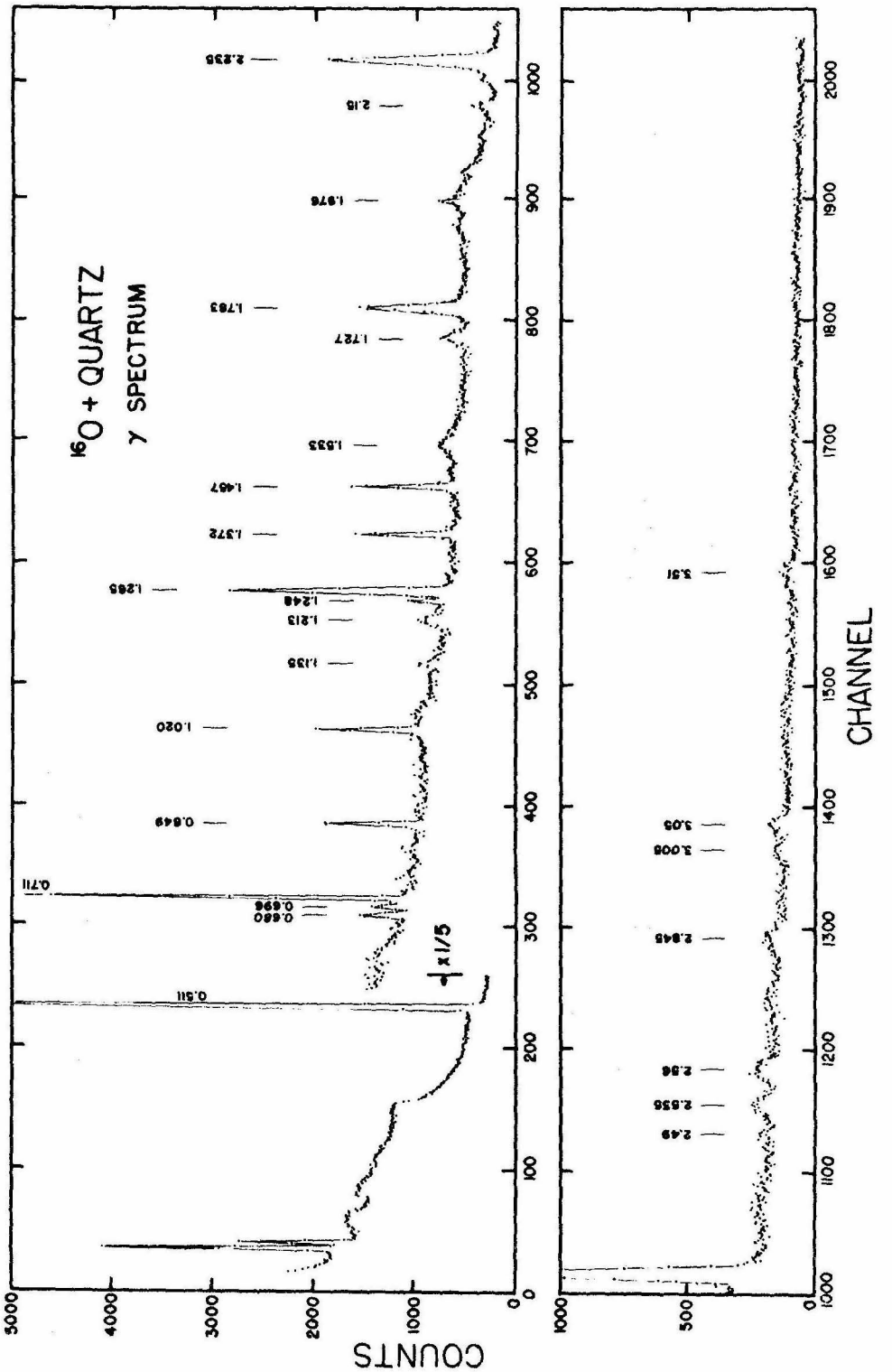
^{16}O + QUARTZ
γ SPECTRUM
COUNTS
CHANNEL
0.511
0.711
0.660
0.698
0.849
1.020
1.135
1.248
1.273
1.368
1.597
1.634
1.783
1.827
1.976
2.18
2.235
x 1/5
2.49
2.535
2.86
2.845
3.008
3.03
3.91

Table 2 lists the γ energy, the relative detection efficiency, and the counts normalized to the number in the 2.23 MeV peak for 9 strong lines observed in all spectra. The estimated errors on the ratios range up to ± 20% because of problems in background subtraction. Note that the ratio of counts varies significantly. Some differences arise from the variety of circumstances under which the spectra were taken. Others probably came from contaminants on the targets or from ^{16}O + Si reactions. Since all peaks in Table 2 are present in the gas target spectra, they are all believed to originate from $^{16}O + ^{16}O$ reaction products. The relative photopeak efficiency of the detector was estimated from Paradellis and Hontzias (1969), Huang, Osman and Ophel (1969) and from direct measurement to roughly follow a power law

$$\text{Efficiency} \sim E^{-\alpha} \quad \text{with} \quad \alpha \simeq 1.2$$

This quantity is also tabulated in Table 2.

Estimates of branching ratios to the various $^{16}O + ^{16}O$ exit channels were made from the intensity of lines in Figure 11. Some conclusions were also implied by the absence of certain transitions. Table 3 gives a list of the γ lines between 0.5 and 4.4 MeV from Figure 11, the most probable transition or transitions involved, and other possibilities that are considered less likely (for $^{16}O + ^{16}O$ reactions only). Some lines or contributions to some peaks may be from undesired γ's. Below 500 keV the annihilation peak and its Compton edge dominated, and above 4.4 MeV little structure was

observed. Transition energies were taken from Endt and van der Leun (1967) and the γ energies were obtained from the energy calibration with a number of sources. The accuracy is about ± 5 keV except at the higher energies where no calibration lines were used. Several lines remain unidentified.

Identifications in Table 3 were required to be self consistent in a number of ways. Single and double escape peaks were always broader than the photopeaks of about the same energy. Strong lines between 1.5 and 2.5 MeV and all lines above 2.5 Mev were required to have both. γ decay schemes and branching ratios, where known, were taken into account. Thus if a transition between the third and second excited states was present, the γ's depopulating the second level had to be seen as well. Finally, if a transition from the second excited state in a nucleus was identified, the one from the first excited state was also required to be present, etc. An exception to the latter was that ^{31}P $(3 \rightarrow 0) = 3.135$ MeV was not observed, but decays from higher levels were.

A number of conclusions can be drawn from Tables 2 and 3 corresponding to $E_{cm} = 12$ MeV. These follow for each $^{16}O + ^{16}O$ exit channel with $Q > 11$ MeV (see the energy level diagram Figure 1). Level energies and γ branching ratios were taken from Endt and van der Leun (1967) and Ajzenberg-Selove and Lauritsen (1959). All yields are stated as ratios to the ^{28}Si yield and are generally based on results presented in Table 2. Limits on yields come from Figure 11.

$^{26}Mg + \alpha + 2p$, $^{28}Si + t + p$, $^{28}Si + {}^{3}He + n$. All are expected to be small because of Q values. No conclusions are possible from γ-ray yields since no excited states can be populated at $E_{cm} = 12$ MeV.

$^{27}Si + \alpha + n$. Neither the transitions from the first nor from the second excited states of ^{27}Si were observed. A limit on the yield was derived to be < 0.05 (relative to $^{28}Si \equiv 1.0$).

$^{29}P + t$. There is only marginal evidence for the ^{29}P $(1 \rightarrow 0)$ transition, and none for the decay from the second excited state. The yield was estimated at $\lesssim 0.03$ times the ^{28}Si yield at $E_{cm} = 12$ MeV. The large negative Q value and Coulomb barrier probably suppress this channel.

$^{29}Si + {}^{3}He$, $^{29}Si + p + d$, $^{29}Si + 2p + n$. No conclusions possible. The $(1 \rightarrow 0)$ transition is masked by the 1.27 MeV γ's from ^{31}P, ^{30}Si, etc. The $(2 \rightarrow 0)$ transition is masked by the 3.05 MeV second escape peak, by ^{31}P $(4 \rightarrow 1)$ and by ^{31}S $(4 \rightarrow 1)$.

$^{16}O + {}^{12}C + \alpha$. The only energetically allowed state is the 4.43 MeV level of ^{12}C, but it is not observed (see Figure 11).

$^{20}Ne + {}^{12}C$ and $^{20}Ne + 3\alpha$. Very little can be concluded. No counts above background were detected at $E_{\gamma} = 1.63$ MeV for ^{20}Ne $(1 \rightarrow 0)$ or at 4.43 MeV for ^{12}C $(1 \rightarrow 0)$. The Q values indicate that these channels may proceed through the

ground states most of the time, emitting no γ's. See the $^{12}C + ^{20}Ne$ Production Section (page 152) for a measurement of the cross section to the ground state.

$^{30}P + d$, $^{30}P + p + n$. γ decays from the first four and perhaps five levels of ^{30}P were identified. The 0.67 MeV line was weak because $^{30}P^*$ (1) is a T = 1 state. The number of γ's from ^{30}P is about the same as from ^{28}Si.

$^{27}Al + p + \alpha$. Decays from the first three or four states in ^{27}Al are present. The fourth is in question because of the absence of ^{27}Al $(4 \rightarrow 0)$, whereas the 1.727 line is broad and contains the single escape peak from 2.23 MeV γ's. The possible presence of $^{16}O + ^{12}C$ reactions must be considered, so the number of ^{27}Al formed by $^{16}O + ^{16}O$ reactions is $\lesssim 0.5$ times the number of ^{28}Si formed.

$^{24}Mg + 2\alpha$. The $(1 \rightarrow 0)$ transition is strong, but others are weak or absent. However the second to fourth levels in ^{24}Mg decay with $E_\gamma > 2.7$ MeV. Again there is the possibility of $^{16}O + ^{12}C$ reactions, so the yield of ^{24}Mg is $\lesssim 0.4$ (relative to the ^{28}Si yield $\equiv 1.0$).

$^{31}S + n$. This channel is very weak compared to others with similar Q values. ^{31}S $(1 \rightarrow 0)$ was observed, but the $(2 \rightarrow 0)$ transition, if present, is obscured by the mirror transition ^{31}P $(2 \rightarrow 0)$ and others. Based on the 1.24 MeV γ's only, the ^{31}S yield is ~ 0.06 times the ^{28}Si yield.

$^{31}P + p$ and $^{30}Si + 2p$. The idea of taking γ spectra was originally conceived as a means of separating these channels. This failed because of a remarkable number of coincidences. The γ's involved are:

1.27 MeV. There are at least 5 different transitions within 5 keV of this energy. One is the 1.78 MeV first escape peak, expected to comprise only a small fraction of the counts in this line. The amount of $^{29}Si\ (1 \rightarrow 0)$ is uncertain, but the amount of $^{30}P\ (4 \rightarrow 2)$ can be estimated using the known γ decay scheme of $^{30}P^*\ (4)$ and the counts in the 1.98 MeV peak. Note that $^{31}P\ (1 \rightarrow 0)$ and $^{30}Si\ (2 \rightarrow 0)$ transition energies are identical within the errors and the detector resolution.

2.235 MeV. Four important transitions occur within ± 3 keV. The $^{32}S\ (1 \rightarrow 0)$ and $^{31}S\ (2 \rightarrow 0)$ γ's are expected to comprise only a small portion of the total from the lack of transitions from higher states in both and from the size of the $^{31}S\ (1 \rightarrow 0)$ peak. That leaves $^{31}P\ (2 \rightarrow 0)$ and $^{30}Si\ (1 \rightarrow 0)$, whose energies are within 2 keV.

3.505 MeV. $^{30}Si^*\ (2)$ decays 55% of the time through the 2.23 MeV level, and 45% of the time directly to the ground state. However, there is evidence for decays in ^{31}P from its first six excited states (excluding the third state), so there is a possibility of a contribution from $^{31}P\ (6 \rightarrow 0)$. The importance of the latter transition cannot be checked from the

γ decay scheme of $^{31}P^*$ (6) because the energy of ^{31}P (6 → 1) is 2.239 MeV! Nevertheless, for only the counts in the 1.27 MeV line, the number of ^{30}Si is < 0.2 and of ^{31}P is > 0.7 (normalized to the number of $^{28}Si \equiv 1.0$) from the strength of the 3.51 MeV peak. The combined strength of all these lines for ^{30}Si and ^{31}P is 3.5.

$^{28}Si + \alpha$. Decays from the first two excited states were observed. This is the only reaction producing a 1.78 MeV γ, and there are many levels of ^{28}Si which cascade through $^{28}Si^*$ (1.78). Thus the 1.78 MeV line was ideal to compare to other yields, and its strength was taken to be $\equiv 1.0$.

^{32}S. Unfortunately no conclusions can be reached. ^{32}S (1 → 0) has an energy of 2.23 MeV, which is the same as several other strong transitions. The observation of the decay from $^{32}S^*$ (2) is questionable because of the "line" shape (see Figure 11). Thus there is no evidence for or against a negligible yield in this channel from the γ spectra.

A summary is given in Table 4. These conclusions agree qualitatively with the preliminary analysis performed in the Introduction Section based on Q values and Coulomb barrier heights.

Table 4 contains similar data for ^{16}O beams bombarding quartz at E_{lab} = 20 and 18 Mev as well. A background spectrum was subtracted from the 18 MeV run, but was unnecessary for the spectra taken at the other energies. The decrease in the fraction

of three body exit channels can be noted from the fall in the relative branching ratios of ^{27}Al, ^{24}Mg and ^{30}P.

Such information is quite important in relating the measured production cross sections for protons and alphas to reaction cross sections. A proton from $^{30}Si + 2p$ should be counted only half as much as one from $^{31}P + p$ in the proton spectra, since two light particles are emitted per reaction in the former case. The uncertainty in the three body fraction will be reflected in the reaction cross section, because of the difference of a factor of 2 in the counting, and in any extrapolation of the cross section to energies below $E_{cm} = 7$ MeV. See the Conclusions Section (page 171) for a further discussion of the above problem.

γ Yield vs. Energy

Fluctuations in the total cross section should appear in the γ yield as a function of bombarding energy, especially if many excited states are populated, as in $^{16}O + ^{16}O$ reactions. Such fluctuations exist in the $^{12}C + ^{12}C$ system and these data were taken to look for a similar behavior in $^{16}O + ^{16}O$.

The differentially pumped gas target, usually at a pressure of 1.5 torr of ultra high purity O_2, was used for the measurements. The beam passed through about 16 cm of gas before reaching the center of the target region, losing about 400 keV (lab). The straggling was estimated at 40 keV (FWHM, lab).

A 2 × 2" NaI (T1) scintillator was located with its front face 2.2 cm above the beam line with 0.5 cm of aluminum between them. A 1.9 cm lead shield around the crystal restricted the target length to about 9 cm or 100 keV (C.M.). The attenuation to 0.51 MeV γ's was a factor of 110 and to 2.23 MeV γ's was 2.8. Precautions against undesired γ's were taken: inside the scattering chamber there was lead placed around the entrance and exit apertures, and the beam stop was moved 140 cm away from the target region.

Three discriminators were used to count all γ pulses above cutoff points of 0.6, 1.6, and 2.2 MeV. The monitor counter from elastic scattering measurements was set at $\theta_{lab} = 45^{o}$ and was used for normalization. The yield was determined from

$$\text{YIELD} = \text{CONST} \cdot \frac{(\#\ \gamma\text{'s} - \text{background rate} \cdot \text{time})}{(\#\ \text{monitor counts})\ (E_{cm}{}^{2})} \cdot \begin{pmatrix}\text{ratio of elastic}\\ \text{scattering to}\\ \text{Mott}\end{pmatrix}$$

The constant was chosen to normalize the yield to 100.0 at $E_{cm} =$ 10.0 MeV so data with different cutoff energies could be compared. Errors were estimated from statistical uncertainties on the number of counts and from a 3% error for pressure changes, shifts in the cutoff energy, and errors in the elastic scattering cross section.

The results are given in Table 5. The background was found to be proportional to time (36 counts per minute for the 2.2 MeV cutoff and 410 for the 0.6 MeV cutoff). No additional background was observed from the canal of the gas target. Counting times ranged from 1 to 16 minutes. Energies were corrected for losses in the gas. The

normalized yields for all three cutoff energies agree within ± 20 % over the whole energy range measured, with the lower cutoff energy data presenting a steeper energy dependence. This systematic difference could result from cascaded γ's; a small fraction of such γ's are detected with the higher cutoff than with the lower ones. Thus, the variation with energy of the average number of cascade γ's per reaction influences the lower cutoff data more strongly. Furthermore, certain exit channels may be excluded by setting the cutoff too high, also influencing the energy dependence.

In the energy range covered, the γ yield changes by a factor of nearly 10,000 (see Table 5). To see small fluctuations, the barrier penetration effect can be factored out:

$$\text{YIELD} \sim \frac{\tilde{S}}{E_{cm}} \exp\left(-\frac{2\pi Z_1 Z_2 e^2}{\hbar v_{cm}} - g E_{cm}\right)$$

and the results are plotted in Figure 12 for the 1.6 MeV cutoff. No absolute normalization was used for $\tilde{S}$, and the value of g was chosen somewhat arbitrarily (it corresponds to an interaction radius of 7.25 fm). Other g values would tilt the data one way or the other in the plot, but would not affect the presence of bumps. Small fluctuations may actually be present in Figure 12, but they could not be seen in the charged particle data with the larger measurement errors.

This situation should be compared to similar results obtained for $^{12}C + ^{12}C$ reactions, also displayed in Figure 12. Charged

Figure 12

$\tilde{S}$ for the Yield of Gamma Rays from $^{16}O + ^{16}O$ and $^{12}C + ^{12}C$.

The differentially pumped system was used for the $^{16}O + ^{16}O$ measurements and a 10 μgm/cm^2 carbon foil was used for the $^{12}C + ^{12}C$ data. In both cases the detector was NaI and elastic scattering monitored the combined target thickness and beam current (see the text pages 58 and 181 and Tables 5 and 18). The values of $\tilde{S}$ for $^{16}O + ^{16}O$ are in arbitrary units (see Figure 41), whereas the $^{12}C + ^{12}C$ results are normalized at $E_{cm} = 4$ MeV to the charged particle data of Patterson, Winkler and Zaidins (1969), which is also plotted.

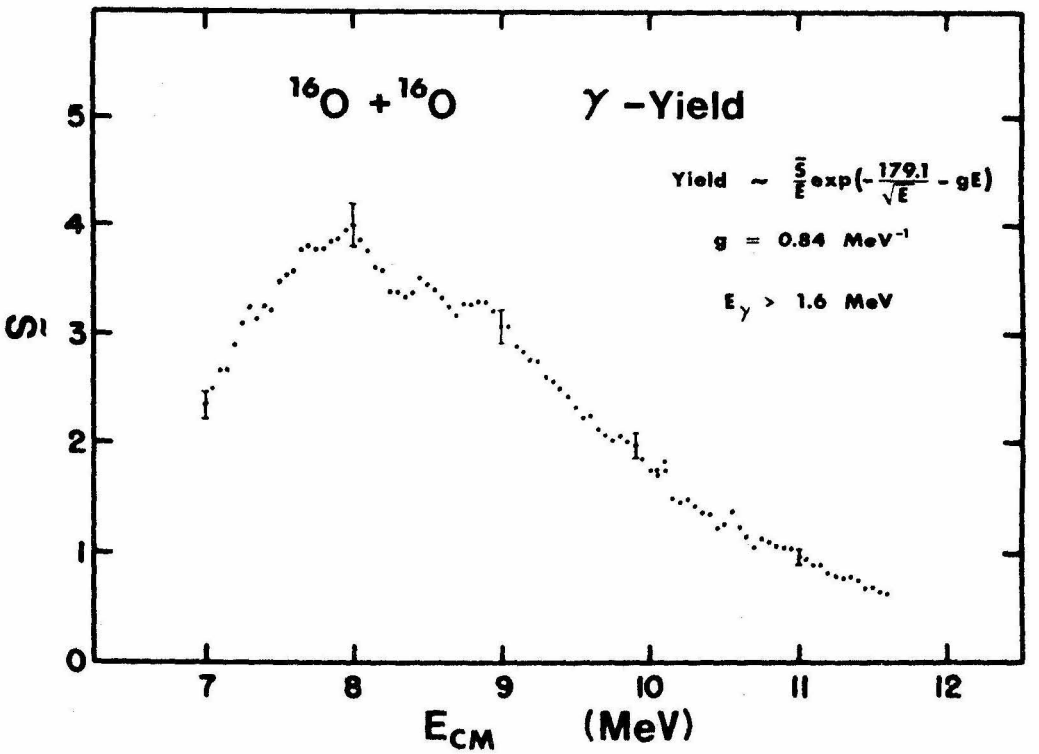
$^{16}O + ^{16}O$ γ -Yield
Yield ~ $\frac{\tilde{S}}{E}\exp(-\frac{179.1}{\sqrt{E}} - gE)$
g = 0.84 MeV^{-1}
E_γ > 1.6 MeV
Sl
E_{CM} (MeV)

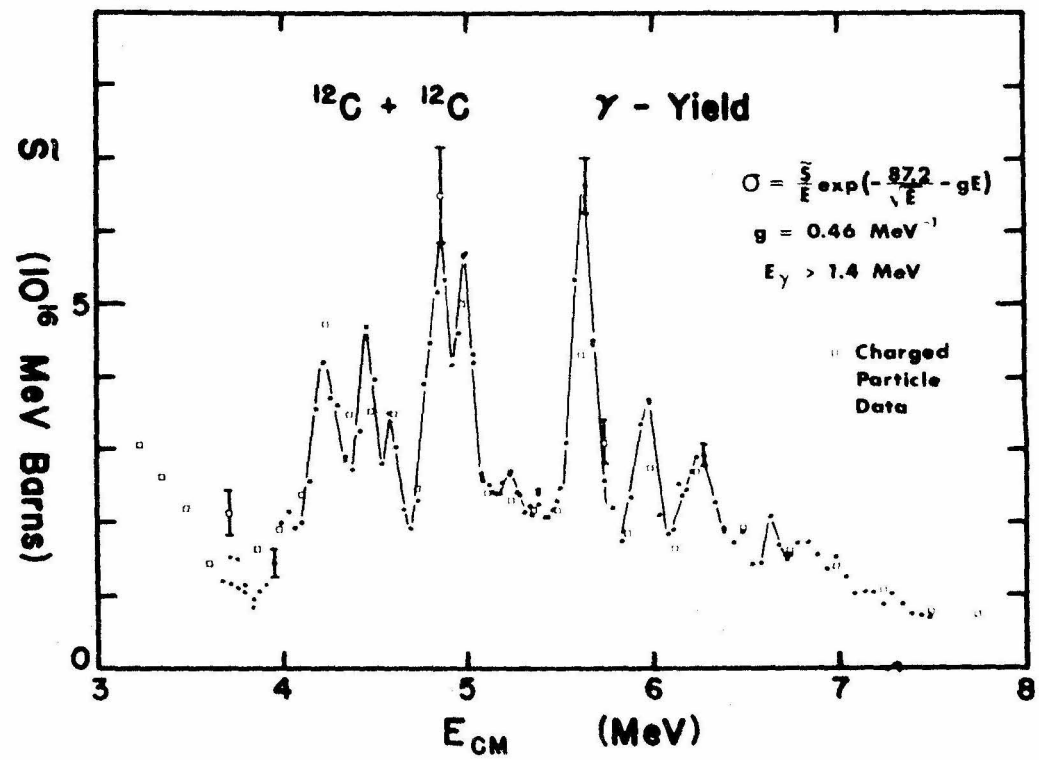
$^{12}C + ^{12}C$ γ - Yield
$\sigma = \frac{\tilde{S}}{E}\exp(-\frac{87.2}{\sqrt{E}} - gE)$
g = 0.46 MeV^{-1}
E_γ > 1.4 MeV
Charged Particle Data
Sl (10^{16} MeV Barns)
E_{CM} (MeV)

particle measurements from Patterson, Winkler and Zaidins (1969) and γ yield data normalized to the former at $E_{cm} = 4$ MeV as described in Appendix II are plotted. The agreement over the full energy range might have been worse if some other cutoff energy were employed. Such an effect was noticed in the $^{16}O + ^{16}O$ case. A more detailed structure was seen with the γ yield data because it was easy to take fine energy steps. The sharp contrast between the two sets of data in Figure 12 is the main evidence for concluding that the $^{16}O + ^{16}O$ cross section is relatively smooth. One important consequence is that it is not necessary to take charged particle data for $^{16}O + ^{16}O$ in small energy steps.

CHARGED PARTICLES

Introduction

Most of the $^{16}O + ^{16}O$ total reaction cross section comes from channels with at least one light charged particle emitted. The gamma spectra and the arguments in the Introduction, based on compound nucleus formation and Coulomb barriers, indicate that the most important of these exit channels are:

$^{16}O + ^{16}O \rightarrow$	$^{28}Si + \alpha$	Q = 9.592 MeV
	$^{31}p + p$	7.676
	$^{30}Si + 2p$	0.388
	$^{24}Mg + 2\alpha$	-0.390
	$^{27}Al + p + \alpha$	-1.991
	$^{30}P + d$	-2.412
	$^{29}Si + ^{3}He$	-2.510
	$^{30}P + p + n$	-4.636

Cross sections for the production of protons, deuterons and alphas were determined by measuring their yield at a number of angles.

Two counter telescopes were constructed to distinguish between these light charged particles. Particles of different masses could be distinguished by passing the particles through a transmission detector of thickness Δx to measure the energy loss, $\Delta E = dE/dx \cdot \Delta x$, and then measuring the total energy E remaining with

another counter.

A number of purely experimental problems prevented the detection of all light charged particles down to the lowest energies at a given laboratory angle. Protection of the counter telescope from the very high elastic scattering count rates required a foil to stop the ^{16}O nuclei. Furthermore, particles of low energy stopping in the ΔE detector of the telescope could not be identified properly and were not counted.

It was important for the low energy cutoff for each type of particle to be as low as possible, so few counts would be lost. This requirement dictated that the protection foil thickness be kept to a minimum and suggested the use of a proportional counter for measuring ΔE. A silicon surface barrier detector with the same energy loss for protons as the proportional counter constructed would have a thickness of 4μ, and was not commercially available. In addition, the high capacitance of such a detector would result in a resolution no better than that of the proportional counter. The foil necessary to retain the proportional counter gas introduced a small additional energy loss (equivalent to 4.2μ of silicon). For many bombarding energies and angles it served as part of the protection foil needed against elastically scattered particles. One of the two counter telescopes used a 58μ thick solid state detector in order to separate the deuterons from the protons, because the proportional counter resolution was not good enough for these particles.

Although the total energy resolution of the counter telescope was $\lesssim 400$ keV, only a few levels in ^{28}Si, ^{31}P and ^{30}P were actually resolved. One reason is that in the residual nuclei regions of excitation energy having a high density of states are energetically accessible. There are hundreds of such states in just the first two exit channels tabulated above. Furthermore, the low particle yields required large angular openings for the counter telescopes, resulting in kinematic broadening of the peak from a given excited state. Finally, the three body channels produce a continuum of particle energies for a given state in the residual nucleus.

Under these circumstances, contaminant reactions could be completely masked by $^{16}O + ^{16}O$ reactions and still contribute a sizeable portion of the particle counts. For example, protons or alphas from $^{16}O + ^{12}C$ or $^{16}O + ^{14}N$ might go unnoticed because individual levels were not resolved. So it was necessary to use a very pure target material and to take precautions to prevent contaminants. A solid target containing Oxygen was not acceptible for this reason.

The most satisfactory target was ultra high purity Oxygen gas in a differentially pumped system. The beam intensity was not limited by the entrance foil needed for a "closed" gas target, and the beam energy loss and straggling were well under control. Gas flowing through the target chamber swept out all impurities from outgassing in the system, preventing buildup of target contaminants. Details of the differentially pumped gas target are given in the

Elastic Scattering Section (page 21).

Angular distributions of protons and alphas were taken at 8 energies between E_{cm} = 6.8 to 11.85 MeV with the counter telescope (with a proportional counter to measure ΔE). Total production cross sections were derived from these measurements. However there was a problem relating these to $^{16}O + ^{16}O$ reaction cross sections because of three body breakups. In two body exit channels only one light particle is emitted per heavy ion reaction, whereas two are given off in each reaction for three body channels. A proton or alpha from the latter should thus be counted only half as much as in the two body case. The uncertainties in the percentages of each exit channel was a serious source of error in deriving $^{16}O + ^{16}O$ reaction cross sections from the data.

The deuteron yield was measured at E_{lab} = 20 and 24 MeV in a similar fashion. Searches were made for ^{3}He and ^{3}H at the same energies, but none were detected. Limits on the latter cross sections were derived.

Experimental

All charged particle measurements were made using the differentially pumped gas target with ultra high purity Oxygen gas (> 99.99% by volume) at a chamber pressure of 3.0 - 3.5 torr. The same 45^{o} counter used for the elastic scattering measurements monitored the combined beam current and target thickness as described in the Elastic Scattering Section (page 30). Before each series of runs,

the angle of the monitor counter was set to $\theta_{lab} = 45^{o}$ by maximizing the yield of elastically scattered oxygen. Its geometrical factor was

$$\langle \Omega L \rangle_{90^{o}} = (6.2 \pm 0.4) \times 10^{-5} \text{ cm sr}$$

and its angular opening was $\pm 0.7^{o}$.

The alpha and proton spectra were obtained with a counter telescope (Figure 12) composed of a proportional counter to measure ΔE and a 2 mm thick lithium drifted silicon detector (110 mm^2 in area) to measure E of the particles. The gas tight housing of the telescope was rigidly connected to a lucite flange rotating in an O-ring in the lid of the scattering chamber. The cylindrical proportional counter was 2.9 cm in diameter by 3.8 cm long and was machined in a block of aluminum (see Rossi and Staub (1949) and Curran (1958) for the design of proportional counters). The high voltage electrode was a 0.1 mm diameter length of piano wire on the axis of the proportional counter. It was supported by a cylindrical glass insulator on the end nearest the E counter, and by a Kovar glass feedthrough on the other end, bringing the electrical connection to the wire out of the counter housing. An Ortec 109 PC charge sensitive preamplifier with built in FET protection was connected to this point by a coaxial cable enclosed in stainless steel tubing. The tubing was open to the atmosphere on one side and epoxied onto the counter housing, over the Kovar feedthrough, on the other side. Thus all high voltage connections to the proportional counter were under atmospheric pressure. The total capacity of the counter wire and

Figure 13

Cross Sectional View of the Counter Telescope.

This counter telescope consisted of a proportional counter to measure ΔE and a 2 mm thick Si(Li) counter to measure E of the particle. The proportional counter consisted of a cylinder of Argon gas in the aluminum telescope housing. The high voltage wire was on the cylinder axis and was connected to a Kovar glass insulated feedthrough and then to a coaxial cable protected by stainless steel tubing (see the text page 66). The proportional counter gas continuously flowed through the counter at a pressure of about 120 torr. The whole counter telescope was rigidly mounted on the lucite top to the target chamber (see Figure 5).

COUNTER TELESCOPE

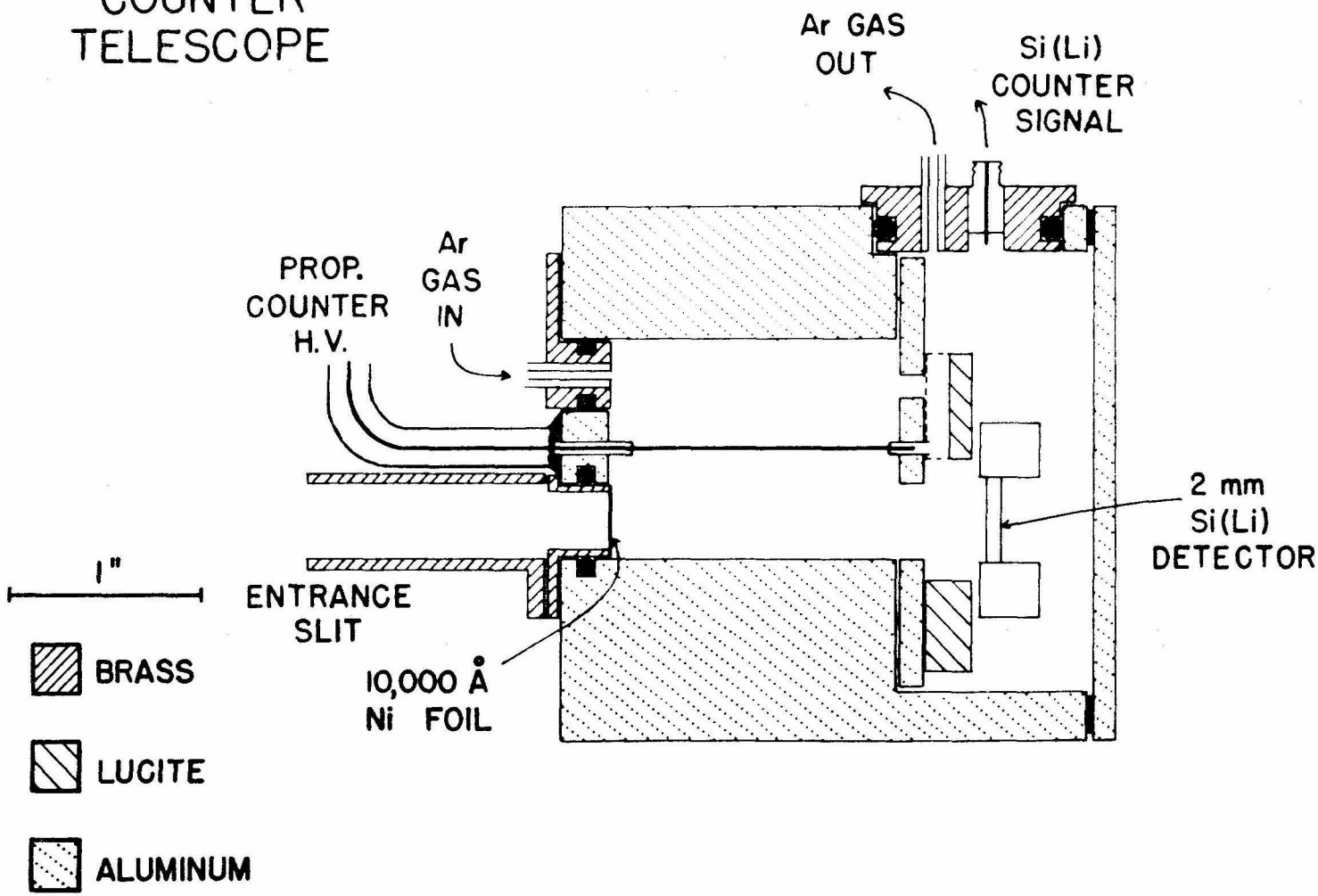

cable, up to the preamplifier input, was 13 pf. Electrical breakdown occurred at about 300 V in the Oxygen gas (at 3 torr chamber pressure) when the high voltage connection was made without the tubing, whereas it occurred at about 600 V in the counter gas (120 torr) with the cable at atmospheric pressure. The normal operating voltage was 550 V and the corresponding gas multiplication was roughly 100. A mixture of Argon and 3% Methane served as the proportional counter gas, and flowed continuously through the counter. A forepump and two needle valves maintained a constant pressure of 100 - 130 torr as measured on a manometer in parallel with the counter during the actual runs.

Particles entered the telescope through a 1.6 mm vertical slit in a 1.6 mm thick brass disk. They then passed through the counter gas retaining foil of 10,000 Å nickel. In order to protect the Si (Li) detector from heavy ions and the telescope from high elastic scattering count rates, especially at very forward angles, one of three different foils could be inserted in addition in front of the telescope without breaking the target vacuum. The foil thicknesses were 1.4 mg/cm^2 and 3.4 mg/cm^2 aluminum (0.0002" and 0.0005") and 0.9 mg/cm^2 nickel (10,000 Å). The thinnest foil needed to stop the elastically scattered Oxygen was used at each angle and energy. The detection limits with just the entrance foil alone, and with the 3.4 mg/cm^2 aluminum foil in addition, were respectively 0.6 and 1.3 MeV for protons and 2.5 and 5.0 MeV for alphas. For laboratory angles over 70^o the telescope entrance foil

was thick enough to stop all particles from $^{16}O + ^{16}O$ elastic scattering and no additional foils were used. The lowest possible detection limit was thus obtained for a region of angles where the reaction products have lower energies for kinematic reasons.

The alphas were always stopped in the telescope, however protons above 18 MeV were not because the E detector was too thin. These counts were recorded by the electronics as having an energy (E) lower than they actually possessed, and they constituted less than 3% of all protons. Such conditions arose only at forward laboratory angles with high bombarding energies.

The telescope angular resolution was $\pm 3.9^{o}$ and its geometrical factor was

$$\langle \Omega L \rangle_{90^o} = (1.28 \pm 0.05) \times 10^{-3} \text{ cm sr.}$$

An experimental check on the solid angle factors was performed by scattering 1.8 MeV protons from pure Argon gas in the differentially pumped system at a chamber pressure of 2.0 torr. At this energy the scattering is pure Rutherford (at least for $\theta_{lab} < 140^{o}$, see Dwarakanath (1968)). Both the monitor and the counter telescope were moved to $\theta_{lab} = 132^{o}$ where the number of counts detected is independent of angle (see Elastic Scattering Section, page 26). The ratio of the number of counts in the counter telescope and in the monitor counter gave

$$\frac{\langle \Omega L \rangle_{\text{MONITOR, } 90^\circ}}{\langle \Omega L \rangle_{\text{TELESCOPE, } 90^\circ}} = (5.2 \pm 0.2) \times 10^{-2}.$$

The correction to account for the fact that the number of counts is not exactly independent of angle is $< 1\%$. Multiple scattering corrections are estimated to be $< 10\%$. The same ratio from geometrical measurements is

$$= (4.8 \pm 0.3) \times 10^{-2}.$$

A mean value of $(5.0 \pm 0.2) \times 10^{-2}$ was used for the evaluation of the data.

A schematic of the electronics associated with the counter telescope is shown in Figure 14. After amplification, the ΔE and E pulses were stored in the two coordinate directions of a two dimensional Nuclear Data 64×64 channel analyzer. The ADC processing the ΔE pulses was coincidence gated from a low level discriminator set on the E pulses, thus eliminating much of the noise inherent in the proportional counter. A typical two dimensional spectrum is shown in Figure 15.

The only background observed in the spectra was a continuum of counts with $\Delta E \simeq 0$ and $E \geq 0$, up to about $E = 8$ MeV. These counts were identified as γ's detected by the Si (Li) counter. The cutoff energy E was independent of angle, but the number of counts varied with angle from $\theta_{lab} = 20$ to 150° (approximately as $1/\sin \theta_{lab}$). Neutrons were excluded as the main contribution

Figure 14

Counter Telescope Electronics.

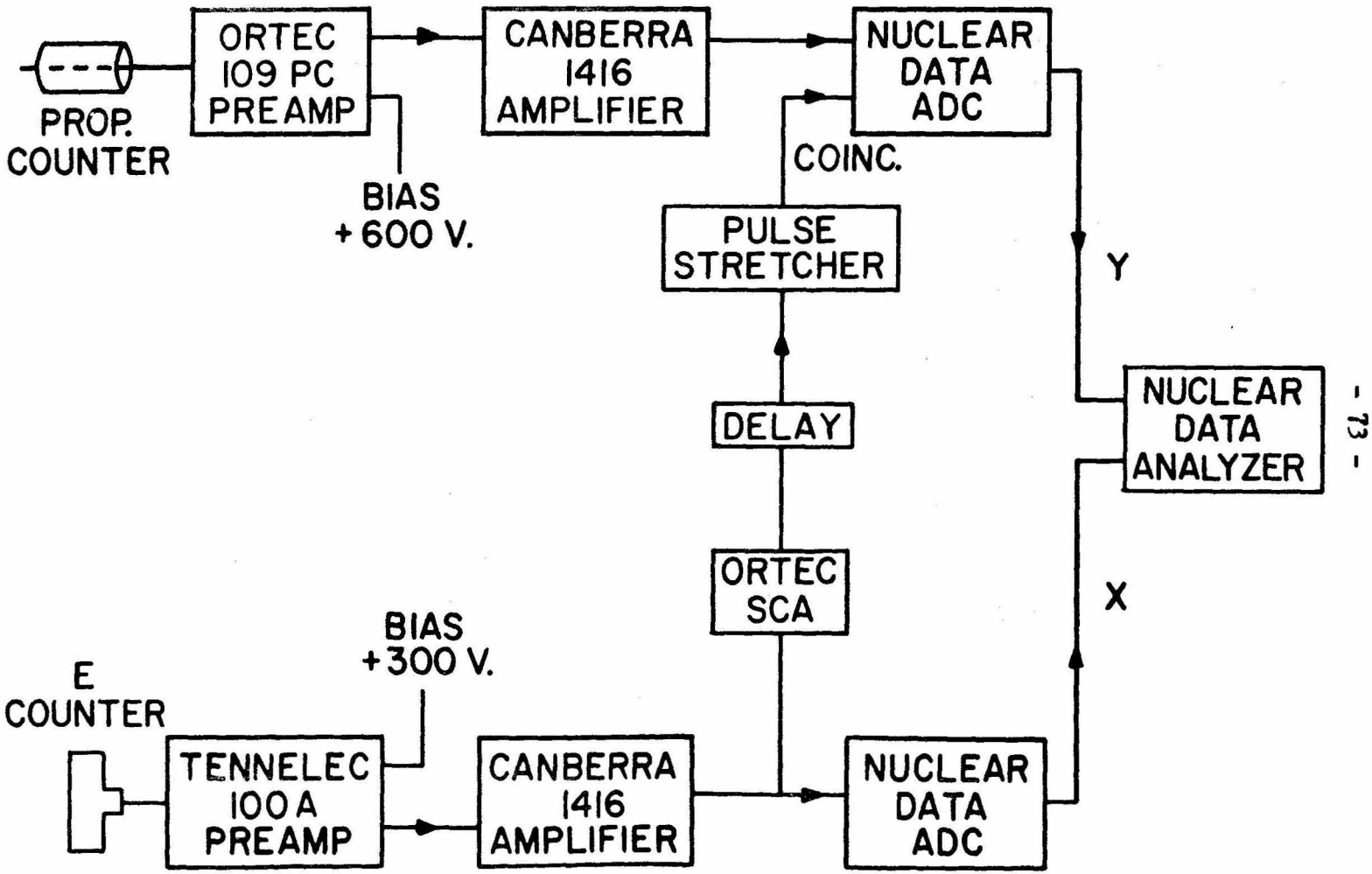
ORTEC
109 PC
PREAMP
CANBERRA
1416
AMPLIFIER
NUCLEAR
DATA
ADC
PROP.
COUNTER
BIAS
+600 V.
COINC.
PULSE
STRETCHER
Y
NUCLEAR
DATA
ANALYZER
DELAY
ORTEC
SCA
X
BIAS
+300 V.
E
COUNTER
TENNELEC
100A
PREAMP
CANBERRA
1416
AMPLIFIER
NUCLEAR
DATA
ADC

Figure 15

Two Dimensional Charged Particle Spectrum.

This spectrum was taken at E_{cm} = 11.85 MeV and θ_{lab} = 20° with the counter telescope of Figure 13. Note that the alpha (uppermost), proton and background ($\Delta E = 0$) lines are well separated. Summing counts in the ΔE direction gives the alpha and proton spectra of Figure 16. A cross section of the counts at E = channel 7 ($E \sim 3.3$ MeV) is given in Figure 18.

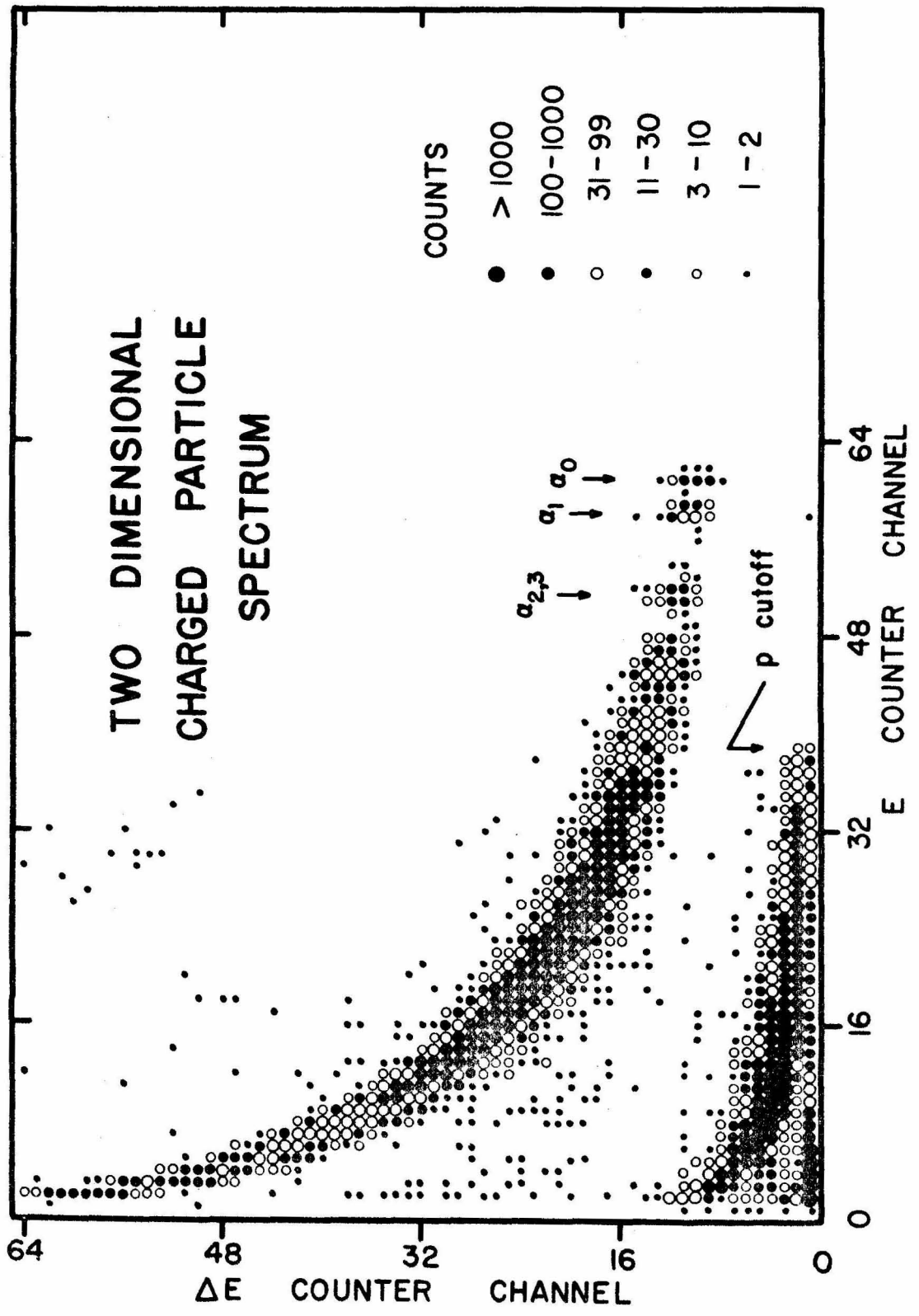
TWO DIMENSIONAL
CHARGED PARTICLE
SPECTRUM
COUNTS
> 1000
100-1000
31-99
11-30
3-10
1-2
$a_{2,3}$
a_1 a_0
p cutoff
64
48
32
16
0
ΔE COUNTER CHANNEL
E COUNTER CHANNEL

because the neutron production cross section was measured and was too small to account for the observed counts (see Neutrons Section, page 141). Electrons from ionization processes in the target and β decay electrons probably contributed somewhat to this background. The proton line was generally separated from these background counts by a channel or more, and the proton spectra showed no indications that extraneous counts were included. The efficiency and possible noise contributions in the two dimensional coincident ΔE - E pulse recording system were checked by using different gains and time delays for the two channels. No anomalies were found.

The energy scale in the E direction was calibrated with the protons and alphas corresponding to the lowest lying levels in ^{31}P and ^{28}Si respectively, since these levels could be seen as separated lines. Energy losses in the foils and gases (O_2 and Ar) were calculated from tabulations by Whaling (1958), Marion (1968) and Northcliffe (1963). The two dimensional spectra were summed in the ΔE direction to get particle spectra as shown in Figure 16. The magnitude of the particle energy in the Si (Li) counter, $E = E_{counter}$, was determined from the energy calibration, and could be related to the energy of the light particles in the target region, E_3, using the energy losses calculated.

Several experimental checks on the calibration and energy losses were made. For example, the 1.8 MeV protons used for the solid angle factor ratio measurement afforded one check. Another

Figure 16

Alpha and Proton Spectra.

These spectra are taken from the two dimensional spectrum of Figure 15. The peaks in the alpha spectrum are not the result of statistics (see Figure 17 and the text page 79). The E counter was not thick enough to stop the highest energy protons, so the "p cutoff" corresponds to the highest energy that can be deposited by protons in this counter. This situation occurred only at forward angles and the highest bombarding energies used.

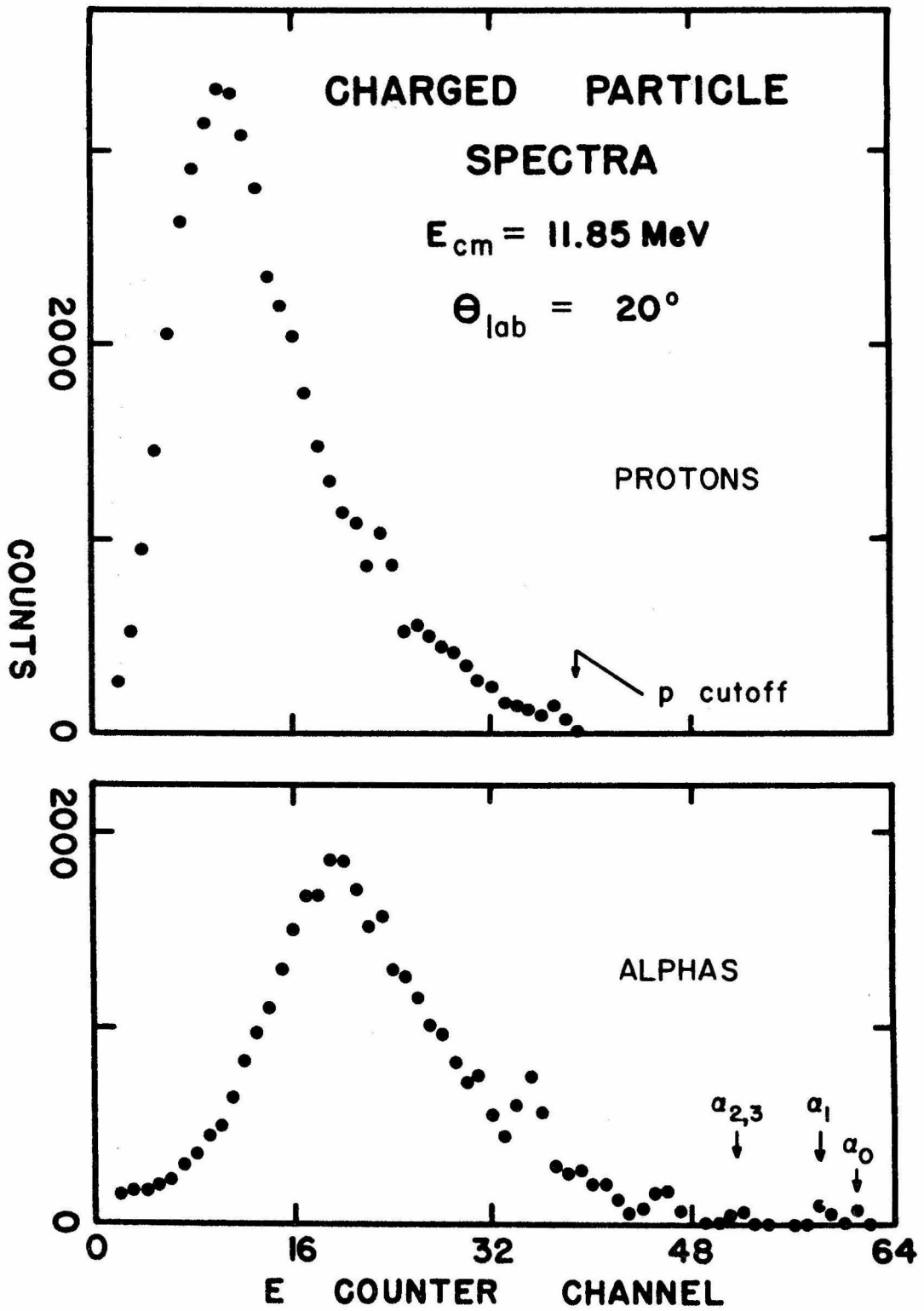
CHARGED PARTICLE
SPECTRA
E_{cm} = 11.85 MeV
θ_{lab} = 20°
PROTONS
p cutoff
ALPHAS
$\alpha_{2,3}$
α_1
α_0
COUNTS
2000
0
0
16
32
48
64
E COUNTER CHANNEL

was obtained from peaks seen in the alpha spectra. These were observed at many different angles and energies and were found to correspond to certain fixed excitation energies in ^{28}Si. A portion of the alpha spectrum at $E_{cm} = 11.95$ MeV and $\theta_{lab} = 20^{o}$ was obtained using the 61 cm magnetic spectrometer ($\Delta\theta = \pm 1^{o}$, $\Delta\phi = \pm 4.5^{o}$) and the 16 counter array in the focal plane. An Oxygen beam bombarded a SiO foil target. The alphas were bent by the spectrometer and passed through 5.1 mg/cm^2 (0.00075") of aluminum before entering the counters. A monitor counter at $\theta_{lab} = 45^{o}$ detecting the elastically scattered Oxygen was used to normalize the runs, and relative efficiency corrections of up to 20% were applied to each counter of the array. The resulting spectrum is given in Figure 17. The range of alpha energies covered was $E_{\alpha} = 10.7$ to 21.2 MeV ($E_{exc} = 8.2$ to 16.5 MeV). A large contribution to the width of the observed peaks came from kinematic broadening effects ($\Delta\theta \cdot dE/d\theta = \pm 120$ keV). The energy positions of the peaks were checked against the counter telescope spectra demonstrating that the energy calibration had a precision of $\pm$ 400 keV for E_3 or $\pm$ 300 keV for E_{exc} over the whole spectrum. On the other hand, the energy resolution of the counter telescope was only about 400 keV for these experiments because of the kinematic broadening of the lines, limited resolution in the 64 channels used for recording the spectra, and straggling. Agreement of the energy calibration as derived from the protons and as derived from the alphas provided still another check that energy losses were correctly computed.

Figure 17

Alpha Spectrum Taken with the Spectrometer.

These data were taken with a SiO foil target and the 16 counter array in the focal plane of the 61 cm spectrometer. The resolution was limited by kinematic broadening due to the large angular opening of the spectrometer entrance slits. Some peaks are shown with appropriate excitation energies. These were used to check the energy calibration of the counter telescope charged particle spectra.

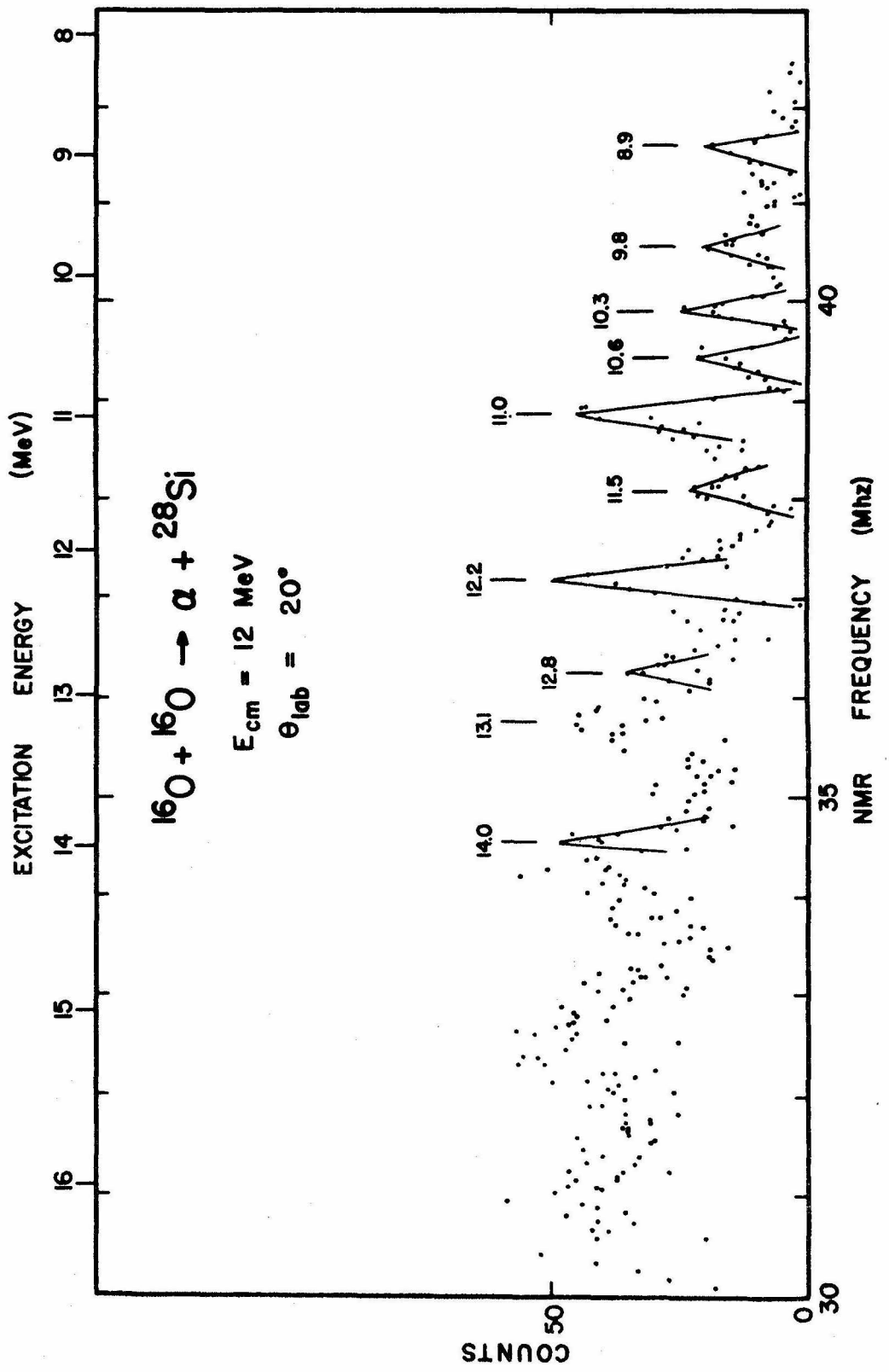
$^{16}O + ^{16}O \rightarrow \alpha + ^{28}Si$
E_{cm} = 12 MeV
θ_{lab} = 20°
EXCITATION ENERGY (MeV)
8
9
10
11
12
13
14
15
16
14.0
13.1
12.8
12.2
11.5
11.0
10.6
10.3
9.8
8.9
COUNTS
50
0
30
35
40
NMR FREQUENCY (Mhz)

With the counter telescope of Figure 13 only a limit on the number of deuterons could be obtained because of the poor proportional counter resolution. Figure 18 shows the ΔE distribution of counts for $E_{counter} = 3.3$ MeV from Figure 15. An approximate energy scale is also shown. The width of the proton and alpha lines can be calculated assuming a Gaussian distribution of energy losses. The observed FWHM are 25 keV and 80 keV for protons and alphas respectively, whereas the calculated values are 20 keV and 40 keV. At this value of $E_{counter}$ the multiple collisions determine the energy loss distribution (a Gaussian), but a Landau distribution (see Moyal (1955) and Landau (1944)) must be used for proton energies above about 4 MeV, where single collisions appreciably influence the losses. The expected position of deuterons, tritons and ^{3}He's is also shown in the figure. The lack of a definite line at these points indicates that few of these particles are present. Cross section limits on the production of d's, t's and ^{3}He's were computed by summing counts near the expected lines. The tails from the proton and alpha lines obscure any deuterons, etc. present, and in the data analysis all counts were assumed to be either protons or alphas.

A second particle telescope was constructed specifically to separate deuterons from protons. The construction was similar to that of the other telescope, except that a 58 μ (150 mm^2 in area) silicon transmission counter served to measure ΔE and a 3 mm by 110 mm^2 lithium drifted silicon detector measured E. The thicker ΔE counter was essential to obtain a better relative energy resolution so

Figure 18

Spectrum of ΔE Counts in the

Charged Particle Spectra.

The number of counts in the two dimensional spectrum of Figure 15 at $E \approx 3.3$ MeV are plotted against the ΔE channel. An approximate energy scale based on the expected proton and alpha energy losses in the proportional counter is also shown. The expected positions of deuterons, tritons and ^{3}He's are indicated.

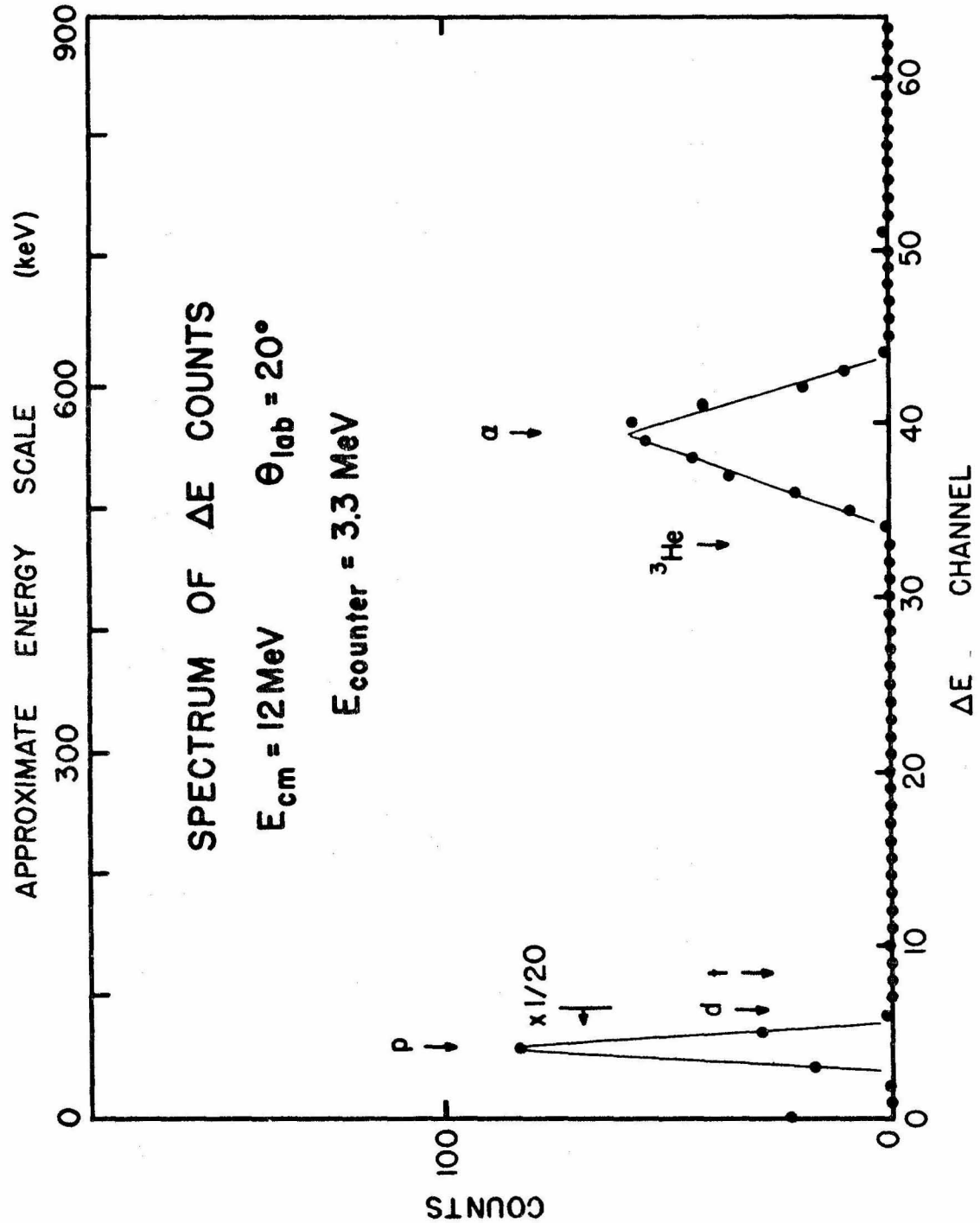
APPROXIMATE ENERGY SCALE (keV)
0
300
600
900
SPECTRUM OF ΔE COUNTS
E_{cm} = 12 MeV
θ_{lab} = 20°
$E_{counter}$ = 3.3 MeV
p
x1/20
d
t
α
^{3}He
COUNTS
100
0
0
10
20
30
40
50
60
ΔE CHANNEL

the proton line would not obscure the deuterons. Both counters were kept under vacuum to prevent electrical breakdown of the Si (Li) counter bias of 500 V in the target gas. The entrance foil was 2.1 mg/cm^2 aluminized mylar and a 3.4 mg/cm^2 aluminum foil could be moved before the entrance slit to stop elastically scattered Oxygen. The angular opening was $\pm$ 4.9^o and the geometrical factor was

$$\langle \Omega L \rangle_{90^o} = (1.23 \pm 0.04) \times 10^{-3} \text{ cm sr.}$$

No attempt was made to experimentally check the ratio of this value to the monitor counter solid angle factor.

The ΔE and E gains were matched to about 0.5% and the pulses then fed into an Ortec Particle Identifier (see Figure 19). One of its outputs was the sum of the E and ΔE pulses, and the other was an identifier pulse proportional to $(E + \Delta E)^{1.73} - E^{1.73}$, a quantity empirically dependent only on the type of particle. Deuterons clearly separated from the protons were observed, however a search for ^{3}He and ^{3}H was again unsuccessful. The spectrum of deuterons at E_{cm} = 11.85 MeV and $\theta_{lab} = 25^o$ is given in Figure 20. Note that many levels in ^{30}P are easily resolved, and there is no large increase in counts at the low particle energies characteristic of the proton and alpha spectra (Figure 16). Yields of protons and alphas leading to states of low excitation energy in the residual nuclei, as obtained from the two counter telescopes, agreed within experimental errors.

Figure 19

Particle Identifier Electronics.

This setup was used for the solid state counter telescope. It was also successfully employed to separate alphas from protons with the counter telescope illustrated in Figure 13, even though the E and ΔE gains were not appropriately matched.

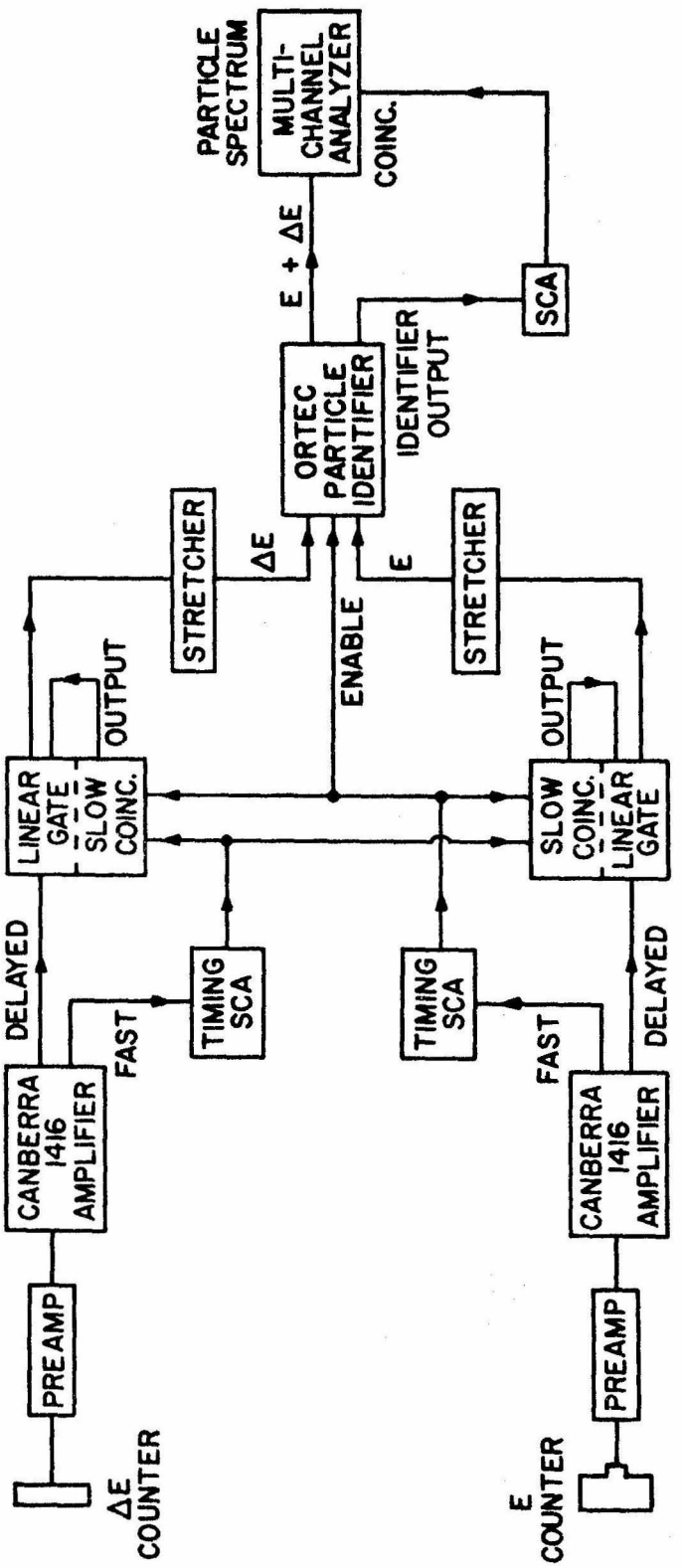
PARTICLE SPECTRUM
MULTI-CHANNEL ANALYZER
COINC.
E + ΔE
SCA
ORTEC PARTICLE IDENTIFIER
IDENTIFIER OUTPUT
STRETCHER
ΔE
ENABLE
E
STRETCHER
LINEAR GATE SLOW COINC.
OUTPUT
SLOW COINC. LINEAR GATE
OUTPUT
DELAYED
FAST
TIMING SCA
TIMING SCA
FAST
DELAYED
CANBERRA 1416 AMPLIFIER
CANBERRA 1416 AMPLIFIER
PREAMP
PREAMP
ΔE COUNTER
E COUNTER

Figure 20

Deuteron Spectrum.

The solid state counter telescope and the particle identifier were used to obtain this spectrum. It corresponds to the highest bombarding energy and most forward angle of all the deuteron data taken. Note that the number of counts does not strongly increase at low energies in contrast to the spectrum shape seen for alphas and protons in Figure 16.

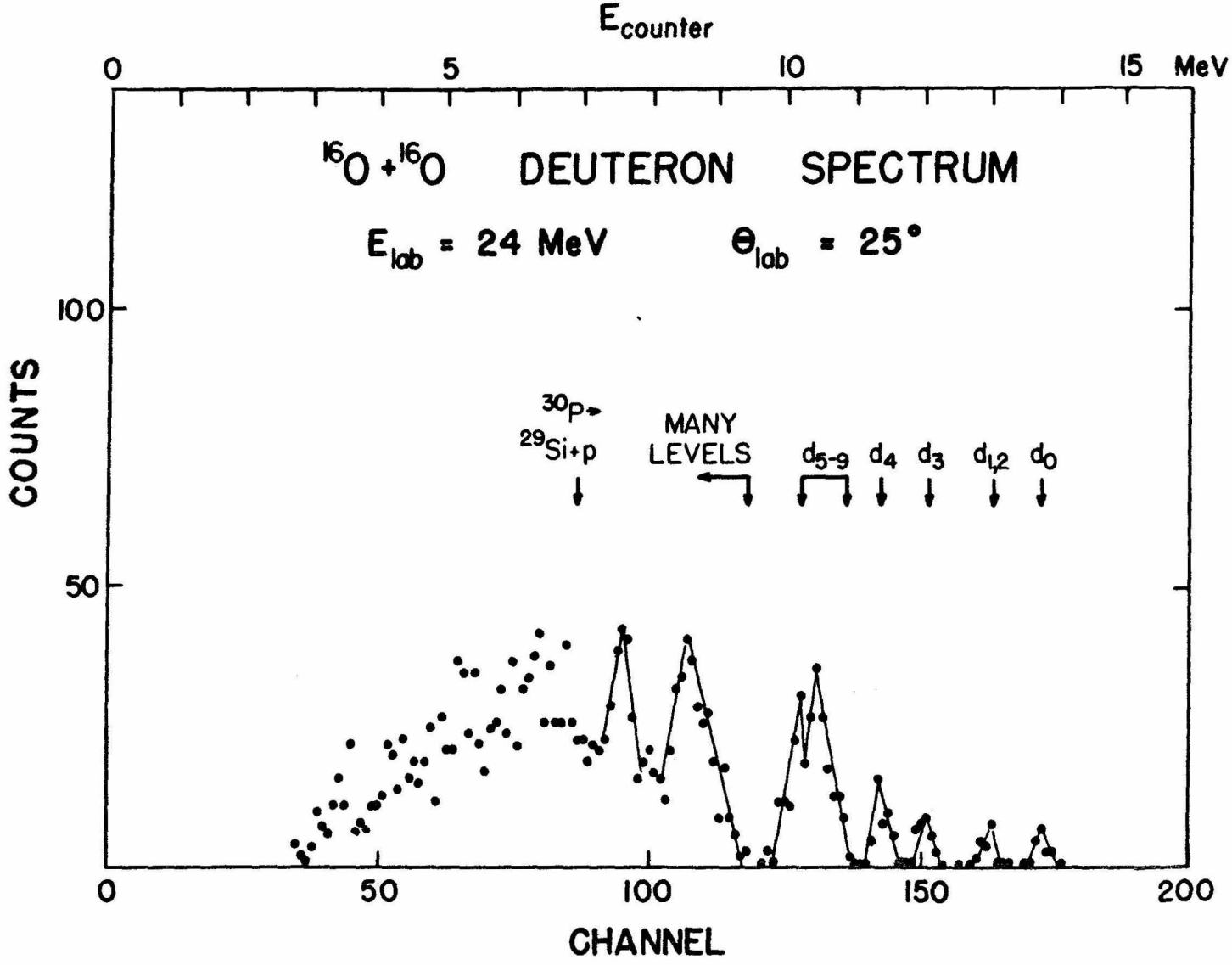
E counter
0
5
10
15 MeV
16O + 16O DEUTERON SPECTRUM
Elab = 24 MeV
θlab = 25°
100
50
COUNTS
30P→
29Si+p
MANY
LEVELS
d5-9
d4
d3
d1,2
d0
0
50
100
150
200
CHANNEL

The charged particle data taken using the counter telescope (proportional counter ΔE) involved many days of running. Up to 14 angles were taken at one energy with runs lasting 15 minutes to 18 hours each. Beam currents were typically 4 to 12 μa of $4+$ ^{16}O. Counts in each spectrum varied from 47 alphas at $E_{cm} = 6.8$ MeV and $\theta_{lab} = 40^{\circ}$, up to 34,000 protons at $E_{cm} = 11.85$ MeV and 20°.

Data Analysis

From the spectra taken, angular distributions in the C.M. and laboratory systems were derived and total production cross sections were determined in two ways. The first method involved transforming all quantities to the C.M. system using a computer program written for the purpose. The analysis proceeded as follows:

1) Energy losses were calculated for the foil thicknesses and gas pressures used in the proportional counter and target chamber.

2) The energy calibration ($E_{counter}$ vs. channel) and energy losses gave the energy of the particle when emitted in the target region, E_3, for each channel.

3) Knowledge of the bombarding energy E_{in}, laboratory angle θ_{lab} and E_3 permitted calculation of the center-of-mass angle θ_{cm}, of the excitation energy in the corresponding heavy particle (^{28}Si, ^{31}P, etc.) E_{exc}, and of the conversion factor between the laboratory and C.M. differential cross sections (C.M. Factor = $d\sigma/d\Omega)_{cm}/$

$d\sigma/d\Omega)_{lab}$) from relativistic kinematics. The three body decays, for which this statement might not be correct, will be discussed later.

4) From measured quantities and counts in the spectra, differential cross sections were then computed from the relation

$$\left(\frac{d\sigma}{d\Omega}\right)_{cm} = \left(\frac{d\sigma}{d\Omega}\right)_{\substack{cm \\ el.sc.}} \cdot \left(\frac{CMF_{telescope}}{CMF_{monitor}}\right) \cdot \left(\frac{\sin\theta_{lab,\,telescope}}{\sin 45^{o}}\right) \cdot \left(\frac{N_{telescope}}{N_{monitor}}\right) \cdot \left(\frac{\langle \Omega L\rangle_{monitor,\,90^{o}}}{\langle \Omega L\rangle_{telescope,\,90^{o}}}\right) .$$

Note that these differential cross sections are integrated over the excitation energy span of the particular channel in the spectrum. The energy calibration for the alpha spectra was checked at this point by plotting $d\sigma/d\Omega)_{cm}$ against E_{exc} for several different laboratory angles, as in Figures 21-24. The peaks in these spectra have the same value of E_{exc} as observed in the spectrum of Figure 17 taken with the spectrometer. The protons showed structure too, but the peaks were not as pronounced.

5) Differential cross sections for larger intervals of E_{exc}, namely for E_{exc} = 0-5, 5-7.5, 7.5-10, etc. MeV were

Figures 21 - 24

Alpha and Proton Spectra vs. E_{exc}.

The values of $"\left(\frac{d\sigma}{d\Omega}\right)_{cm}"$ are plotted against the excitation energy, E_{exc}, for alphas and protons at E_{cm} = 7.85 and 11.85 MeV. Data from spectra taken at several different angles are presented in each figure to show that the peaks occur at fixed values of E_{exc}. At the lower bombarding energies the percentage of particles from these peaks increases. Note that $"\left(\frac{d\sigma}{d\Omega}\right)_{cm}"$ corresponds to the integrated differential cross section over the particular channel in the spectrum. The region of extrapolated counts is also given.

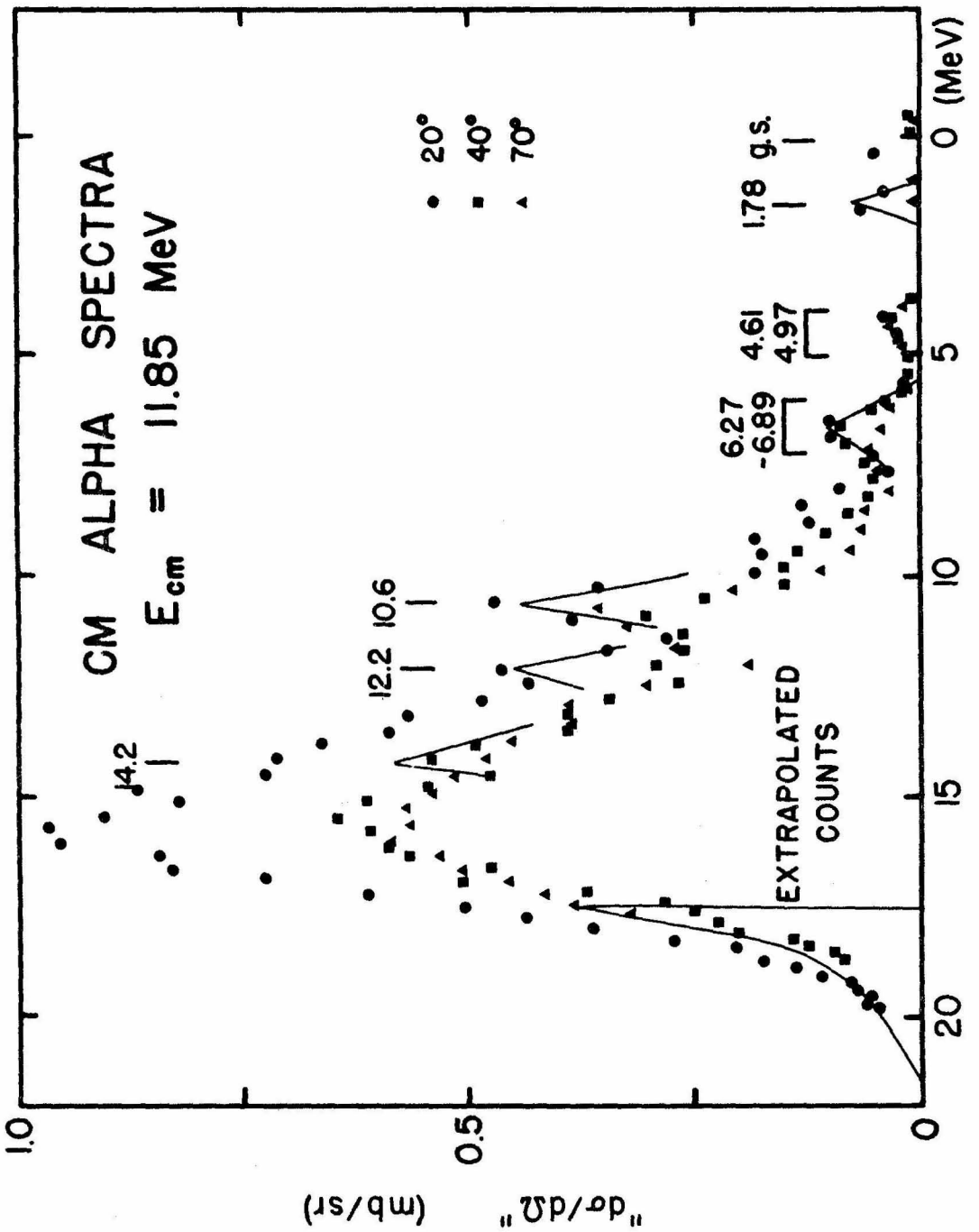
CM ALPHA SPECTRA
E_{cm} = 11.85 MeV
20°
40°
70°
14.2
12.2
10.6
6.27
-6.89
4.61
4.97
1.78 g.s.
EXTRAPOLATED COUNTS
"dσ/dΩ" (mb/sr)
1.0
0.5
0
20
15
10
5
0 (MeV)
EXCITATION ENERGY

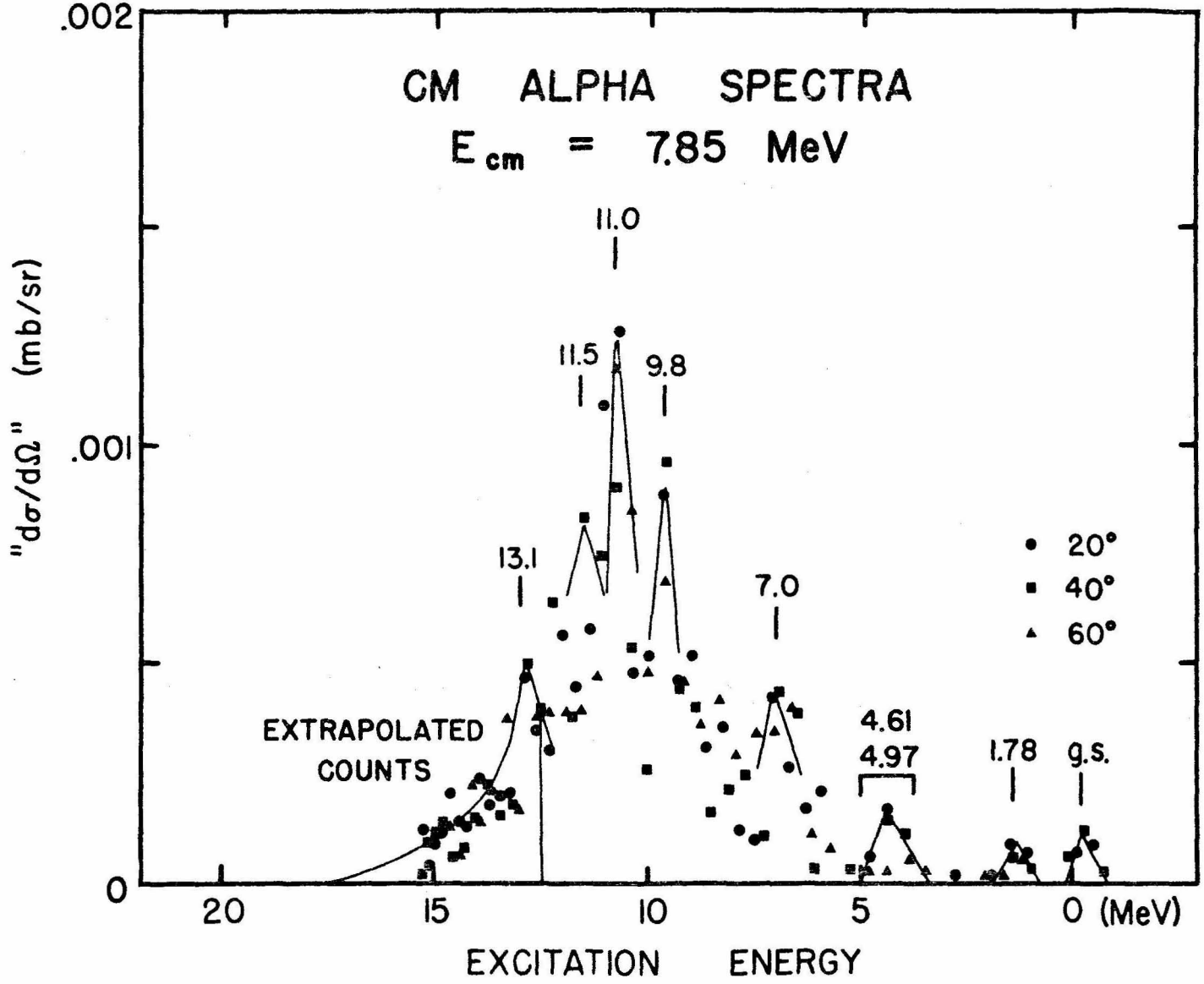
CM ALPHA SPECTRA
E_{cm} = 7.85 MeV
"dσ/dΩ" (mb/sr)
.002
.001
0
11.0
11.5
9.8
13.1
7.0
4.61
4.97
1.78
g.s.
EXTRAPOLATED COUNTS
20°
40°
60°
20
15
10
5
0 (MeV)
EXCITATION ENERGY

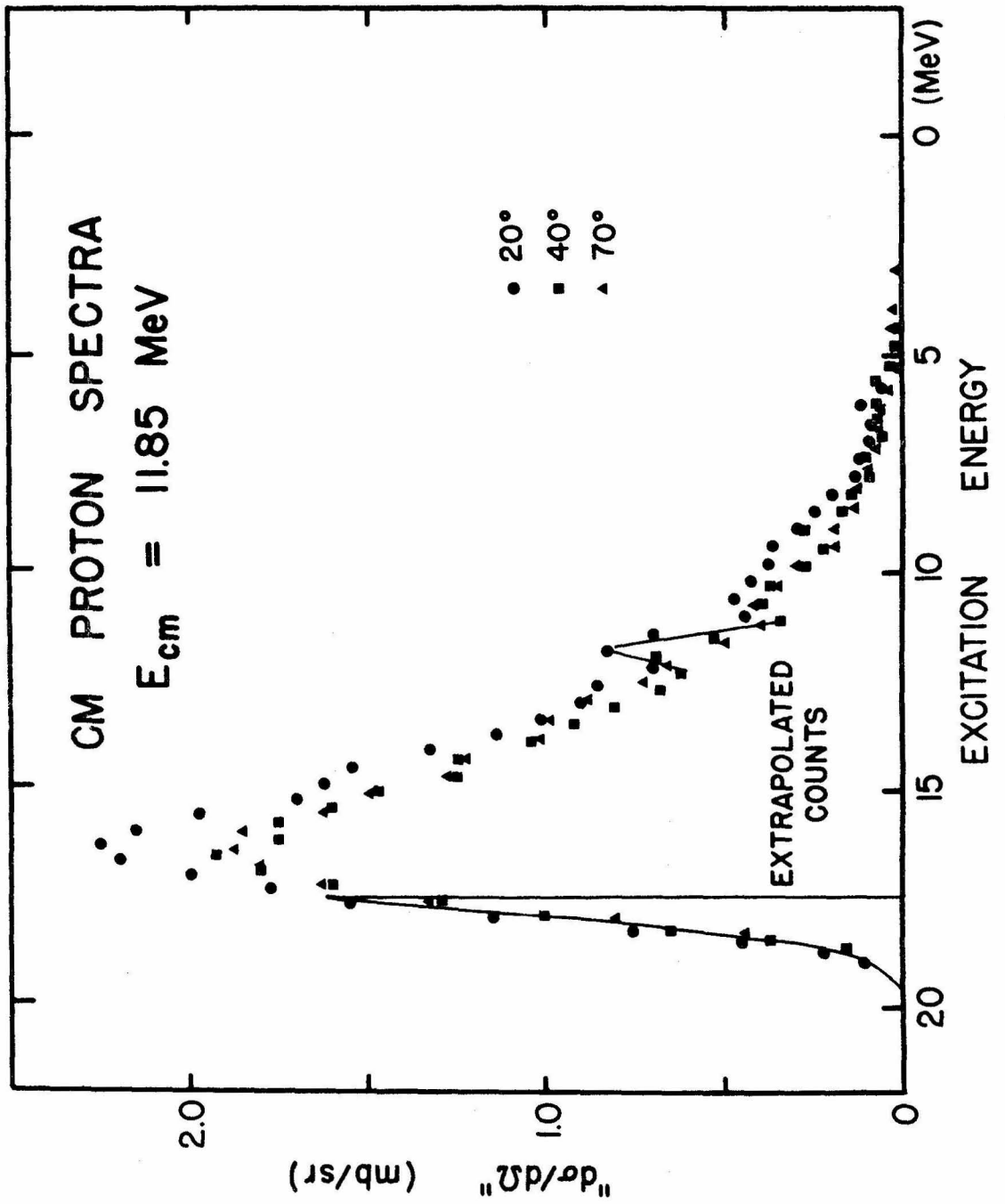
CM PROTON SPECTRA
E_{cm} = 11.85 MeV
20°
40°
70°
EXTRAPOLATED COUNTS
"dσ/dΩ" (mb/sr)
2.0
1.0
0
20
15
10
5
0 (MeV)
EXCITATION ENERGY

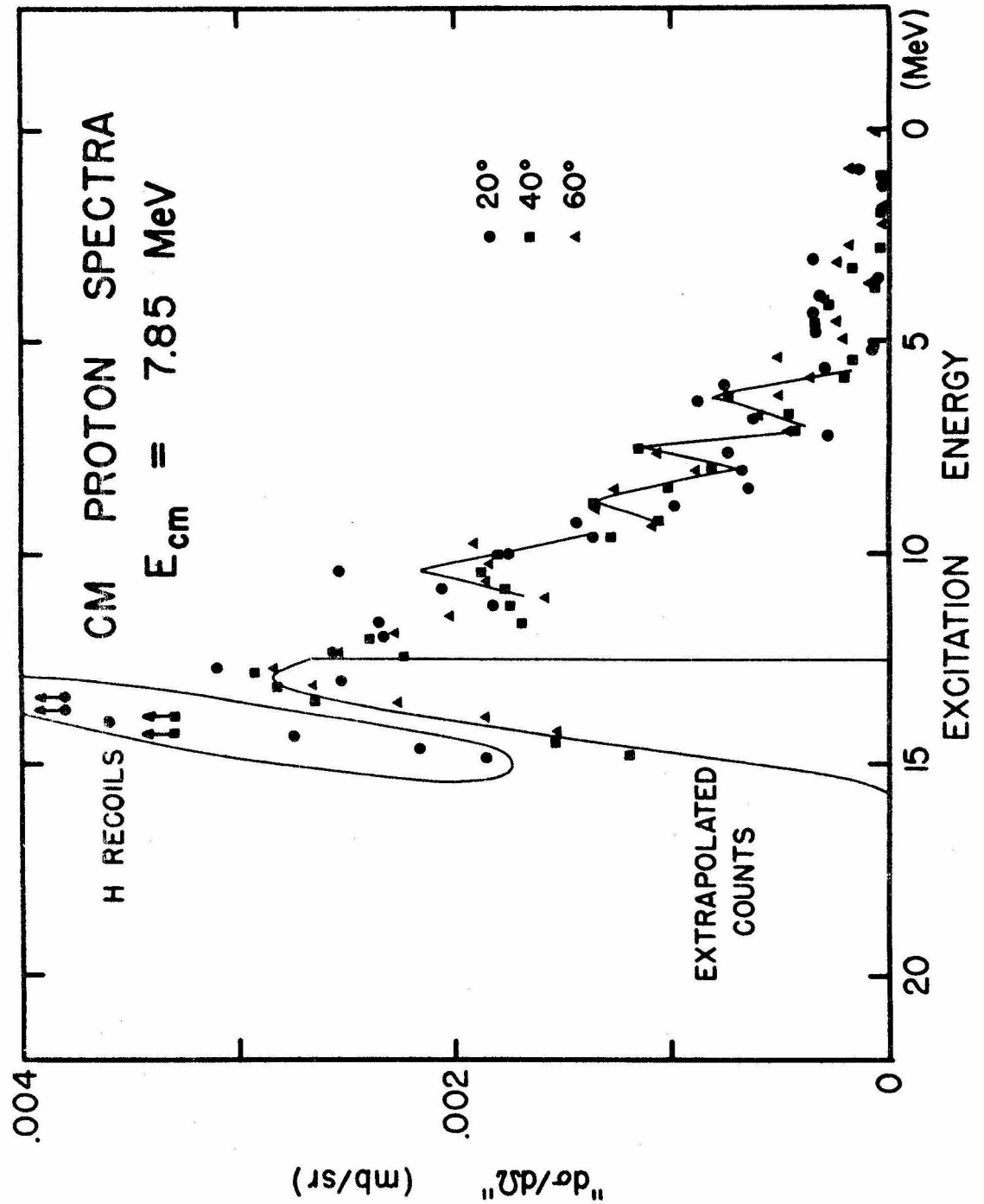
CM PROTON SPECTRA
E_{cm} = 7.85 MeV
20°
40°
60°
H RECOILS
EXTRAPOLATED COUNTS
"dσ/dΩ" (mb/sr)
.004
.002
0
20
15
10
5
0 (MeV)
EXCITATION ENERGY

then computed by summing $d\sigma/d\Omega)_{cm}$ from step 4 over the appropriate channels and linearly interpolating the counts at the ends of the interval.

6) Relative errors on the differential cross sections as computed in step 5 were composed of:

a) statistical errors on $N_{telescope}$ and $N_{monitor}$.

b) an error associated with the variation of the C.M. Factor over the angular opening of the counter telescope ($\pm 3.9^{o}$). The change in the C.M. Factor over this angle was typically 3-12% depending on the excitation energy and laboratory angle.

c) an error to allow for uncertainties in the energy calibration. Since the calibrations were believed to be good to ± 0.5 channels, an additional error to the counts $N_{telescope}$ was assigned to be half the number of counts in the channel at each end of the interval summed. The corresponding uncertainty in E_3 is roughly $\pm$ 200 keV. The largest contributions to the relative error were normally the last two, but at the lowest energies the statistical uncertainties on the number of counts $N_{telescope}$ predominated.

Table 6 gives the results of these calculations along with the relative errors. At several bombarding energies and laboratory angles more than one run was taken, primarily as a cross check between the many running days used to gather the data. Differential

cross sections for each interval in E_{exc} for these runs were always consistent within the appropriate errors. Instead of each individual measurement, weighted averages of such data are given in Table 6.

The angular distributions were found to be symmetric about $\theta_{cm} = 90^{o}$ within the relative errors in almost all cases (see Figure 25). For identical beam and target particles, they should be strictly symmetric if the computation of the C.M. angle and C.M. Factor is correct (as it is for all two body reactions). For the interval $E_{exc} = 0 - 5$ MeV the alphas, and to a lesser extent the protons as well, show structure in the angular distributions. The structure is not present at higher excitation energy intervals probably because of the larger number of excited states in these intervals. The protons have a generally shallower angular distribution than the alphas, but both are peaked in the forward and backward directions.

Based on the symmetry about $\theta_{cm} = 90^{o}$, too few low energy (close to the detection limit) proton and alpha counts were detected at backward angles compared to forward angles. This was mainly true for the first two or three channels in the particle spectra ($E_{counter} < 1.5$ MeV) and was attributed to multiple scattering. Whenever particles corresponding to a certain range in E_{exc} appear in channels 1 to 3 of the E spectrum at very backward laboratory angles, the same range of E_{exc} will give particles of much higher energy at forward angles. This is for purely kinematic reasons. Since the low energy particles at the backward angles undergo fairly

Figure 25

Proton and Alpha Angular Distributions.

Average differential cross sections for restricted excitation energy intervals are plotted for alphas and protons at E_{cm} = 8.85 MeV from Table 6. The average differential cross section (value of A , see the text page 102) from the Legendre polynomial fit is shown for each excitation energy interval. In general, the angular distributions are symmetric about $\theta_{cm} = 90^{o}$ and are flatter at higher excitation energies.

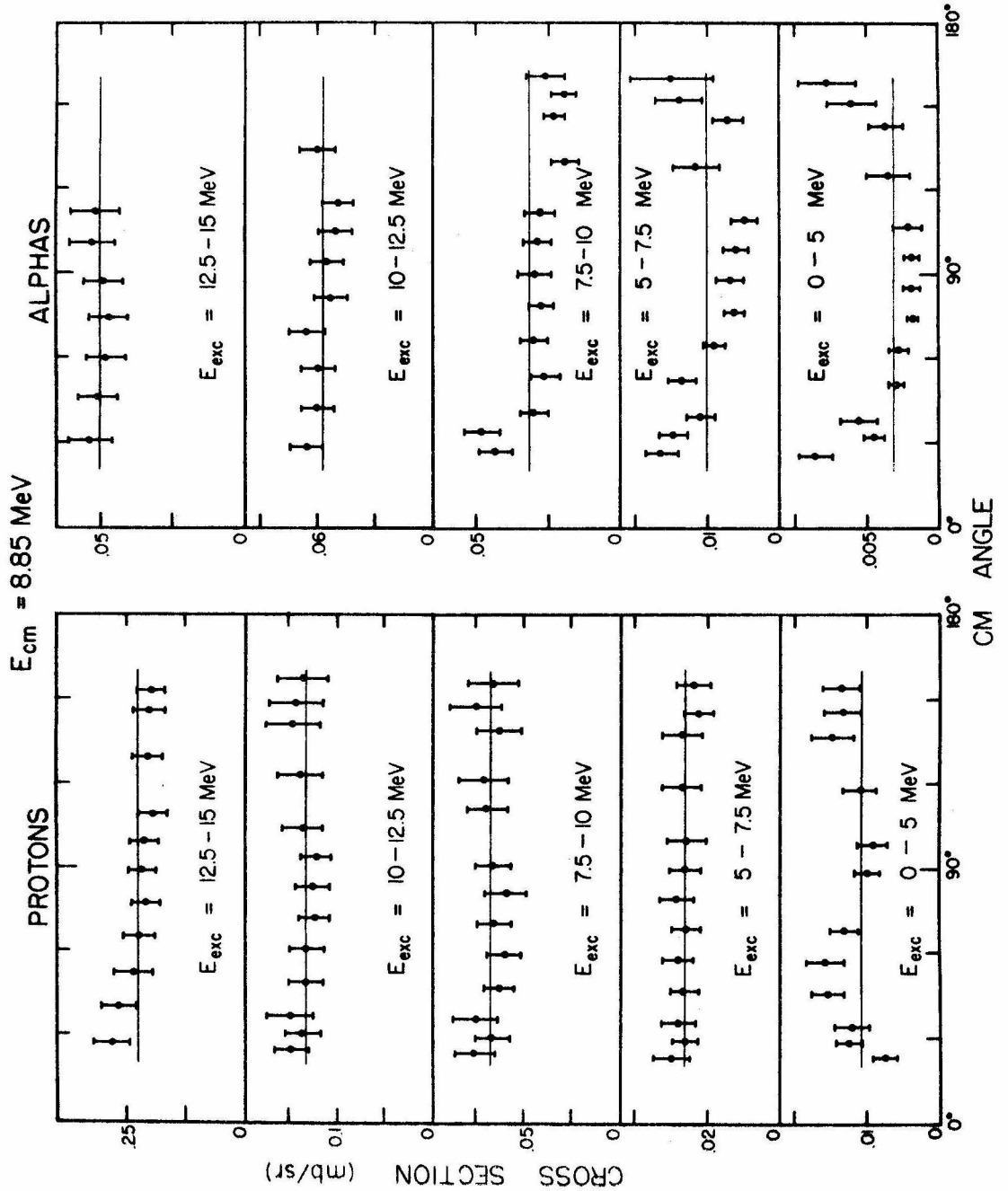
PROTONS
ALPHAS
E_{cm} = 8.85 MeV
E_{exc} = 12.5 - 15 MeV
E_{exc} = 10 - 12.5 MeV
E_{exc} = 7.5 - 10 MeV
E_{exc} = 5 - 7.5 MeV
E_{exc} = 0 - 5 MeV
CROSS SECTION (mb/sr)
CM ANGLE
0°
90°
180°

strong multiple scattering, whereas the higher energy ones do not, the angular distribution may be distorted (the backward angle data then being incorrect). The size of the loss of counts is difficult to calculate theoretically because of the complicated detection geometry and the presence of material all along the path from the target to the E counter. Outside the entrance slit to the counter telescope the particles lost by multiple scattering can be compensated by other particles scattering into the path through the telescope. However, multiple scattering in the 10,000 Å nickel entrance foil or Argon gas may result in a net loss of particles detected. The counter telescope entrance slit could prevent compensating particles from scattering into the telescope. Assuming that the Argon gas is concentrated at the nickel entrance foil and that the multiple scattering angular distribution is Gaussian (see Marion and Zimmerman (1967)), the estimated loss of particles is 15% for $E_{p,\text{counter}} \sim 1.2$ MeV and $E_{\alpha,\text{counter}} \sim 2.5$ MeV. Intervals in E_{exc} which contain counts from the first three channels in the particle spectra were not included in Table 6.

The counts analyzed by this method were assumed to be totally the result of two body exit channels ($^{31}P + p$, $^{28}Si + \alpha$ or $^{30}P + d$). Particles from a three body breakup may have been incorrectly analyzed for obtaining production cross sections. If the three particles are ejected "instantaneously" after the reaction with no interactions between them, the analysis is correct. This follows from the dependence of θ_{cm}, E_{cm} and the C.M. Factor

$$\text{C.M. Factor} = \frac{d\sigma/d\Omega)_{cm}}{d\sigma/d\Omega)_{lab}} = \frac{d\Omega_{lab}}{d\Omega_{cm}} = \frac{d(\cos\theta_{lab})}{d(\cos\theta_{cm})}$$

only on θ_{lab}, E_{lab} and the velocity of the center-of-mass of the system. In the absence of final state interactions, these quantities do not depend on the variables of the other particles emitted. However, in the presence of such interactions the quantities θ_{cm}, E_{cm}, C.M. Factor may be incorrect. For example, in the reaction $^{16}O + {}^{16}O \rightarrow {}^{30}Si + 2p$, if there is a compound nucleus formed which first emits one proton and later emits the second (the final state interaction being between the second proton and ^{30}Si), then the center-of-mass velocity for the second "evaporation" is not the same as the center-of-mass velocity for the $^{16}O + {}^{16}O$ system. Hence the program would derive the wrong values of θ_{cm}, E_{cm}, and C.M. Factor for the second particle emitted. The assigned excitation energy

$$E_{exc} = \tfrac{1}{2} \cdot E_{^{16}O,\,lab} + Q_{g.s.} - E_{cm}$$

was not correct for the resulting nucleus ^{30}Si.

Total cross sections for each interval in E_{exc} were computed by fitting the angular distributions with Legendre polynomials

$$\frac{d\sigma}{d\Omega}\Big)_{cm} = AP_0(\cos\theta_{cm}) + BP_2 + CP_4 + \ldots$$

$$\sigma_{production} = 4\pi A$$

Only even L values were used since the bombarding and target particles were identical. The number of terms taken was 5 or k - 2, with k the number of different angles, whichever was less. The value of A and its error from the fit also appear in Table 6. Whenever there were only three or fewer angles, the angular distribution was taken to be isotropic and an average was used for the differential cross section A. The assigned error on such values of A was taken to cover the individual values of $d\sigma/d\Omega)_{cm}$ or to be 20%, whichever was larger. For conditions typical of cases where data at only a few angles were available, namely high excitation energies and low bombarding energies, the angular distributions have a typical variation of ± 10 - 30% over all angles. The 20% error on A mentioned above was assigned from this variation in $d\sigma/d\Omega)_{cm}$ with angle.

To obtain total production cross sections, the number of low energy particles stopped in the target chamber gas, foils and proportional counter gas, and therefore lost, had to be estimated. This was done by making a linear extrapolation from $N_{telescope}$ (in channel 2 or 3) counts at E_3 (channel 2 or 3) to 0 counts at $E_3 = 0$. The number of counts lost was taken to be $(N_{extrap} \pm N_{extrap})$. In addition, Hydrogen recoils from $^{16}O + {}^{1}H$ elastic scattering were identified as a contaminant at forward laboratory angles and lower bombarding energies (for an estimate of the Hydrogen contamination in the target gas, see the Elastic Scattering Section). Kinematically these protons have a maximum energy of $E_{lab} = 5.3$ MeV at a ^{16}O bombarding energy of 24 MeV and a maximum laboratory angle of

90^{o}. The Hydrogen recoil peak was easily identifiable in the proton spectra, and the number of protons from $^{16}O + ^{16}O$ reactions beneath the peak was also determined by a linear extrapolation. From the extrapolated counts and counts in the spectrum above the highest interval in E_{exc}, the differential cross section $d\sigma/d\Omega)_{cm,extrap}$ was computed. The values $4\pi A$ and $4\pi\, d\sigma/d\Omega)_{cm,extrap}$ are summarized in Table 7. The errors given include the fitted or estimated errors on the average differential cross sections, a 2% error on the Mott scattering cross section, an estimated 15% error for losses by multiple scattering, and a 4% error for the solid angle factor ratio. The total production cross sections are also given (see Figure 26).

As an independent check on the precision of these cross sections, the data at 4 energies were analyzed using a different method. Laboratory cross sections were computed from

$$\left(\frac{d\sigma}{d\Omega}\right)_{lab} = \left(\frac{d\sigma}{d\Omega}\right)_{\substack{cm \\ el.sc.}} \cdot \left(\frac{\sin\theta_{lab,\,telescope}}{\sin 45^{o} \cdot CMF_{monitor}}\right) \cdot \left(\frac{\langle\Omega L\rangle_{monitor,\,90^{o}}}{\langle\Omega L\rangle_{telescopt,\,90^{o}}}\right) \cdot \left(\frac{N_{tot}}{N_{monitor}}\right)$$

with $N_{tot} = N_{telescope} + N_{extrap}$. The same errors as above were applied, except that in this case the variation of the C.M. Factor over the angular opening of the counter telescope and the energy calibration errors, 6c), did not apply. At least 9 angles were taken at each of the energies and the results are given in Table 8. The total

Figure 26

Production Cross Sections for Protons,

Alphas and Deuterons.

The measured production cross sections and total errors are plotted as a function of E_{cm} from Table 7. Smooth lines have been drawn through the alpha and proton points. Energy losses have been taken into account and produce an overall uncertainty in the energy scale of ± 50 keV (C.M.).

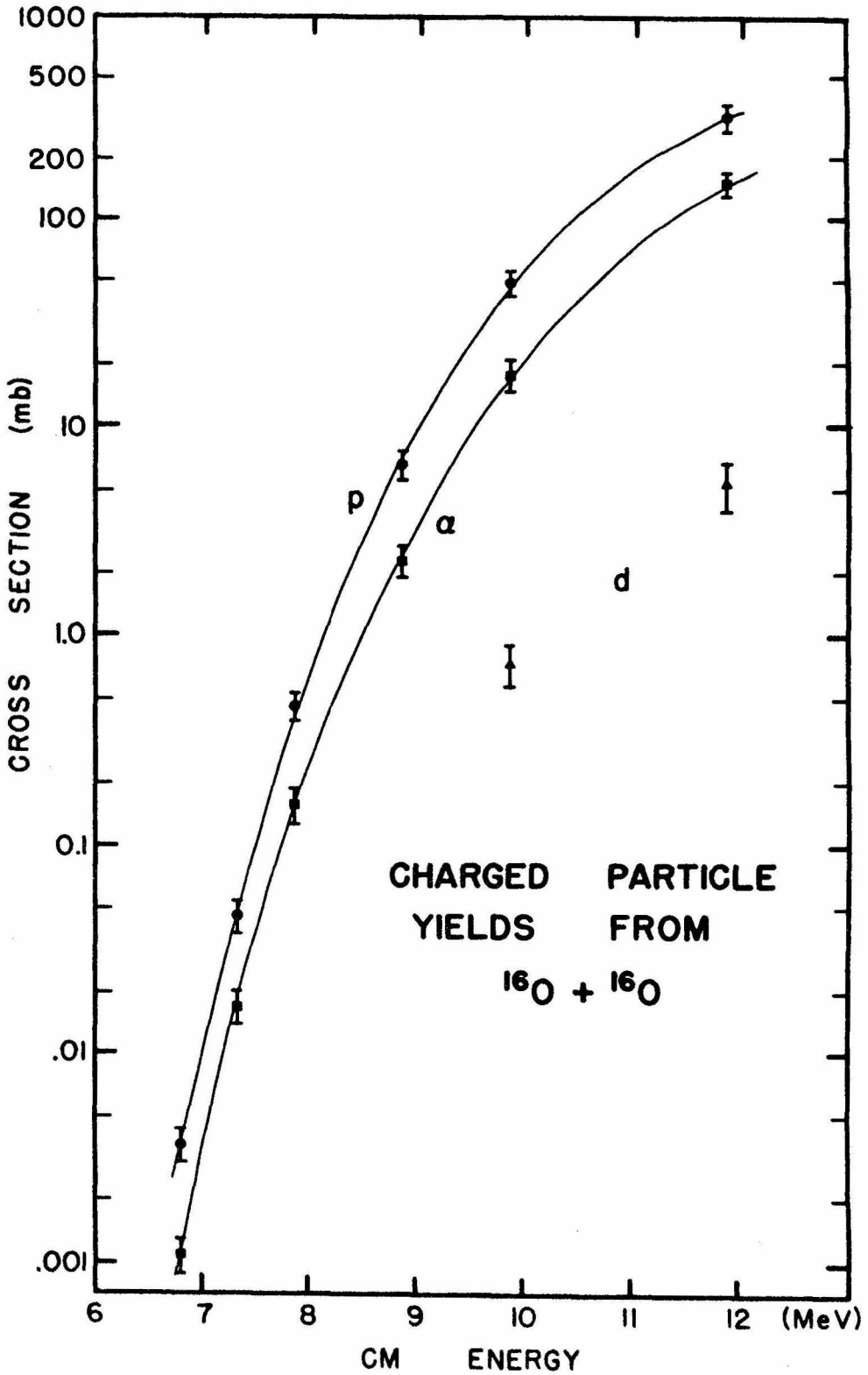
1000
500
200
100
10
1.0
0.1
.01
.001
CROSS SECTION (mb)
p
α
d
CHARGED PARTICLE
YIELDS FROM
16O + 16O
6
7
8
9
10
11
12
(MeV)
CM ENERGY

production cross sections were computed from a Legendre polynomial fit to the data

$$\frac{d\sigma}{d\Omega}_{lab} = AP_0(\cos\theta_{lab}) + BP_1 + CP_2 + \ldots$$

$$\sigma_{production} = 4\pi A$$

where all L values up to L = 5 were included (no symmetry about $\theta_{lab} = 90^o$ is required). The production cross sections and the total errors are also given in Table 7.

The agreement between the total cross sections from Tables 6 and 8 demonstrates that errors from the possible incorrect treatment of the three body reactions in the first method do not seriously affect the total production cross sections obtained. The same conclusion applies to any deuterons (or ^{3}He or ^{3}H counts) included in the charged particle spectra which would not have been analyzed correctly. Thus the cross sections at $E_{cm} = 6.80$ and 7.32 MeV are also expected to be correct, even though data were taken at only a few angles.

The production cross sections (for p's etc.) are an upper limit to the actual reaction cross sections (for $p + {}^{31}P$, $2p + {}^{30}Si$, etc.). A lower limit is obtained by counting all protons or alphas with energies below the respective three body cutoffs as though they all came from three body exit channels. This was done at 4 energies (see Table 9, lower limit I). A better estimate of the lower limit

used the same procedure except that counts in the peaks of the alpha and proton spectra (see Figures 16, 17) were taken to be from two body reactions, giving the cross sections listed as "lower limit II." The upper limit was reduced by subtracting out known three body decays. This is discussed in the Conclusions.

ACTIVATION METHOD

Introduction

Cross sections for three exit channels in $^{16}O + ^{16}O$ reactions were measured by an activation method with 2π counting geometry. The nuclei ^{31}S and ^{30}P from $^{16}O(^{16}O,n)^{31}S$, $^{16}O(^{16}O,d)^{30}P$ and $^{16}O(^{16}O,pn)^{30}P$ were collected on a catcher foil on the surface of a plastic scintillator. The beam was then turned off and β particles from ^{31}S and ^{30}P were detected in the scintillator as a function of time. The decay curves were analyzed using the halflives of these nuclei to separate the two activities. Unfortunately, the presence of other β activities from undesired reactions complicated the analysis.

Experimental

The experimental setup is shown in Figure 27. The ^{16}O beam was passed through slits and a 1.1 cm diameter hole in a 5 cm thick lead block before hitting the SiO foil target. The lead shielded the scintillator from radioactivity on the defining slits. The heavy reaction products passed through the SiO foil and were collected on a gold covered aluminum foil in front of the scintillator. There were alternate bombarding periods when the photomultiplier was turned off, and counting periods when the number of β's from the radioactive decays were measured as a function of time. The combined beam intensity and target thickness was monitored by observing $^{16}O + ^{16}O$

Figure 27

Experimental Setup for the Activation Method.

The activation measurements were made by first bombarding the SiO foil target with the ^{16}O beam. Heavy nuclei formed in $^{16}O + ^{16}O$ reactions passed through the target and were collected on the aluminum catcher foil. Elastically scattered particles were counted in the solid state detector at 45°. Then the beam was turned off and β particles from radioactive reaction products on the catcher foil were detected with the Pilot B scintillator. Lead was used to shield against room background and radiation from the entrance slits.

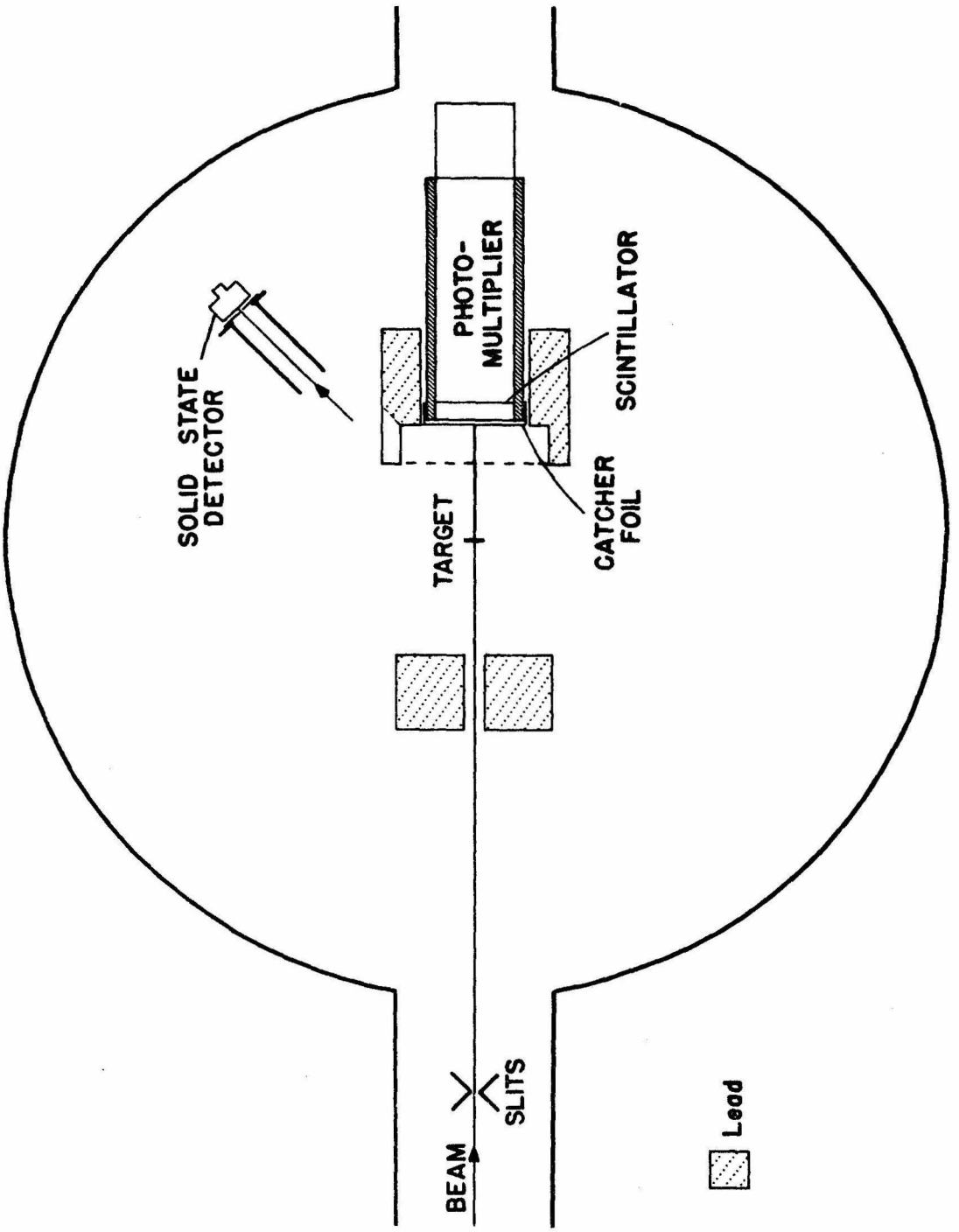
SOLID STATE DETECTOR
PHOTO-MULTIPLIER
SCINTILLATOR
TARGET
CATCHER FOIL
BEAM
SLITS
Lead

elastic scattering at $\theta_{cm} = 90^{o}$ as described in the Elastic Scattering Section. Typical beam currents were 300 to 500 na of O^{4+}, and total times per measurement were 10 minutes to 5 hours.

The targets used were 20 - 40 μ gm/cm^2 SiO foils and were about 150 - 350 keV thick to 18 MeV ^{16}O beams. They were made by evaporating optical grade SiO onto a layer of 10 μ gm/cm^2 BaCl on a glass slide. The amount of SiO deposited was estimated using a quartz crystal thickness monitor. Foils were then floated off in distilled water and mounted on tantalum target holders. The target thickness was measured with the 61 cm double focusing magnetic spectrometer. A very low intensity and diffuse ^{16}O beam was passed through a pinhole in 0.012" tantalum and then analyzed by the spectrometer set at 0.5 - 1.5^{o}. When the SiO foil was placed between the pinhole and the magnet, the ^{16}O beam had a lower energy which could be directly measured on the spectrometer. To measure the target thickness, the beam was first scattered from a nickel foil or from Argon gas in the differentially pumped gas target into a detector. Then the SiO foil was placed before the nickel or Argon and the energy shift in the scattered ^{16}O gave the target thickness.

At the lowest bombarding energy, E_{lab} = 15 MeV, the minimum recoil ^{31}S and ^{30}P energies are 4.7 and 4.4 MeV respectively. The SiO target was < 3.2 MeV thick (estimated from Northcliffe (1963)) to such nuclei created at the front surface of the foil. Experimentally, no difference in yield was noted for the

different thickness foils used, confirming that the ^{31}S and ^{30}P were not stopped before reaching the detector.

The maximum recoil angle of ^{31}S was 11.5^{o} and of ^{30}P was 14.0^{o} with respect to the incoming beam direction. Maximum deflections of 1^{o} could occur from γ decay of ^{31}S or ^{30}P excited states while in flight, and the multiple scattering angle for these nuclei in the SiO foil was $\langle \theta^2 \rangle^{\frac{1}{2}} < 24^{o}$. These effects suggest that the heavy nuclei should be mostly confined to a cone of half angle $< 30^{o}$. In the experiment, the aluminum foil and scintillator subtended a cone of half angle 33^{o} as seen from the target. However, the yield was checked as a function of the half angle subtended by the scintillator and catcher foil over a range of 16.5 to 36.0^{o}. Total β yields were found constant within 5%. Furthermore, it was experimentally demonstrated that more than half the radioactivity was emitted within a cone of half angle 6.2^{o}. A cylindrical disk of tantalum 0.8 cm in diameter by 0.4 cm thick was placed at the center of the catcher foil. The disk was thick enough to stop all β particles from radioactive nuclei deposited on it, and the β yields were lower by about 50% with this arrangement. Therefore, almost all ^{31}S and ^{30}P were collected on the aluminum catcher foil.

Commercial 0.0015" aluminum foil with about 0.6 mg/cm^2 of gold evaporated on its surface served as the catcher foil. It was used as a light reflector for the scintillator and a beam stop as well. The Al_2O_3 layer on the aluminum surface is typically 40 - 100 Å (1.5 - 4 $\mu gm/cm^2$) thick. The gold insured that the ^{16}O beam had

lost sufficient energy by the time it reached the Al_2O_3 so that the Coulomb barrier prevented background counts from $^{16}O + ^{16}O$ reactions.

Background activation runs with the beam in but the target out were taken after every target-in run (see Figure 30). An Oxygen buildup in the catcher foil from bombardment with the beam contributed to the background. Four hours of continuous bombardment with 300 na beam would build up 7×10^{15} atoms of Oxygen, or 10% of the amount of Oxygen in a 20 μ gm/cm^2 SiO foil. Buildup of hydrocarbons from the pump oil and of other substances on the gold surface also might add background counts. To minimize background β counts from these sources, the catcher foil was changed periodically and measurements were made at decreasing bombarding energies. Higher energy ^{16}O beams penetrated deeper into the gold and aluminum and could not be reached later by lower energy beams. Also, a liquid Nitrogen trap was installed beneath the SiO foil to decrease Carbon buildup.

The scintillator was Pilot B optically bonded to an RCA - 8575 photomultiplier with Dow Corning #20-057 Optical Coupling Compound. The scintillator was 1.4 cm thick by 5.1 cm in diameter. The photomultiplier was chosen to fit inside the 61 cm scattering chamber, where the measurements were taken. The mounting of the scintillator on the photomultiplier was checked under vacuum for the presence of air bubbles which would affect the light collection efficiency. The scintillator and photomultiplier were shielded with

1.2 to 2.5 cm of lead, and the whole assembly was mounted on one of the moveable arms in the scattering chamber.

On the other arm was the monitor counter (usually a heavy ion surface barrier counter 75 μ thick and 100 mm^2 in area) with a typical solid angle of 3×10^{-4} sr. and angle subtended from the target of $\pm 0.7^{o}$. Before each series of runs the detector was moved to $\theta_{cm} = 90^{o}$ relative to the beam by maximizing the yield of elastically scattered Oxygen. A typical monitor spectrum is shown in Figure 28. The desired counts could be easily separated from the silicon recoils. The counts in the various peaks indicated that the ratio of Silicon to Oxygen in the target was nearly 1 to 1 and remained essentially constant after $\frac{1}{2}$ hour of continuous bombardment.

The desired activities were formed by:

	Q	$E_{\beta^+,max}$	$T_{\frac{1}{2}}$
$^{16}O + {}^{16}O \rightarrow {}^{31}S + n$	1.448 MeV	4.42 MeV	2.6 sec
$\rightarrow {}^{30}P + d$	-2.412	3.22	2.50 min
$\rightarrow {}^{30}P + p + n$	-4.636		

The major contaminant activity had a halflife of about 4 seconds and was probably ^{27}Si formed by

$^{16}O + {}^{12}C \rightarrow {}^{27}Si + n$	-0.422	3.79	4.2 sec

Other possibilities are

$^{16}O + {}^{16}O \rightarrow {}^{27}Si + \alpha + n$	-7.583	3.79	4.2 sec
$\rightarrow {}^{29}P + t$	-7.478	3.93	4.4

Figure 28

Monitor Spectrum for $^{16}O + SiO$.

This spectrum was taken at $E_{lab} = 20$ MeV, $\theta_{lab} = 45^{o}$ and shows that the desired $^{16}O + ^{16}O$ elastic counts were easily separated from $^{16}O + Si$ elastics or recoils (see the text page 115).

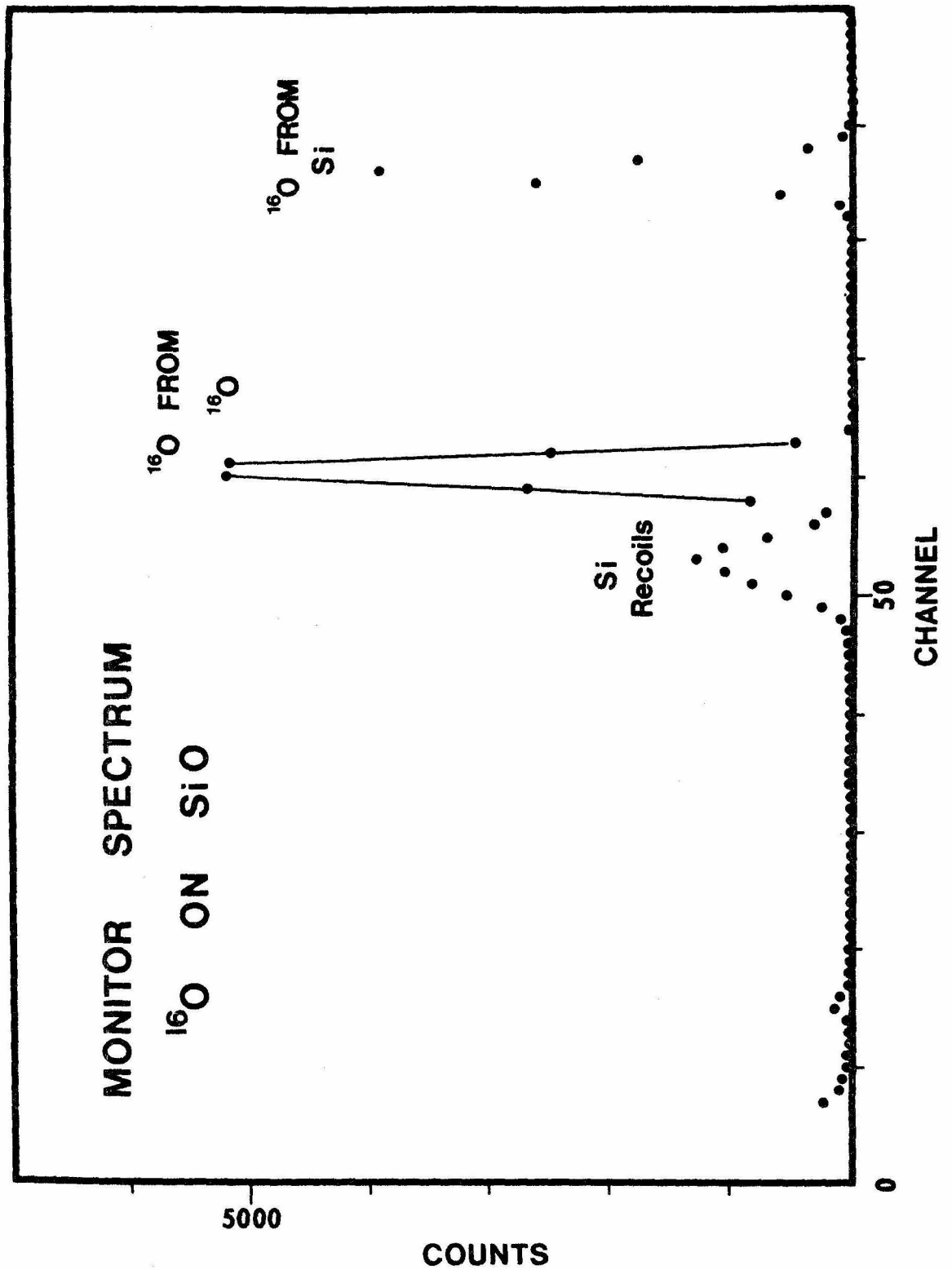
MONITOR SPECTRUM
^{16}O ON SiO
^{16}O FROM ^{16}O
^{16}O FROM Si
Si Recoils
5000
COUNTS
0
50
CHANNEL

Carbon contamination and subsequent Carbon buildup on the SiO target were suspected to be the main causes of the undesired activity. The 4 second activity yield varied for different target foils and increased as a function of time for a particular foil, suggesting that it did not come from ^{16}O + Si reactions. Measurements of the $^{12}C(^{16}O,n)^{27}Si$ cross section were made on Carbon foils with the same apparatus. If the 4 second contaminant activity was completely from this reaction, it would indicate a typical Carbon thickness of about 0.5 μ gm/cm^2. The contaminant yield was somewhat decreased by installing a cold trap beneath the SiO foil.

Oxygen bombardment of natural Silicon could yield several β activities with halflives of seconds to minutes. Those with $E_{threshold} < 18$ MeV (lab) are: $^{29}P(T_{\frac{1}{2}} = 4.4$ sec), ^{17}F (66 sec), ^{14}O (71 sec), ^{15}O (124 sec), and ^{30}P (2.50 min). The halflife of ^{29}P (formed by a proton transfer to ^{28}Si) is very similar to that of ^{27}Si, and both would have been considered as the 4 second activity in the decay curve analysis. However, significant increases in the relative amount of this activity were noted as a function of bombarding time on a given target, indicating that $^{12}C(^{16}O, n)^{27}Si$ was probably responsible. There was no evidence for β emitters of about one minute halflife in any of the decay curves.

The other two activities, ^{15}O and ^{30}P, were quite serious since they could have given the wrong cross section for ^{30}P production. The reactions forming them would be:

$^{16}O + {}^{28}Si \rightarrow {}^{15}O + {}^{29}Si$	Q = -7.2 MeV	$E_{threshold}$ = 11.3 MeV
$\rightarrow {}^{14}N + {}^{30}P$	-8.9	14.0
$^{16}O + {}^{29}Si \rightarrow {}^{15}O + {}^{30}Si$	-5.1	7.9
$\rightarrow {}^{15}N + {}^{30}P$	-6.5	10.1
$^{16}O + {}^{30}Si \rightarrow {}^{15}O + {}^{31}Si$	-9.1	14.0

A commercial 90 μ gm/cm^2 (1000 Å) nickel foil oxidized by heating it in a pure Oxygen atmosphere was used as the target in some runs. At E_{cm} = 12 MeV the cross section for production of ^{30}P and ^{31}S agreed with the values obtained with SiO targets to within 10%. Furthermore, the Coulomb barrier for ^{16}O + Si reactions is roughly 20 MeV C.M., which corresponds to bombarding energies of about 30 MeV. The presence of an activity with a halflife similar to ^{30}P was detected at lower bombarding energies. The β end-point energy for this activity is less than that for ^{30}P, and it was tentatively identified as ^{15}O, possibly from a neutron transfer reaction to Silicon. Although charged particle reactions will be greated suppressed far below the Coulomb barrier, there are no such barriers to be penetrated for a neutron transfer reaction, so they may have measureable yields there.

A schematic of the electronics is shown in Figure 29. The sequence timer turned the beam on and off by way of a beam deflector magnet. The photomultiplier high voltage had to be turned off during bombardments, otherwise there would have been electrical breakdown from positive ion feedback in the tube due to the high count

Figure 29

Electronics for the Activation Method.

All activation data were taken with basically this system. At times, an internal (to the analyzer) time base generator was used to step the decay curve analyzer from one channel to the next. For very long bombardment and counting time runs the cycle was controlled manually and the sequence timer was not used (see the text page 119).

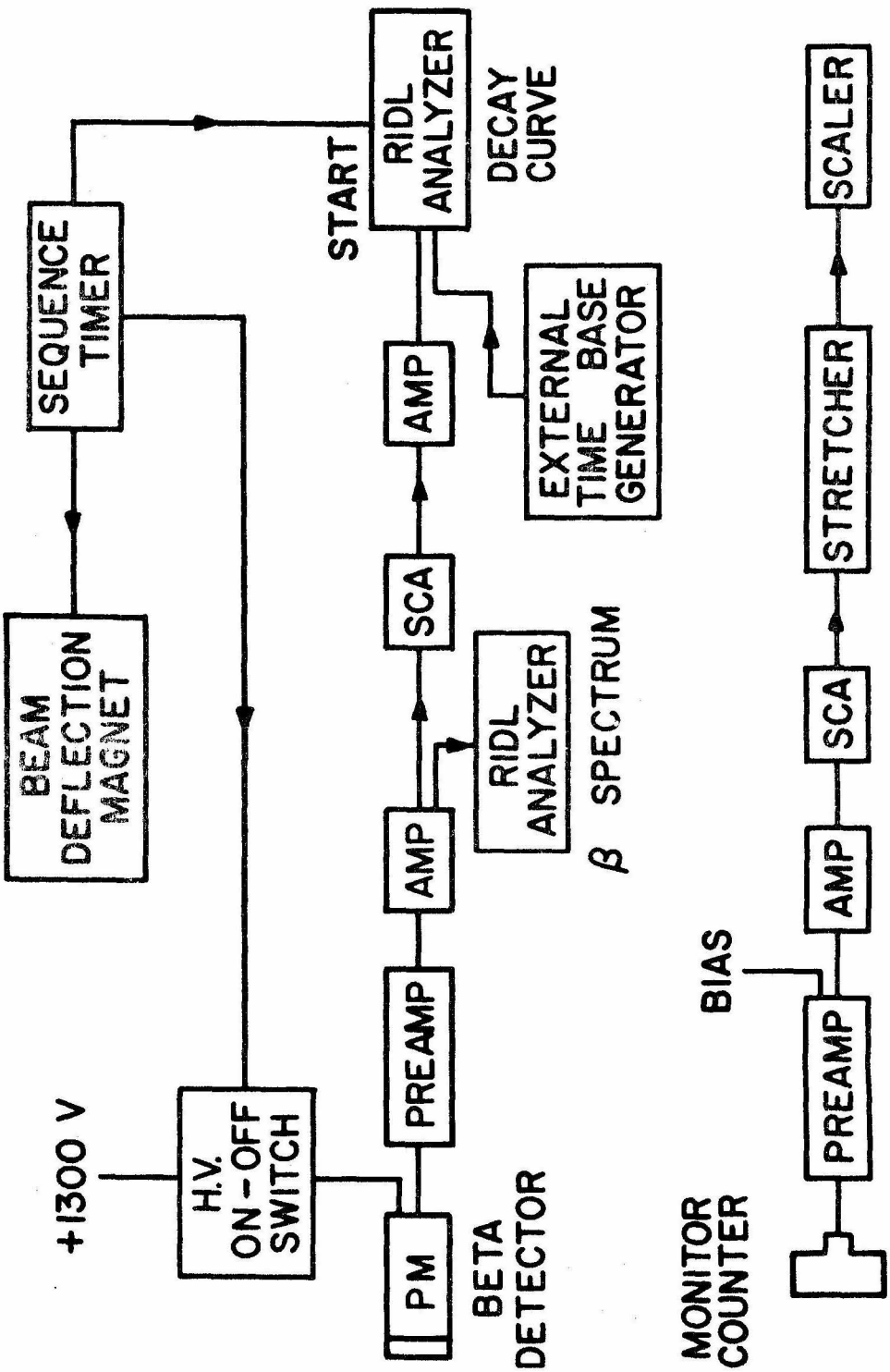
SEQUENCE TIMER
BEAM DEFLECTION MAGNET
+1300 V
H.V. ON-OFF SWITCH
PM
BETA DETECTOR
PREAMP
AMP
SCA
START
RIDL ANALYZER
DECAY CURVE
AMP
EXTERNAL TIME BASE GENERATOR
RIDL ANALYZER
β SPECTRUM
MONITOR COUNTER
BIAS
PREAMP
AMP
SCA
STRETCHER
SCALER

rates. The photomultiplier did not recover during the counting period unless it was turned off during the beam on part of the cycle. Bombardment and counting times were varied. The ^{31}S and ^{27}Si lifetimes are quite similar, and at higher energies their yield is substantially less than the ^{30}P yield. Therefore bombardment times were typically 3 seconds and counting times ranged from 20 to 55 seconds in order to improve the data on the $^{16}O(^{16}O,n)^{31}S$ cross section. Longer bombarding times (60 - 180 sec) and counting times were used at lower energies to obtain the ^{30}P cross sections.

For the time sequence spectra a lower level discriminator was set on the photomultiplier pulses to reduce room background counts. Usually the cutoff was above the 511 keV annihilation radiation Compton edge. Corrections for the true beta counts excluded were made when cross sections were computed. Discriminator pulses were fed into a RIDL 400 channel analyzer in the time sequence mode to give the decay curve. The dwell time was 0.6 sec/channel with the analyzer internal oscillator, or 0.25 to 4.0 sec/channel with an external oscillator. A typical decay curve and the corresponding background is shown in Figure 30. In addition to the time sequence spectra, beta spectra were also taken during most runs (see Figure 31).

Figure 30

Beta Decay Curve and Background.

The beta decay curve with the target in and the corresponding curve for the target taken out of the beam were taken at E_{cm} = 11.95 MeV. The curve with the background subtracted shows three activities (see the three straight lines drawn through the points). The bombarding time was 3.1 seconds, the counting time was 50.3 seconds, and the dwell time per channel was 0.25 seconds. The curves represent a total of 20 cycles each (see the text page 122).

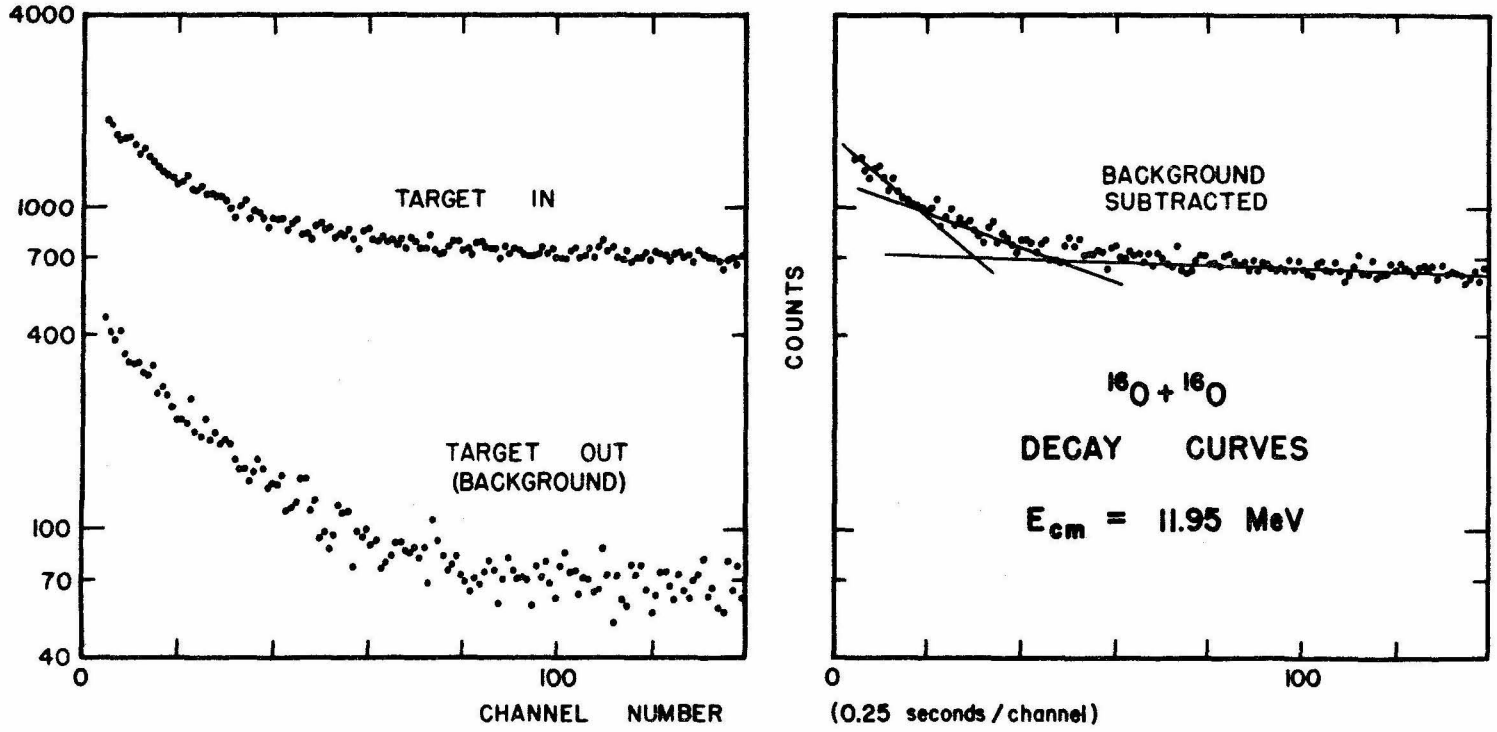
4000
1000
700
400
100
70
40
0
100
TARGET IN
TARGET OUT
(BACKGROUND)
CHANNEL NUMBER
COUNTS
BACKGROUND
SUBTRACTED
$^{16}O + ^{16}O$
DECAY CURVES
E_{cm} = 11.95 MeV
0
100
(0.25 seconds / channel)

Figure 31

Typical Beta Spectrum from $^{16}O + ^{16}O$.

The spectrum of counts from the plastic scintillator used in the activation measurements is shown for $E_{cm} = 9$ MeV. A low energy cutoff was necessary to discriminate against the gamma background (see Figure 32 and the text page 122).

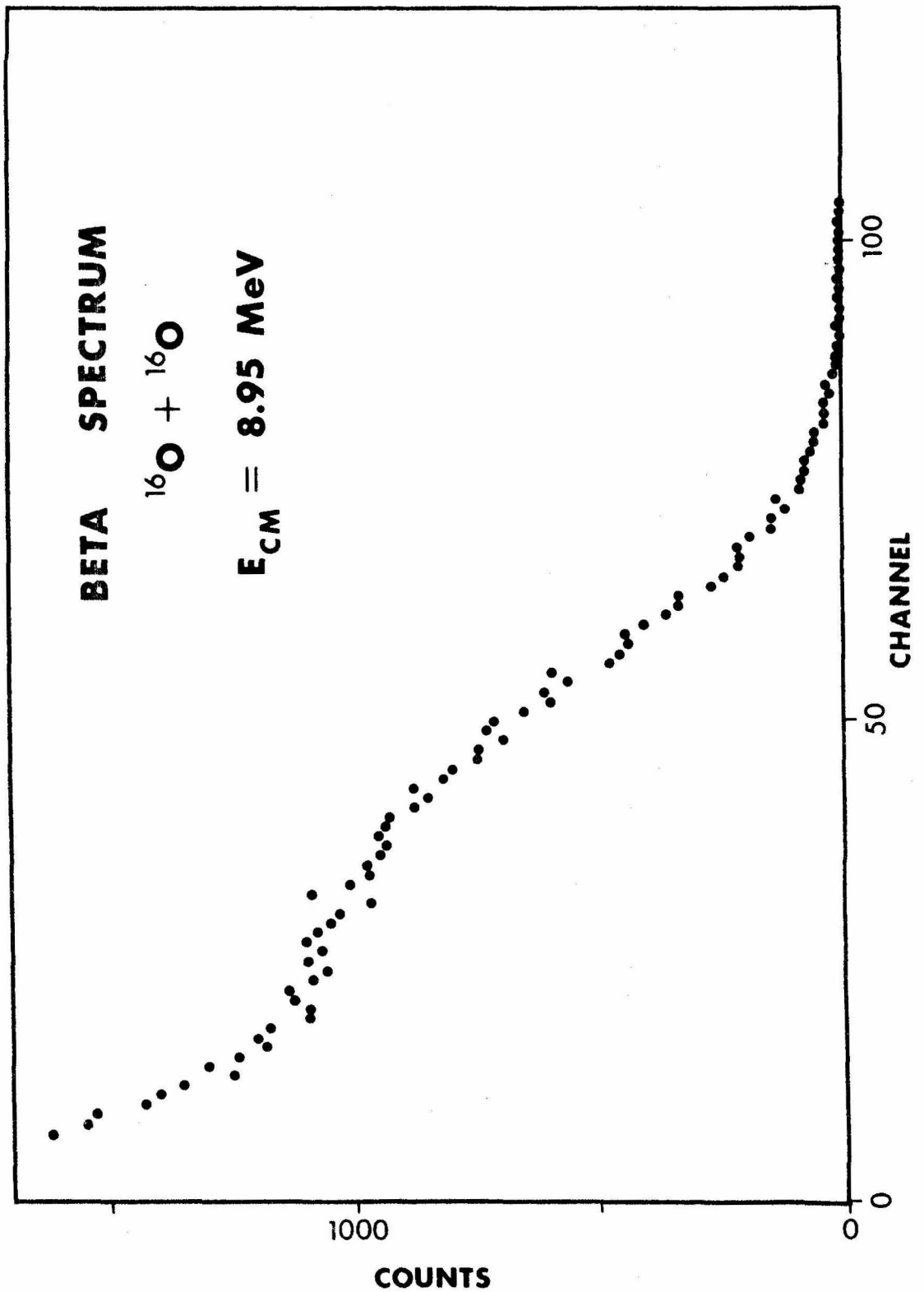
BETA SPECTRUM
$^{16}O + ^{16}O$
$E_{CM} = 8.95$ MeV
1000
0
COUNTS
0
50
100
CHANNEL

Data Analysis

A number of corrections had to be applied to derive final cross sections. The general expression used in the analysis follows:

$$\begin{pmatrix}\#\text{ radioactive}\\ \text{nuclei formed}\end{pmatrix} = \begin{pmatrix}\#\ ^{16}\text{O in}\\ \text{per sec}\end{pmatrix} \cdot \begin{pmatrix}\#\ ^{16}\text{O targets}\\ \text{per cm}^2\end{pmatrix} \cdot \begin{pmatrix}\text{Cross section}\\ \text{in cm}^2\end{pmatrix} \cdot \begin{pmatrix}\text{Time in}\\ \text{sec}\end{pmatrix}$$

$$\begin{pmatrix}\#\ ^{16}\text{O elastically}\\ \text{scattered at}\\ \theta_{cm} = 90^{o}\end{pmatrix} = \text{NMON} = \begin{pmatrix}\#\ ^{16}\text{O in}\\ \text{per sec}\end{pmatrix} \cdot \begin{pmatrix}\#\ ^{16}\text{O targets}\\ \text{per cm}^2\end{pmatrix} \cdot \begin{pmatrix}\Delta\Omega_{mon}\\ \text{in sr}\end{pmatrix} \cdot \left(\frac{d\sigma}{d\Omega}\right)_{\substack{\text{el.}\\ \text{lab}}} \text{in cm}^2/\text{sr} \cdot \begin{pmatrix}\text{Time in}\\ \text{sec}\end{pmatrix}.$$

Therefore

$$\sigma_{TOT} = \frac{\left(\frac{d\sigma}{d\Omega}\right)_{el.lab}(\theta_{cm} = 90^{o}) \cdot \left(\Delta\Omega_{mon}\right)}{\text{NMON}} \cdot \begin{pmatrix}\#\text{ radioactive}\\ \text{nuclei formed}\end{pmatrix}$$

where $\begin{pmatrix}\#\text{ radioactive}\\ \text{nuclei formed}\end{pmatrix}$ was determined from

$$\text{NCOUNTS} = \begin{pmatrix}\#\text{ radioactive}\\ \text{nuclei counted at}\\ \text{end of bombardment}\end{pmatrix} = \begin{pmatrix}\#\text{ radioactive}\\ \text{nuclei formed}\end{pmatrix} \cdot \begin{pmatrix}\text{Timing}\\ \text{Correction}\end{pmatrix} \cdot \begin{pmatrix}\text{Efficiency}\\ \text{Correction}\end{pmatrix} \cdot \begin{pmatrix}\beta\text{ Spectrum}\\ \text{Correction}\end{pmatrix}.$$

The timing correction allowed for the nuclei formed which decayed before the end of bombardment. It could also correct for deviations from complete equilibrium in the number of ^{31}S and ^{30}P on the catcher foil. However, at least two or three cycles were taken before measurements were actually made, so corrections for nonequilibrium amounted to < 10% and they were not actually applied. The expression for the timing correction was

$$\frac{\text{Total \# formed}}{\text{\# at end of bombardment}} = \frac{T_o}{\tau} \frac{(1 - e^{-T_c/\tau})}{(1 - e^{-T_o/\tau})}$$

where τ = mean life of the activity, T_o = bombardment time per cycle, and T_c = total time per cycle.

The efficiency correction allowed for the positrons emitted but not absorbed in the scintillator. Even with a very large diameter plastic scintillator, only half the positrons would have been counted (2π instead of 4π solid angles). In addition, some more β's were lost by going through the catcher foil. The total correction (including the $2\pi/4\pi$ factor) was estimated to be about $(2.3 \pm 0.2)^{-1}$ and a systematic error can be associated with it.

The β spectrum correction allowed for counts missing in the decay curve because of the discriminator setting. Its value was estimated using a good statistics beta spectrum (with background subtracted) at E_{cm} = 12 MeV with a very low discriminator setting. The energy calibration was determined from γ spectra of ^{22}Na,

ThC" and ^{207}Bi. Starting with the highest β^+ endpoint energy activity, ^{31}S, a Fermi curve was fit to the high energy tail of the spectrum and subtracted off. Curves for ^{27}Si and ^{30}P were successively subtracted in the same way. These fitted curves were used to estimate the β spectrum correction. Note that it is different for each activity because of different β endpoint energies. The summed fitted and experimental curves used are shown in Figure 32. The areas differed by 20% with too many low energy counts experimentally. The $^{12}C(^{16}O,n)^{27}Si$ reaction on a Carbon foil produced a nearly pure ^{27}Si beta spectrum. The same procedure was used on this spectrum, and the fitted and actual areas again differed by 20%. The excess low energy counts in the spectra were probably real β particles that had not been stopped in the scintillator because they were scattered out, or particles that were travelling nearly parallel to the scintillator surface and lost energy in the catcher foil before hitting the Pilot B plastic. β spectrum corrections for the data varied from 0.7 - 33% for ^{31}S and from 1.5 - 360% for ^{30}P. They could be estimated fairly well; this was demonstrated from the variety of discriminator settings giving agreement of cross sections within experimental errors (except for the low energy ^{30}P data).

The number of radioactive nuclei left at the end of bombardment, NCOUNTS, was determined from the decay curves. First background counts were subtracted from the decay curve,

$$N = (N_{Decay} - N_{Background}) \pm \sqrt{N_{Decay} + N_{Background}} .$$

Figure 32

Beta Spectrum and Fitted Curve.

The experimental points are from a good statistics $^{16}O + ^{16}O$ beta spectrum with background subtracted at $E_{cm} = 11.95$ MeV. The theoretical curve is the sum of beta spectra for ^{31}S, ^{30}P and ^{27}Si fitted to the high energy end of the observed spectrum (see the text page 129 for details of the fitting procedure), and was used to estimate the β-spectrum correction.

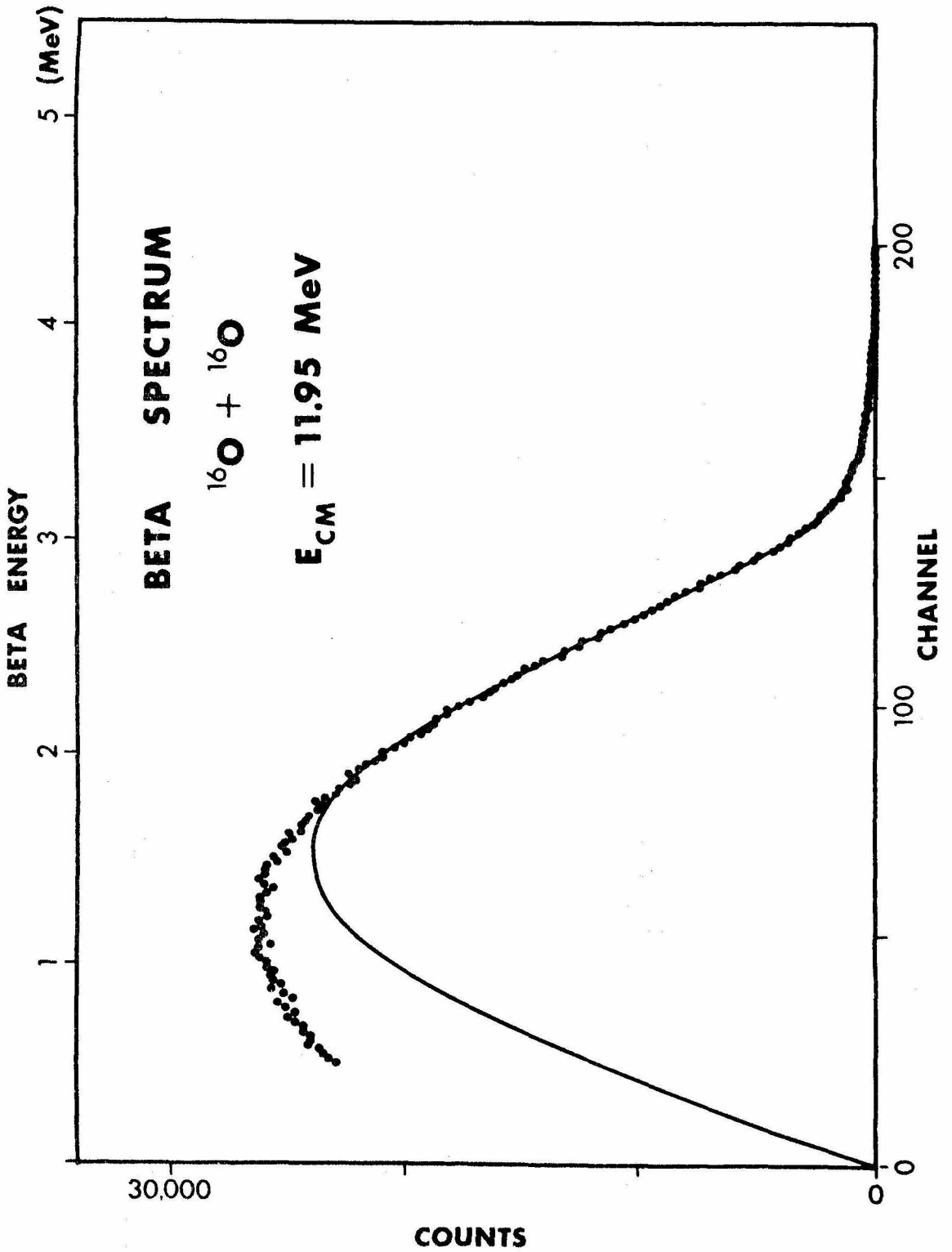
BETA SPECTRUM
$^{16}O + ^{16}O$
$E_{CM} = 11.95$ MeV
BETA ENERGY
1
2
3
4
5 (MeV)
30,000
COUNTS
0
100
200
CHANNEL

During the background measurement with the beam in but target out it was attempted to keep the beam intensity constant at all times. However, there is an error associated with the background subtraction because the beam intensity may have changed between the target-in and target-out runs. A three parameter least squares fit was made for N as a function of time, assuming three exponentially decaying components with the known halflives of ^{31}S, ^{30}P and ^{27}Si. The fit gave NCOUNTS for each activity. Two activities were not sufficient to fit the data. Since the background was subtracted, the values of NCOUNTS corresponded to reactions on the SiO target only, and not those on the catcher foil.

Results

The contaminant reaction $^{16}O + ^{12}C \rightarrow ^{31}Si + n$ was studied on a 20 μ gm/cm^2 Carbon foil to estimate the amount of Carbon necessary to account for the observed 4 second β activity. It was also used to estimate the β spectrum correction factor. The monitor counter was left at $\theta_{lab} = 45^o$ to the beam and the $^{16}O + ^{12}C$ elastic scattering was used to normalize the results (see Appendix I). Total cross sections obtained are given in Table 10 and Figure 33. These data indicate a layer of Carbon about 0.5 μ gm/cm^2 was present on the SiO target foils.

The final cross sections for production of ^{31}S and ^{30}P are given in Table 11 and Figures 34 and 35. The uncertainties in energies are estimated to be $\pm$ 50 keV C.M. from the energy

Figure 33

Cross Sections for $^{16}O + {}^{12}C \rightarrow n + {}^{27}Si$.

The cross sections and total errors from Table 10 for $^{12}C\ (^{16}O,n)\ ^{27}Si$ measured by the activation method are plotted. A smooth curve is drawn through the points. Energy losses have been taken into account, resulting in an overall uncertainty in the energies of ± 40 keV (C.M.).

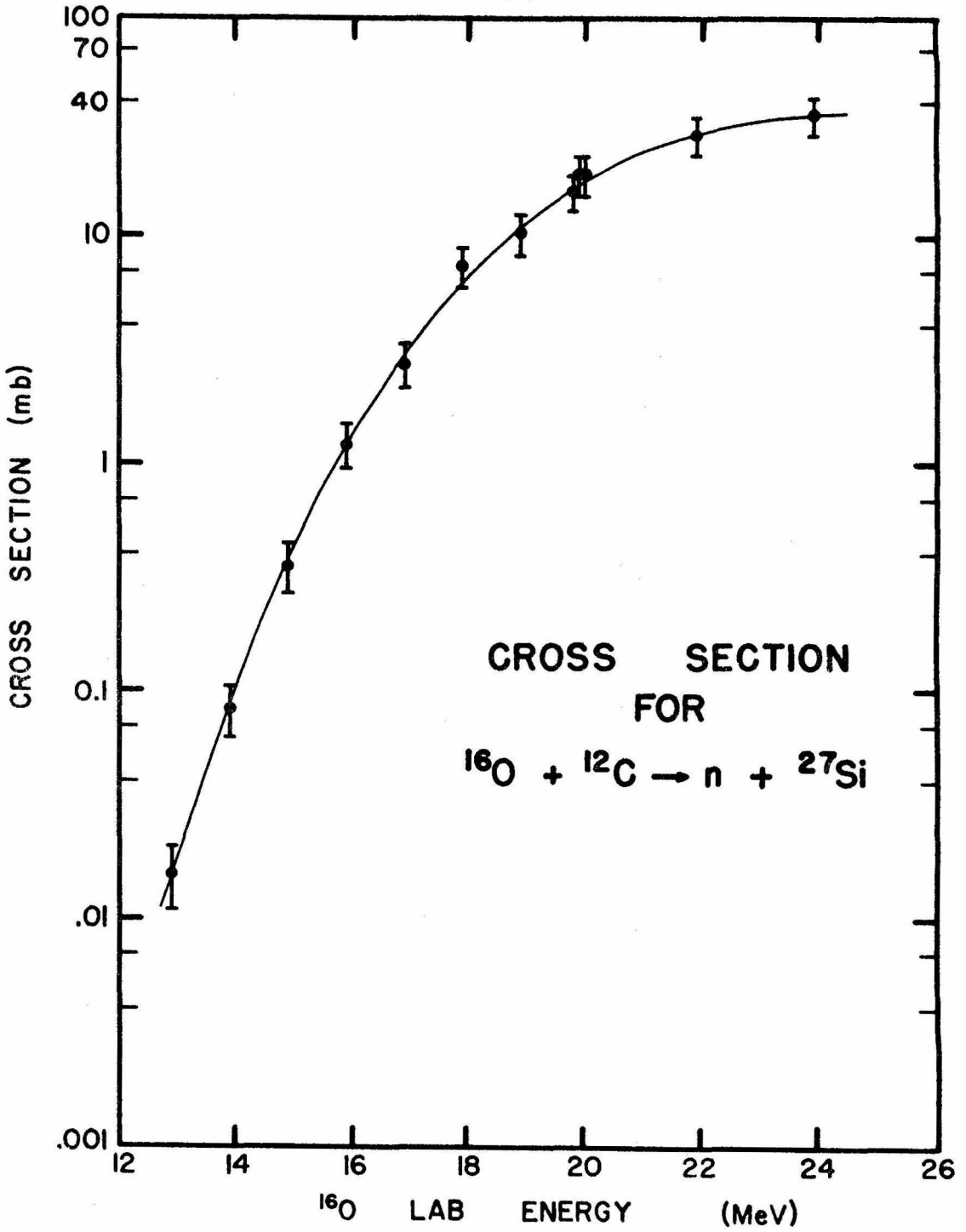
100
70
40
10
1
0.1
.01
.001
CROSS SECTION (mb)
12
14
16
18
20
22
24
26
^{16}O LAB ENERGY (MeV)
CROSS SECTION
FOR
$^{16}O + {}^{12}C \rightarrow n + {}^{27}Si$

Figure 34

Cross Sections for $^{16}O + {}^{16}O \rightarrow n + {}^{31}S$.

The cross sections obtained by the activation method for ^{16}O (^{16}O,n) ^{31}S are plotted with total errors from Table 11. A smooth curve is drawn through the points. A substantial fraction of the error results from the difficulty in separating ^{31}S and ^{27}Si in the decay curves. Energy losses have been taken into account and produce an uncertainty in the energy of each point of ± 50 keV (C.M.).

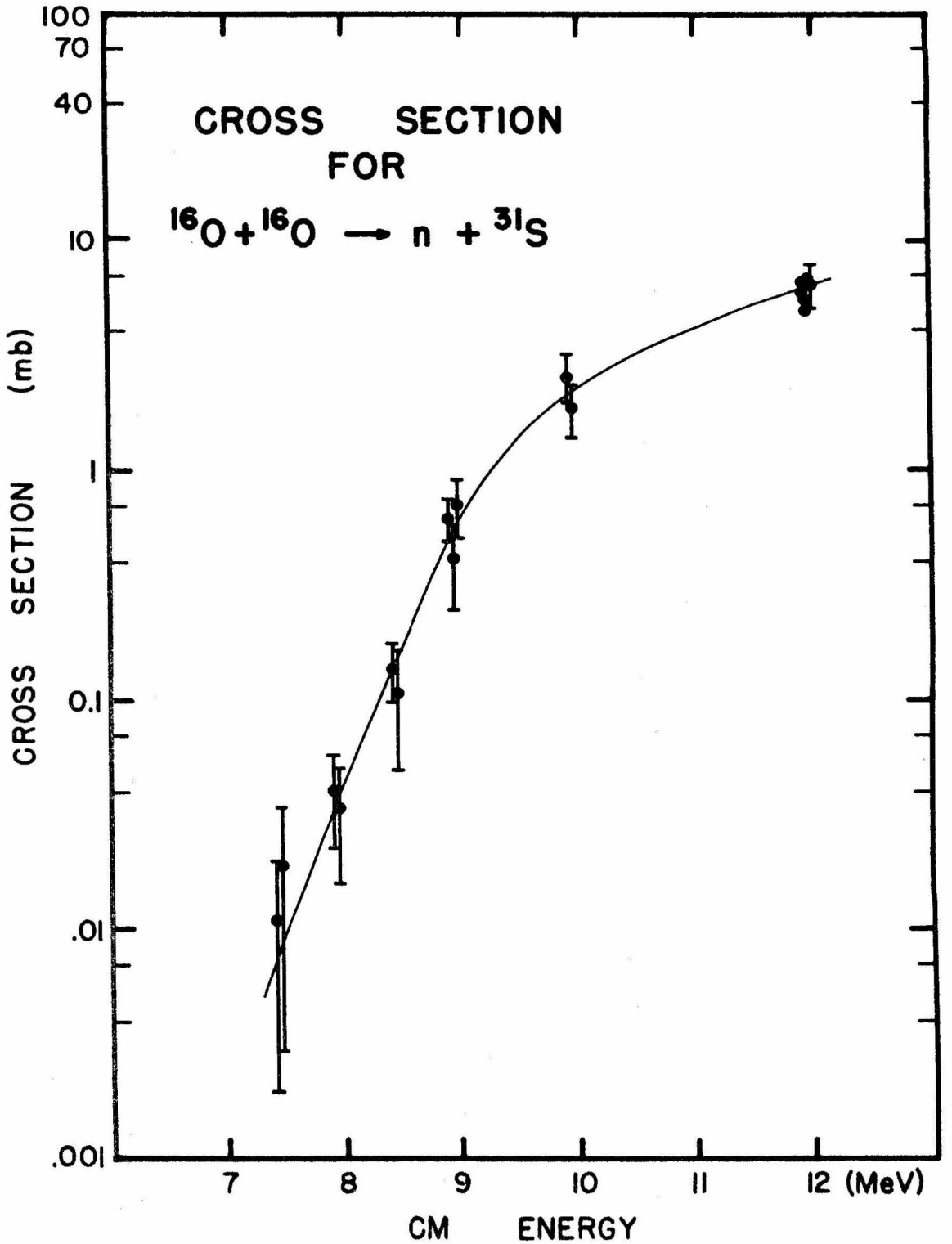
CROSS SECTION
FOR
$^{16}O + ^{16}O \rightarrow n + ^{31}S$
CROSS SECTION (mb)
100
70
40
10
1
0.1
.01
.001
7
8
9
10
11
12 (MeV)
CM ENERGY

Figure 35

Cross Sections for $^{16}O + {}^{16}O \rightarrow d + {}^{30}P$ or $p + n + {}^{30}P$.

The cross sections obtained from the activation method for the production of ^{30}P from $^{16}O + {}^{16}O$ reactions are plotted with total errors (see Table 11). The values below $E_{cm} = 8.5$ MeV are less certain because of a background activity with a halflife similar to that of ^{30}P (see the text page 119). Energy losses have been taken into account and produce an uncertainty in the energy of each point of ± 50 keV (C.M.). Also plotted are the cross sections for production of ^{31}S, neutrons and deuterons at $E_{cm} = 12$ MeV. For a discussion of these, see the Neutrons Section (page 141).

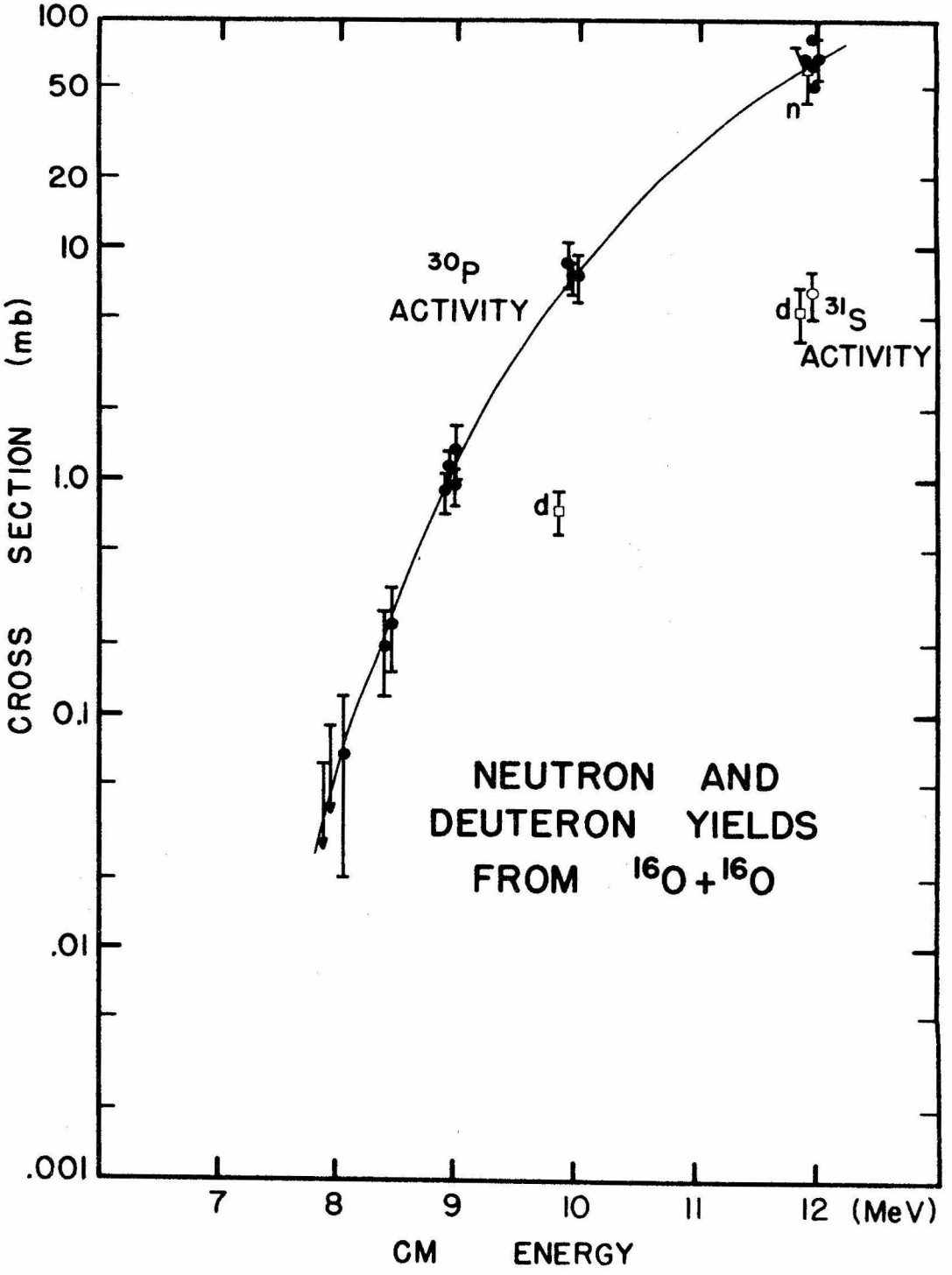
100
50
20
10
1.0
0.1
.01
.001
CROSS SECTION (mb)
7
8
9
10
11
12 (MeV)
CM ENERGY
n
30P ACTIVITY
d
31S ACTIVITY
d
NEUTRON AND
DEUTERON YIELDS
FROM 16O + 16O

losses in the target foils. Errors on all three sets of cross sections consist of:

A)	Errors on the beta spectrum corrections	± 10 - 20 %
B)	Timing correction uncertainties	± 12 %
C)	Efficiency correction errors	± 10 %
D)	Measurement errors on the monitor solid angle	± 5 %
E)	Elastic scattering cross section errors	± 2 %
F)	Statistical uncertainty on NMON	< 3 %
G)	Errors on background subtraction from an incorrect amount of beam during the background run or errors resulting from changes in beam intensity during the run causing a change in equilibrium concentrations of ^{30}P or ^{31}S (estimated)	± 5 - 20 %
H)	Least squares fit uncertainties for NCOUNTS	

At higher energies the errors are generally larger for ^{31}S than for ^{30}P because it was difficult to separate the ^{31}S and ^{27}Si in the decay curves. The yield of "^{30}P" did not change as a function of discriminator cutoff above E_{cm} = 9 MeV, so it was concluded that there was no contaminant activity with a halflife of about 2 to 3 minutes with a sizeable yield compared to the actual ^{30}P yield at these energies. The longer lived activity was studied with very high discriminator cutoffs, as well as the usual cutoffs, and with long bombardment ($T_o \simeq 3$ min) and counting times (T_c = 10 min) at E_{cm} = 8.45 and 7.95 MeV. At the former energy the cross sections for forming ^{30}P agreed at larger cutoffs, but increased with lower

cutoffs, thus indicating the presence of a contaminant activity with a 2 to 3 minute halflife but lower β endpoint energy (such as ^{15}O). At E_{cm} = 7.95 MeV only a limit on the cross section could be obtained (see Table 11). The ^{31}S cross sections did not exhibit variations with discriminator cutoff. Average values of the cross sections at each energy are also given in Table 11. Note that the ^{30}P cross section falls much faster with decreasing energy than the ^{31}S cross section.

NEUTRONS

Introduction

The cross sections for the production of ^{30}P as measured by counting β particles, and for production of deuterons as measured with the counter telescope, differ by a factor of 11 at $E_{cm} = 12$ MeV and a factor of 9 at 10 MeV. The difference is attributed to three body reactions, and as a check, a measurement of the neutron yield was performed at $E_{cm} = 12$ MeV.

Disregarding exit channels with large negative Q values on the basis of Coulomb barriers to be penetrated, the most important modes of neutron production should be

$$^{16}O + {}^{16}O \rightarrow {}^{31}S + n$$
$$\rightarrow {}^{30}P + p + n$$
$$\rightarrow {}^{27}Si + \alpha + n$$

The γ ray spectra taken indicated that other exit channels are negligible and that the ^{27}Si yield was probably smaller than the ^{31}S yield. Since a certain amount of Carbon contamination cannot be avoided when using foil targets, the reaction $^{16}O + {}^{12}C \rightarrow {}^{27}Si + n$ must also be taken into account. The activation data showed that Carbon buildup on the target was sufficiently slow to keep the neutron yield from this reaction lower than the yield from $^{31}S + n$ at $E_{cm} = 12$ MeV for many hours. In addition, a liquid Nitrogen trap

was used at the entrance to the target chamber to reduce Carbon buildup.

If the cross section determinations from either the radioactivity measurements or from the deuteron (charged particle) data were incorrect, and all ^{30}P were formed in the $^{30}P + d$ exit channel, then the number of neutrons would be at most 2 or 3 times the number of ^{31}S formed at $E_{cm} = 12$ MeV. However, if ^{30}P was produced mainly by $^{16}O(^{16}O,pn)$ the number of neutrons should be 11 to 13 times the ^{31}S yield. Even with the usual uncertainties in measuring absolute neutron cross sections, the large factor between the two alternatives made the experiment feasible. It was concluded from the results of the neutron measurements that both cross section determinations are consistent and that ^{30}P is mainly produced by three body breakups.

Experimental

A SiO foil target, similar to those employed in the activation measurements, was bombarded with a 24 MeV ^{16}O beam. The target thickness was 210 ± 60 keV (lab) (see the Activation Method Section, page 112). The low detector efficiency and difficulties in localizing the target region for taking angular distributions prevented the use of the gas target. The target chamber was 10 cm I.D. with 3.2 mm thick brass walls. As usual, the cross section was normalized to the Mott scattering at $\theta_{lab} = 45^{o}$ using a monitor counter with solid angle

$$d\Omega_{MON} = (3.6 \pm 0.3) \times 10^{-4} \text{ sr.}$$

This value was obtained from purely geometrical measurements. A correction for the finite beam spot size (< 2 mm square) to the monitor counts was estimated to be $\lesssim 10\%$.

Precautions were taken to reduce the neutron background as much as possible. In addition to shields of boron loaded paraffin and cadmium against neutrons produced upstream from the target chamber, there were no slits or collimators near the target. Instead, the beam was first focused on slits 10 m from the target. Passing through a magnetic quadrupole about 4.7 m from the target, the beam was then focused to a 1 × magnified image on a piece of quartz at the back of the chamber. The beam stop during the actual measurements was not the quartz, but a piece of tantalum with a layer of gold evaporated on it.

The choice of detectors was limited by the large γ flux. A standard long counter, similar to the shielded counter described by Hanson and McKibben (1947), was chosen because of its low γ sensitivity and fairly flat neutron response (see Figure 36). The angular distribution of the neutrons was taken at a constant distance of 26 cm from the target to the front face of the long counter's inner wax cylinder.

The neutron counter efficiency was determined with a "calibrated" (to about ± 10%) Pu-α-Be source in the place of the target.

Figure 36

"Long Counter" Response and the Predicted Neutron Spectrum.

The response of a standard "long counter" for neutron energies up to E_n = 9 MeV was taken from unpublished data in Allen (1960). An extrapolation up to E_n = 18 MeV was made using an equation fitted to this data (see page 150). The neutron spectrum calculated on the basis of a compound nucleus model is also shown (see the text page 150). Both were used to estimate a correction to the measured neutron production cross section to allow for a non-flat response for the "long counter".

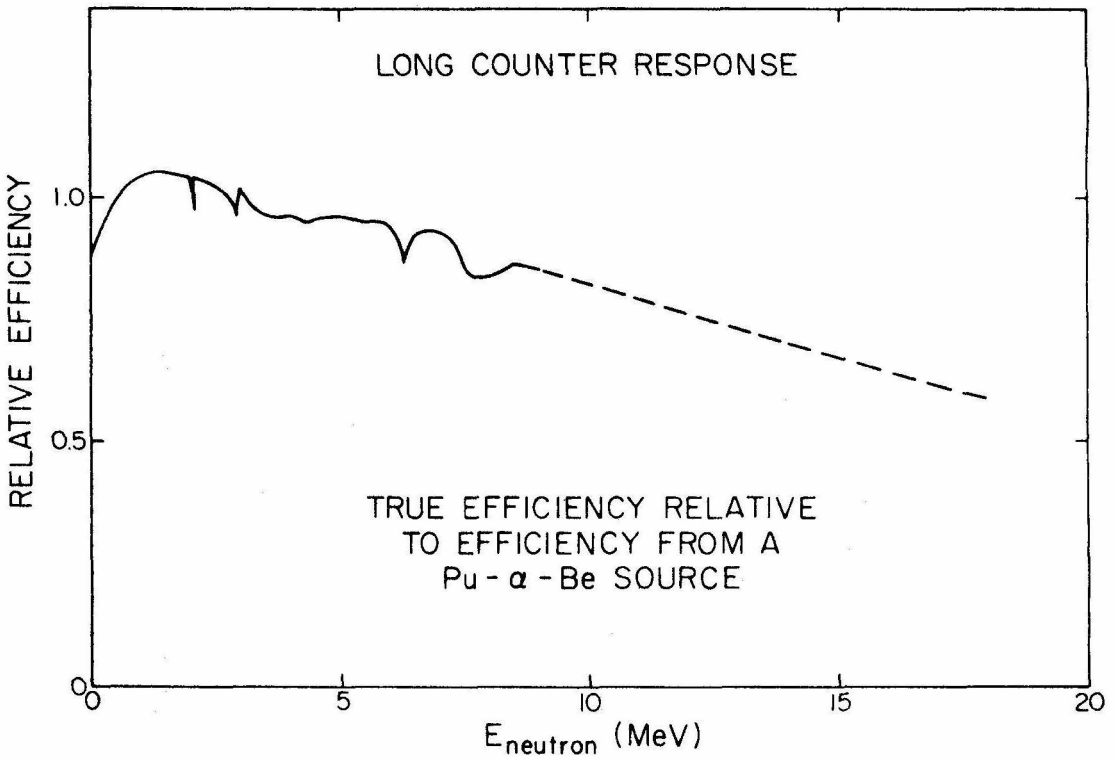
LONG COUNTER RESPONSE
RELATIVE EFFICIENCY
1.0
0.5
0
TRUE EFFICIENCY RELATIVE
TO EFFICIENCY FROM A
Pu - α - Be SOURCE
0
5
10
15
20
E neutron (MeV)

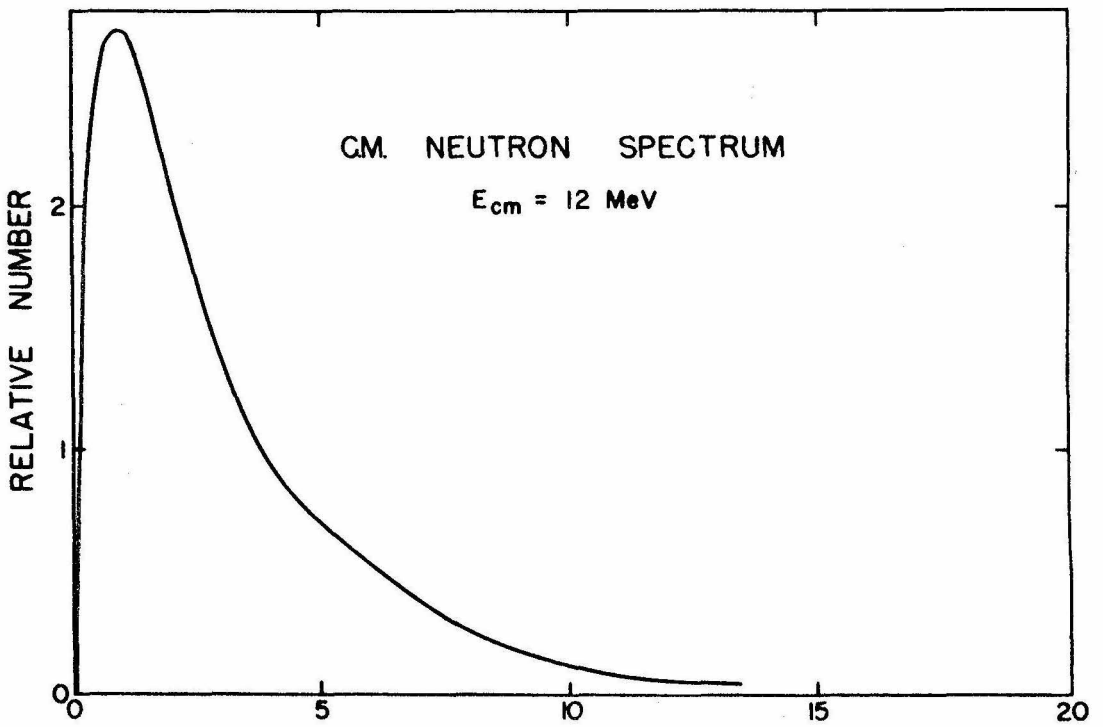
C.M. NEUTRON SPECTRUM
E cm = 12 MeV
RELATIVE NUMBER
2
1
0
0
5
10
15
20

This source was tested against a "calibrated" (again to about ± 10%) Ac-α-Be source and a 40% discrepancy in the number of neutrons detected by the long counter was found. From an average of the two sources, and the number of neutrons counted, the efficiency was

$$\text{Relative efficiency} = \text{Absolute efficiency} \cdot \frac{\text{"d}\Omega\text{"}}{4\pi} = (1.10 \pm 0.22) \times 10^{-4}.$$

The uncertainty was assigned from the source calibration. However, the detector response was not perfectly flat, and the neutron spectrum from the reaction did not duplicate that from either source, so a correction to the efficiency had to be estimated.

Following each measurement, a background run without the SiO foil was performed at each angle to allow for the nonisotropic neutron background. The beam intensity remained approximately constant throughout the experiment, and counting times ranged from 10 to 25 minutes. The low count rate relative to background prevented lower energy measurements.

Data Analysis

The data were first analyzed assuming a perfectly flat long counter response, or alternately assuming that the source spectrum and $^{16}O + {}^{16}O$ neutron spectrum were identical. The differential cross section was computed from

$$\left(\frac{d\sigma}{d\Omega}\right)_{\substack{\text{lab} \\ \text{flat resp.}}} = \left(\frac{d\sigma}{d\Omega}\right)_{\substack{\text{lab} \\ \text{el.sc.}}} \cdot \left(\frac{N}{NMON}\right) \cdot \frac{d\Omega_{MON}}{4\pi \cdot \left(\begin{array}{c}\text{Relative efficiency} \\ \text{of the long counter}\end{array}\right)}$$

The relative efficiency and monitor solid angle were directly measured, and the elastic scattering cross section was computed using the results of Figure 5 in the Elastic Scattering Section. Table 12 gives the observed values of N/NMON and their purely statistical errors. The total cross section is

$$\sigma_{\substack{n \\ \text{flat response}}} = 2\pi \int_{-1}^{1} d(\cos\theta_{lab}) \cdot \frac{d\sigma}{d\Omega}\Big)_{\substack{lab \\ \text{flat resp.}}}$$

$$= 60 \pm 17 \text{ mb.}$$

The error was computed assuming 15% uncertainty in graphical integration and extrapolation of the angular distribution to backward angles (see Figure 37).

Taking the important exit channels as $^{31}S + n$ and $^{30}P + np$ in these measurements, the following equality should hold at $E_{cm} = 11.95$ MeV:

$$\sigma(^{30}P \text{ production}) + \sigma(^{31}S \text{ production}) \stackrel{?}{=} \sigma(n \text{ production}) + \sigma(d \text{ production})$$

$$\| \qquad\qquad \| \qquad\qquad \| \qquad\qquad \|$$

$$(64 \pm 14 \text{ mb}) + (6.2 \pm 1.5 \text{ mb}) \stackrel{?}{=} (60 \pm 17 \text{ mb}) + (5.4 \pm 1.4 \text{ mb})$$

$$66 \pm 14 \text{ mb} = 65 \pm 17 \text{ mb}$$

The conclusion is that the three body breakups are responsible for most of the ^{30}P formation. Information from the activation method decay curves indicated that the left-hand side should perhaps be larger by 2 ± 1 mb if the $^{16}O + ^{12}C \rightarrow ^{27}Si + n$ reactions were included.

Figure 37

Differential Cross Section for

Neutron Production.

The laboratory differential cross sections for neutron production measured with the long counter is plotted as a function of the laboratory angle. Even with the large active volume of the long counter, it had to be moved fairly close to the target because of its low absolute efficiency and the low neutron yield. Thus, the long counter subtended a large angle. The smooth curve drawn through the points was used to determine the total cross section.

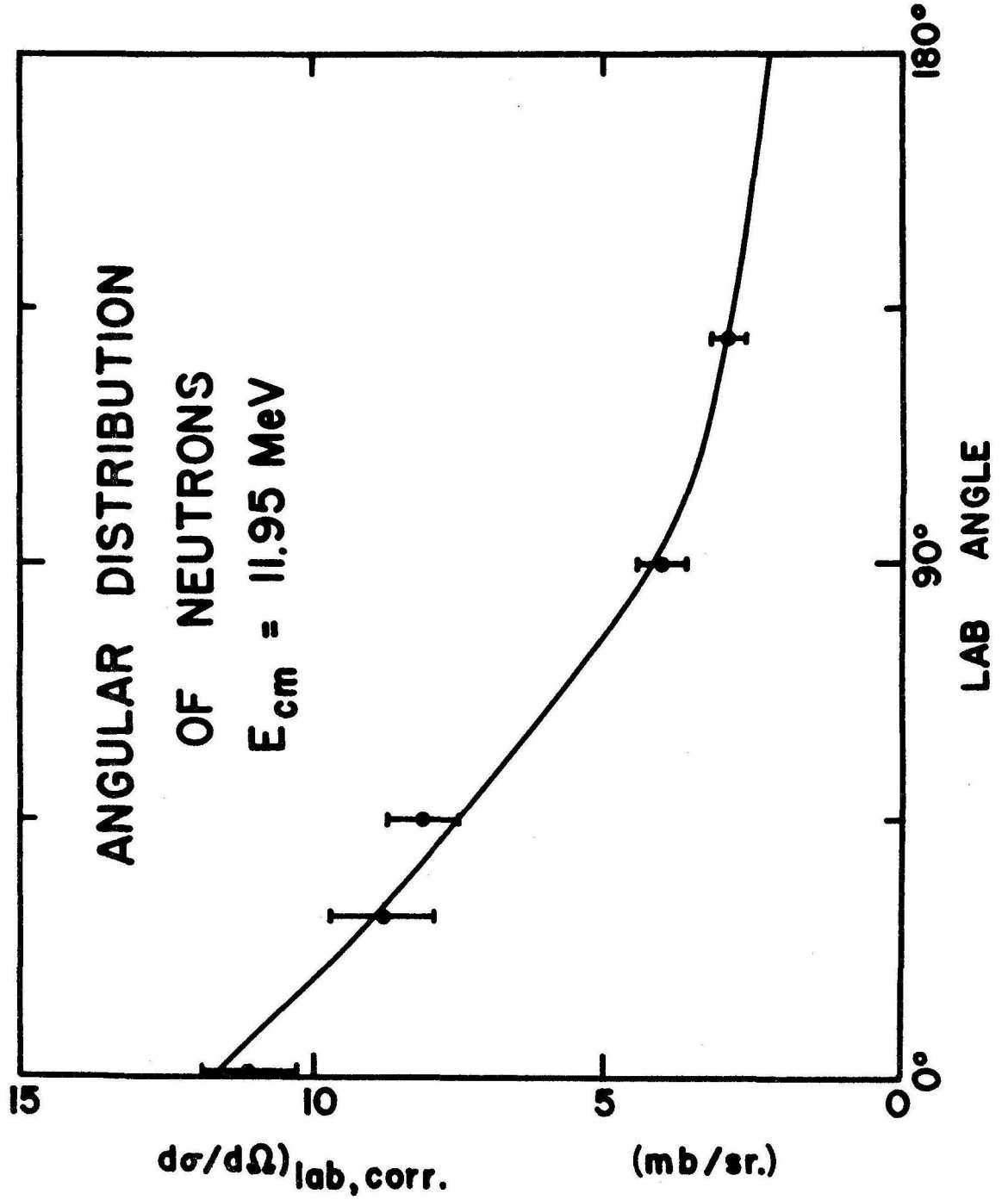
ANGULAR DISTRIBUTION
OF NEUTRONS
E_{cm} = 11.95 MeV
15
10
5
0
$d\sigma/d\Omega)_{lab,corr.}$
(mb/sr.)
0°
90°
180°
LAB ANGLE

In the previous analysis no correction was applied for the variation in detector response with neutron energy. An attempt was made to estimate the size of such a correction. First, some unpublished results given in Allen (1960) show that the long counter efficiency relative to a Pu-α-Be source

$$\text{Relative efficiency} = 0.3206 \frac{2\sigma_H}{\sigma_c + 2\sigma_H} - 0.02167\, E_n(\text{MeV}) + 0.8406$$

fitted the measured points to 1.5% RMS for E_n = 1.5 to 9 MeV. Here σ_H and σ_c are the neutron total cross sections for Hydrogen and Carbon. Below about 1 MeV the efficiency drops off again, the precise values depending critically on the long counter design. No measurements could be located for $E_n > 9$ MeV, so the above expression was used to extrapolate the response up to E_n = 18 MeV (see Figure 36).

Second, the neutron spectrum was estimated using the compound nucleus model of Blatt and Weisskopf (1952) as described in the Introduction. The density of states in all heavy nuclei of concern was taken to be that of a Fermi gas system with zero spin

$$\rho = \frac{\text{const}}{E_{exc}^2} \exp\left(2\sqrt{aE_{exc}}\right).$$

The value of a = 4 MeV^{-1} was again used. Both two and three body contributions were included and the result is also given in Figure 36. The C.M. neutron spectrum derived in this manner was transformed into the laboratory frame and then folded into the efficiency curve of

Figure 36, yielding a correction of about 4% (see Table 12). It is well within experimental uncertainties. The total cross section for neutron production is then

$$\sigma_{n\ \text{corrected}} = 62 \pm 17 \text{ mb.}$$

$^{12}C + ^{20}Ne$ PRODUCTION

Introduction

The $^{12}C + ^{20}Ne$ exit channel could not be studied by the previous techniques (detecting β particles or light particles). Information was not even available from the γ spectra, since no peaks were identified as coming from $^{12}C^*$ or $^{20}Ne^*$, and since a sizeable fraction of the yield in this channel may leave the reaction products in their ground states. Assuming this channel preceeds by a direct reaction mechanism with the α tunneling through the Coulomb barriers, Buchler (1969) estimated that the branching ratio to $^{12}C + ^{20}Ne$ was $< 20\%$ at $E_{cm} = 10$ MeV.

In order to determine the cross section for forming ^{12}C and ^{20}Ne in their ground states, the particles were detected in coincidence. Measurements were restricted at some angles by energy loss and multiple scattering in the SiO foil target and at others by high elastic scattering count rates. The angular distribution was thus obtained only for $35^\circ < \theta_{cm} < 145^\circ$. However, these data were not sufficient to determine the cross section to within 50%. An attempt was made to obtain data at more forward (or backward) C.M. angles using the 61 cm magnetic spectrometer. Elastically scattered particles and the many charge states of ^{16}O only permitted the measurement of a lower limit to the total cross section of this channel. In addition, the cross sections for the reaction leading to

excited states were not measured. Hence only a rough estimate of the $^{12}C + ^{20}Ne$ total cross section was obtained. All data were for $E_{cm} = 11.95$ MeV.

Experimental

The discrimination against other reactions provided by the kinematic coincidence technique permitted the use of a solid target. Such a technique would be difficult to perform for a gas target because of its low density and large counter solid angles. A SiO foil about 200 keV thick to a 24 MeV ^{16}O beam was used, giving a high density of localized target nuclei. The presence of a Carbon contaminant was noted, but it did not affect the measurement.

Two solid state detectors were used, one mounted on each moveable arm in the 61 cm scattering chamber. In these runs the laboratory angle was calibrated and the proper counter height was determined with a telescope zeroed in on the chamber entrance slits. In addition, the number of coincidence counts as a function of one counter angle, with the other detector fixed, showed a maximum within 0.5^{o} of the proper angle settings as determined above. Three independent sets of measurements were performed using different collimators and solid angles. The best data were obtained for one counter with small ($\Delta\theta = \pm 0.5^{o}$, $\Delta\phi = \pm 1.4^{o}$, $\Delta\Omega = 7.9 \times 10^{-4}$ sr) and the other with large ($\Delta\theta = \pm 1.8^{o}$, $\Delta\phi = \pm 3.2^{o}$, $\Delta\Omega = 6.9 \times 10^{-3}$ sr) solid angle and acceptance angles.

The beam passed through the foil into a Faraday cup. The beam intensity and target thickness were related to the integrated current in the cup by measuring the yield of Mott scattered ^{16}O nuclei at $\theta_{cm} = 90^{o}$ with the two solid state counters. The correct angle was determined as usual by maximizing the elastic scattering counts with angle, affording still another check on the angular calibration. As a result, the counter solid angle did not enter into the calculation of the differential cross section (see Data Analysis). The beam current was held approximately constant at about 200 na of 24 MeV O^{5+}, and corrections to the data for beam angle changes of $\pm 0.4^{o}$ and the finite beam spot size (< 3 mm square) were estimated to be less than 14%. Counting times ranged from 5 to 40 minutes per point.

Pulses from the two counters were amplified and fed into the Nuclear Data analyzer used in the two dimensional 64 X 64 channel mode. The signals were also sent into timing single channel analyzers and from there into an Ortec Fast Coincidence module (90 ns resolving time). Its output was stretched and delayed and then sent into the analyzer coincidence inputs. The energy scale for each counter was calibrated using elastic scattering peaks at several angles. A typical spectrum is shown in Figure 38.

Each spectrum was screened for all peaks present. Random coincidences between two elastic scattering groups were often seen and were usually separated from the desired counts. True coincidences from elastic scattering of the beam from a Carbon contami-

Figure 38

Two Dimensional Coincidence Spectrum for

$^{16}O + {}^{16}O \rightarrow {}^{12}C + {}^{20}Ne$.

A typical coincidence spectrum with the forward counter at 34° and the backward counter at 50° is shown. One contaminant group is the $^{12}C + {}^{16}O$ elastic scattering counts. A few counts from elastic scattering off other nuclei in the target are also present. At some pairs of angles, $^{16}O + {}^{16}O$ elastic scattering counts were quite strong, but they were always separated from the desired group.

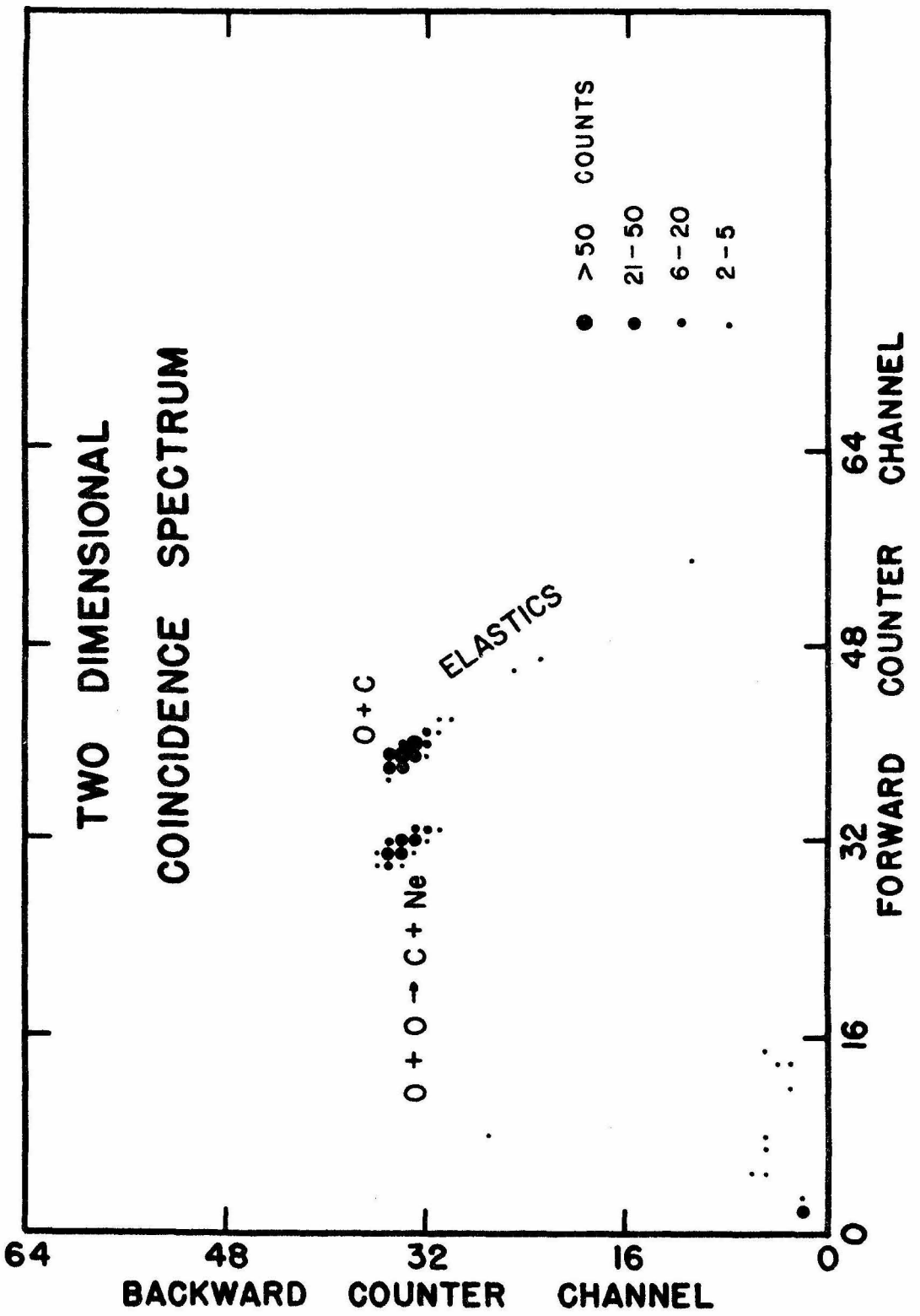
TWO DIMENSIONAL
COINCIDENCE SPECTRUM
>50 COUNTS
21-50
6-20
2-5
ELASTICS
O+C
O + O → C + Ne
64
48
32
16
0
BACKWARD COUNTER CHANNEL
FORWARD COUNTER CHANNEL

nant on the SiO foil gave a large number of counts at some angles, but these were always separated from the $^{12}C + ^{20}Ne$ group. Positions of all peaks from runs in one of the three sets of data is shown in Figure 39. The $^{12}C + ^{20}Ne$ counts were identified from the energy calibration, and random coincidences described above were excluded. The separation of the two lines in Figure 39 reflects the - 2.4 MeV Q value for $^{16}O + ^{16}O \rightarrow ^{12}C + ^{20}Ne$ as compared to $Q = 0$ for elastic scattering. This provides still another check that the peaks were properly identified.

A SiO foil target was used for the data taken with the magnetic spectrometer ($\Delta\theta = \frac{1}{2}^{o}$, $\Delta\phi = \pm 1^{o}$). The 16 counter array served as the detector. The energy scale for each of the 16 counters was calibrated with ^{16}O + SiO and ^{12}C recoils from $^{16}O + ^{12}C$ elastic scattering at $\theta_{lab} = 10^{o}$ and 21.5^{o}. Different charge states of ^{12}C and ^{20}Ne were tried, but the desired counts were always obscured by tails from ^{16}O elastic scattering lines. The best upper limit on the differential cross section was obtained by looking for 7^{+} ^{20}Ne at $\theta_{lab} = 7^{o}$ ($\theta_{cm} = 162.8^{o}$). $^{16}O + ^{16}O$ elastic scattering was detected in a monitor counter at $\theta_{cm} = 90^{o}$ and was used to integrate the beam intensity and measure the target thickness simultaneously.

Data Analysis

The differential cross section for the coincidence method was determined from the equation

Figure 39

Positions of Coincidence Peaks in $^{12}C + ^{20}Ne$ Spectra.

The channels at which peaks were observed in the coincidence spectra of one of the sets of $^{16}O + ^{16}O \rightarrow ^{12}C + ^{20}Ne$ runs is shown. Accidental coincidences between O + O and O + Si elastic scattering groups are excluded. Most of the coincident "elastic" points were from O + C or O + O elastic scattering.

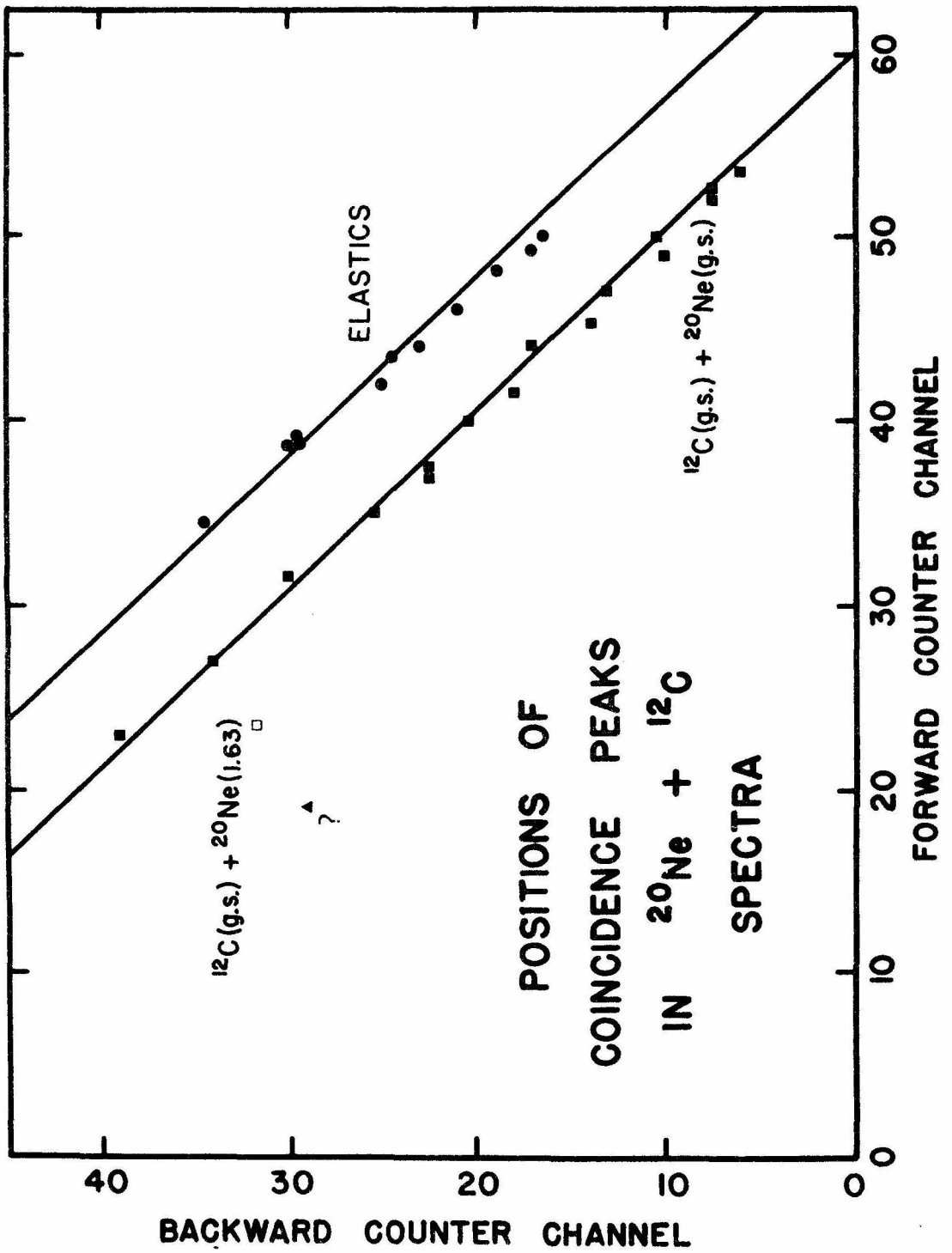
POSITIONS OF
COINCIDENCE PEAKS
IN ^{20}Ne + ^{12}C
SPECTRA
ELASTICS
^{12}C(g.s.) + ^{20}Ne(1.63)
?
^{12}C(g.s.) + ^{20}Ne(g.s.)
BACKWARD COUNTER CHANNEL
FORWARD COUNTER CHANNEL
0
10
20
30
40
50
60

$$\left(\frac{d\sigma}{d\Omega}\right)_{cm} = \left(\frac{d\sigma}{d\Omega}\right)_{\substack{cm \\ el.sc.}} \cdot \left(\frac{N}{Q}\right) \cdot \left(\frac{Q_o}{NMON}\right) \cdot \left(\frac{\text{C.M. Factor}}{\text{C.M. Factor}_{MON}}\right)$$

where $d\sigma/d\Omega)_{\substack{cm \\ el.sc.}}$ is the elastic scattering cross section at $\theta_{cm} = 90^o$ determined from Figure 9 (Elastic Scattering Section), N is the number of counts in the $^{12}C + ^{20}Ne$ peak and Q is the integrated current in the Faraday cup. The ratio $Q_o/NMON$ is the measured ratio of integrated current to monitor counts ($\theta_{cm} = 90^o$) corresponding to the counter which defined the angles θ_{cm} and ϕ of the reaction, whereas the other counter was always wide enough to catch the second particle.

A number of corrections were applied. When one counter was near $\theta_{lab} = 90^o$, the foil was turned slightly, so the coincidence counts were adjusted for the increase in target nuclei. The analyzer deadtime was always monitored and corrected for. The effect of multiple scattering of the reaction products in the foil was difficult to estimate. Under the assumption that the angular distribution after scattering in the foil is purely Gaussian

$$N(\theta) = N(0^o) \cdot e^{-\theta^2/\langle\theta^2\rangle}$$

and that the laboratory angular distribution was approximately isotropic over an area larger than the counter, the ratio

$$R = \frac{\text{\# coincidences if no multiple scattering}}{\text{\# coincidences detected}}$$

was computed for each point taken. Values of $\langle\theta^2\rangle$ were determined

from Marion and Zimmerman (1967) for each particle and angle. The corrections were < 5% for the best set of data, and were typically 1 - 15% for the other two sets. Coincidences lost by multiple scattering were somewhat compensated by particles scattered into the detectors, so R was always near 1.0. Marion and Zimmerman (1967) indicated that sizeable deviations from a Gaussian distribution occur at $|\theta| > 1.3\sqrt{\langle\theta^2\rangle}$ where single scattering events become dominant. This mainly influences the correction for the higher ^{12}C and ^{20}Ne energies, where $\sqrt{\langle\theta^2\rangle}$ is quite small (< 0.2°) in any case.

Table 13 presents the weighted average and relative errors for the differential cross sections. These errors are from statistical uncertainties in the number of counts N, and from deadtime and multiple scattering corrections (± 15 % since the number of counts in the laboratory was not isotropic nor was the scattering pure Gaussian). In addition there is an overall error of ± 15 % estimated for the finite beam spot size, for changes in the incident beam angle, and for the charge integration.

The identity of bombarding and target particles requires the angular distributions to be symmetric about $\theta_{cm} = 90^\circ$, so the data are plotted for $\theta = 0^\circ$ to 90° in Figure 40. There is a lack of points with $\theta_{cm} < 35^\circ$ for two reasons: 1) at very forward angles the elastic scattering count rates became prohibitively high, and 2) for these C.M. angles one particle has a very low laboratory energy, so energy losses and multiple scattering in the SiO foil became

Figure 40

Angular Distribution for

$^{16}O + {}^{16}O \rightarrow {}^{12}C(g.s.) + {}^{20}Ne(g.s.)$.

The final differential cross sections for the $^{16}O + {}^{16}O \rightarrow {}^{12}C(g.s.) + {}^{20}Ne(g.s.)$ reaction are plotted from Table 13. The two curves drawn through the points are the "best" fits from Table 14, and they give quite different total cross sections.

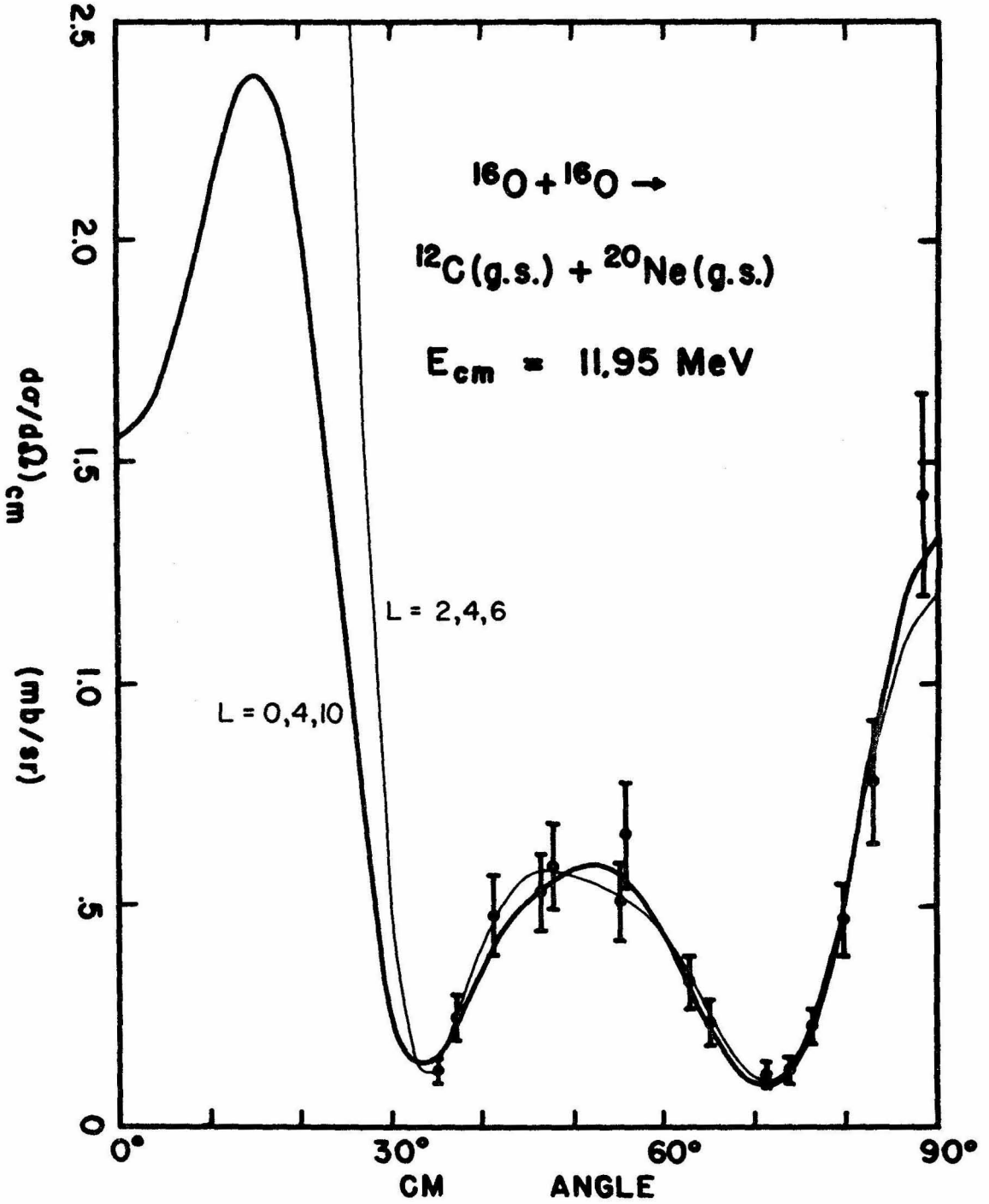
$^{16}O + ^{16}O \rightarrow$
^{12}C(g.s.) + ^{20}Ne(g.s.)
E_{cm} = 11.95 MeV
L = 2,4,6
L = 0,4,10
$(d\sigma/d\Omega)_{cm}$ (mb/sr)
2.5
2.0
1.5
1.0
.5
0
0°
30°
60°
90°
CM ANGLE

excessive. Note the presence of an isolated value for the ^{12}C (gs) + ^{20}Ne (1.63) and a single limit for the ^{12}C (gs) + $^{20}Ne^*$ (4.25) and $^{12}C^*$ (4.43) + ^{20}Ne (gs) differential cross section.

Results

An attempt was made to determine the full angular distribution from just those measured values. Since all particles involved have spin 0, and since the incoming and target particles are identical, the angular distribution must be of the form (see DeBenedetti (1964))

$$\frac{d\sigma}{d\Omega}\Big)_{cm} = \left| \sum_{\substack{L=0 \\ \text{even}}}^{\infty} A_L P_L(\cos\theta_{cm}) \right|^2 \qquad A_L \text{ complex.}$$

Classically $L \sim 6$ at $E_{cm} = 12$ MeV, so $L \leq 10$ was assumed. This still left more parameters than points. Therefore a least squares fit to the data with a function of the form

$$AP_{L_1}{}^2 + BP_{L_1}P_{L_2} + CP_{L_2}{}^2$$

or the corresponding function for three L values, was attempted. Solutions were required to have $A, C \geq 0$ and $B^2 \leq 4AC$ etc. The best fits are given in Table 14, with the two best plotted in Figure 40. The total sections were computed from

$$\sigma_{TOT} = \int 2\pi\, d(\cos\theta_{cm}) \cdot \frac{d\sigma}{d\Omega}\Big)_{cm} = \sum_{L=0}^{\infty} |A_L|^2 \frac{4\pi}{2L+1}$$

The values of χ^2 for the three parameter fits are very large, indicating that more than two L values are necessary. Two fits with six parameters seem satisfactory, but unfortunately give quite different cross sections. It appears that L = 4 is probably present, but this could be expected since the zeros of P_4 (cos θ) occur at θ = 30.6° and 70.1°, close to the minima in the angular distribution.

The spectrometer data were used to chose between the two cross sections from the fits. The cross section was derived from

$$\left(\frac{d\sigma}{d\Omega}\right)_{cm} = \left(\frac{d\sigma}{d\Omega}\right)_{\substack{cm \\ el.sc.}} \cdot \left(\frac{N}{NMON}\right) \cdot \frac{1}{Eff} \cdot \frac{\Delta\Omega_{MON}}{\Delta\Omega_{SPEC}} \cdot \frac{CMF}{CMF_{MON}} \quad .$$

The limit to the desired counts N was estimated from the spectra of the 16 counters in the array. Solid angles were determined from the known monitor counter geometry and the spectrometer opening. A correction was applied for the ratio of the particles detected by the array to the number entering the spectrometer (Eff). The upper limit to the differential cross section was 6.5 mb/sr at θ_{cm} = 162.8° (see Table 13). At this angle the L = 2,4,6 fit to the angular distribution gives $d\sigma/d\Omega)_{cm} \sim 14$ mb/sr, whereas all other fits in Table 14 give $d\sigma/d\Omega)_{cm} < 2.5$ mb/sr.

Thus, it is concluded that the cross section for $^{16}O + {}^{16}O \rightarrow {}^{12}C$ (gs) + ^{20}Ne (gs) at E_{cm} = 11.95 MeV is

$$\sigma(C + Ne) = 8 \pm 3 \text{ mb} .$$

A lower limit to this cross section is

$$\sigma(\mathrm{Ne} + \mathrm{C}) > \int_{35^{o}}^{145^{o}} 2\pi \, d(\cos \theta_{cm}) \cdot \frac{d\sigma}{d\Omega}\Big)_{cm} = 5.2 \pm 0.8 \text{ mb} .$$

The error on the fitted cross section was chosen to cover the cross sections predicted from the best fits (excluding the $L = 2,4,6$ solution). No particular significance was placed on the L values of the best fits except that $L = 4$ is probably present. Note that the cross section for the $^{12}C + ^{20}Ne$ exit channel was not obtained since reactions leaving ^{12}C and/or ^{20}Ne in excited states were not measured. The latter cross sections cannot be large since no characteristic γ's were observed from excited states in either ^{12}C or ^{20}Ne.

CONCLUSIONS

The data from each of the sections are summarized below:

A) Elastic Scattering

1) All measured $^{16}O + ^{16}O$ cross sections are normalized to the $^{16}O + ^{16}O$ elastic scattering data at $\theta_{cm} = 90^{o}$.

2) The differential cross section for $^{16}O + ^{16}O$ elastic scattering at $\theta_{cm} = 90^{o}$ is smooth except for a bump near $E_{cm} = 10.5$ MeV. There is no structure similar to that in the $^{12}C + ^{12}C$ case; thus, large variations, such as those in the $^{12}C + ^{12}C$ reaction cross section, are not expected in the $^{16}O + ^{16}O$ reaction cross sections.

B) Gamma Rays

1) The important exit channels for $^{16}O + ^{16}O$ reactions at $E_{cm} = 7$ to 12 MeV are $^{31}P + p$ and/or $^{30}Si + 2p$, $^{28}Si + \alpha$, $^{24}Mg + 2\alpha$, $^{27}Al + \alpha + p$, $^{30}P + d$ and/or $^{30}P + p + n$, $^{31}S + n$, and perhaps $^{12}C + ^{20}Ne$.

2) The gamma yield as a function of bombarding energy was much smoother for $^{16}O + ^{16}O$ than for $^{12}C + ^{12}C$, again suggesting that the large variations in the reaction cross section for $^{12}C + ^{12}C$ are not present in the $^{16}O + ^{16}O$ case. Large steps in bombarding energy were justified for $^{16}O + ^{16}O$ reaction cross section measurements.

C) Charged Particles

1) The production cross section for alphas is about 2 to 3 times less than for protons from E_{cm} = 7 to 12 MeV, and the production cross section for deuterons is more than an order of magnitude less than for protons at E_{cm} = 10 to 12 MeV. No ^{3}H or ^{3}He were definitely identified.

2) Three body events in the charged particle spectra may not have been properly analyzed, but the total production cross section was not significantly influenced and was approximately correct. This was demonstrated by evaluating some of the data by an independent method.

D) Activation Method

1) The cross section for production of ^{30}P is an order of magnitude larger than for production of ^{31}S at E_{cm} = 12 MeV, and they are about equal at E_{cm} = 8 MeV.

2) The precision of these measurements suffered from contaminants in the SiO foil target.

E) Neutrons

1) Three body breakup reactions account for over 85 % of the production of ^{30}P at E_{cm} = 10 to 12 MeV.

2) The production cross section for neutrons is about 5 to 8 times less than for protons from E_{cm} = 8 to 12 MeV, assuming the exit channel $^{30}P + p + n$ accounts for most of the formation of ^{30}P at these energies.

F) $^{12}C + ^{20}Ne$ Production

1) The cross section for $^{16}O + ^{16}O \rightarrow ^{12}C$ (gs) + ^{20}Ne (gs) was found to be 8 ± 3 mb, a factor of 40 below that for the production of protons at E_{cm} = 11.95 MeV.

The experimentally measured cross sections are given in Tables 7 and 11 and in Figures 26, 34 and 35.

To obtain the total reaction cross section at the lowest bombarding energies, estimates of the ^{32}S, ^{31}S, ^{30}P and $^{12}C + ^{20}Ne$ production cross sections are required. The following assumptions were made for this purpose:

1) $\sigma(^{30}P) = \sigma(^{31}S)$ below E_{cm} = 8 MeV. The data at higher energies indicate that the two cross sections approach each other with decreasing energy, the two being approximately equal at $E_{cm} \sim 8$ MeV (see Table 11).
2) The cross section for $^{31}S + n$ remains about 9% of the proton production cross section below E_{cm} = 7.4 MeV. This is approximately the corresponding ratio at E_{cm} = 8.85, 7.85 and 7.32 MeV.
3) The total cross section for $^{16}O + ^{16}O \rightarrow ^{12}C + ^{20}Ne$ is assumed to be 10 ± 4 mb at E_{cm} = 11.85 MeV, slightly higher than the cross section measured for ^{12}C (gs) + ^{20}Ne (gs) to allow for the formation of excited states in either ^{12}C or ^{20}Ne. The branching ratio for the $^{12}C + ^{20}Ne$ exit channel is assumed constant at the approximate value for E_{cm} = 11.85 MeV.

4) σ (^{32}S) $\simeq$ 0. It is assumed that electromagnetic decays of any ^{32}S formed (with an excitation energy of roughly 25 MeV) do not compete significantly with the strong decays (emission of one or more particles).

The first two assumptions will not seriously affect the extrapolation of the total reaction cross section to lower energies since the branching ratio for the ^{31}S + n, ^{30}P + d, and ^{30}P + p + n exit channels is small. The fourth assumption could not be checked experimentally (see the Gamma Rays Section, page 55), but is expected to be true on general principles. Furthermore, the energy dependence of the cross sections for these four exit channels will be dominated by the Coulomb barrier penetration factor for ^{16}O + ^{16}O, as is also true for the ^{31}P + n, ^{28}Si + α, ^{30}Si + 2p, etc. channels. On the other hand, the third assumption is an attempt to include the ^{12}C + ^{20}Ne exit channel without unnecessarily biasing the total reaction cross section. If a direct interaction (α-transfer) is largely responsible for the ^{12}C + ^{20}Ne yield, then the energy variation of the cross section could be different from the other exit channels.

Since the major fraction of the total reaction cross section occurs in proton and alpha emitting channels, the activation measurements were interpolated down 100 keV (C.M.) to correspond to the same C.M. energy as the charged particle data. The interpolation was performed by drawing a smooth curve through the activation data (see Figures 34 and 35). The uncertainty assigned was taken to be the same as that of a typical measurement at an energy about

100 keV (C.M.) higher.

The central problem in deriving reaction cross sections from these data is the presence of three body breakup reactions. From simple theoretical arguments (see page 14 and Figures 2 to 4), and from the experimental results of the Gamma Rays and Neutrons sections, three body exit channels are important in $^{16}O + ^{16}O$ reactions at the energies studied. Not only is the absolute percentage of three body reactions important, but the variation of this percentage with bombarding energy may significantly influence the extrapolation of the total reaction cross section to energies below those measured.

Upper and lower limits to the total reaction cross section are

$$\sigma_{LIM} = \sigma_{LIM}(p) + \sigma_{LIM}(\alpha) + \sigma(^{12}C + ^{20}Ne) +$$

$$+ (\sigma(^{30}P) + \sigma(^{31}S) = \sigma(n) + \sigma(d))$$

with $\sigma_{LIM}(p)$ and $\sigma_{LIM}(\alpha)$ the corresponding limits to the charged particle cross sections. These were discussed in the Charged Particles section (page 107). The upper limit was derived by assuming all α and p counts were from two body exit channels. The lower limit was obtained by taking as three body breakup reaction products all counts that were not definitely from two body processes. These are given in Table 9.

A better estimate of the upper limit can be obtained by subtracting off known three body reactions, namely $^{30}P + p + n$ events

or $\sigma(^{30}P)$. The Neutrons section demonstrated that over 85% of all ^{30}P formed in $^{16}O + ^{16}O$ reactions was produced by this exit channel at E_{cm} = 10 and 12 MeV. The cross section for $^{30}P + d$, $\sigma(d)$, is not entirely neglected by this procedure. In the charged particle spectra taken with the counter telescope of Figure 13, protons and deuterons could not be resolved. Any deuterons in the tail of the proton line were counted and analyzed as protons. However, an improper center-of-mass solid angle factor was therefore applied to such counts. On the other hand, the number of deuterons was very small compared to the number of protons at higher energies, and no indications of a deuteron line were observed at lower energies in the two-dimensional charged particle spectra. Arguments in the Introduction based on Coulomb barrier heights and Q values also suggest that the deuteron production cross section is small compared to the total reaction cross section at lower energies. Furthermore, the error introduced by incorrectly analyzing any deuterons did not seriously affect the production cross section for protons and deuterons. This was demonstrated by the agreement of the cross sections obtained by analyzing the data with two independent methods. Thus, it is concluded that a meaningful limit to the reaction cross section can be obtained in this way.

The final total cross section limits were computed from

$$\sigma_{\substack{\text{lower}\\ \text{lim}}} = \sigma_{\substack{\text{lower}\\ \text{lim II}}}(p) + \sigma_{\substack{\text{lower}\\ \text{lim II}}}(\alpha) + \sigma(^{30}P) + \sigma(^{31}S) + \sigma(^{12}C + ^{20}Ne)$$

$$\sigma_{\substack{\text{upper}\\ \text{lim}}} = \sigma_{\text{Production}}(p+d) + \sigma_{\text{Production}}(\alpha) + \sigma(^{31}S) + \sigma(^{12}C + ^{20}Ne)$$

and the results are given in Table 15. The final cross sections are the average of these two limits. The total cross sections for the lowest two energies were derived from the upper limit only and the assumption of 17% to 20% three body reactions. These percentages were estimated from the three body fractions at the other four energies. Errors are estimated from the uncertainties in the three body percentage, errors on the measured cross sections, and uncertainties in the extrapolated cross sections.

The values of $\tilde{S}$ for these cross sections are plotted in Figure 41 for $g = 0.84\ \text{MeV}^{-1}$ (this corresponds to an interaction radius $R = 7.24$ fm; see the Introduction, page 5). A set of different values of the parameter g were tried, but in no case was $\tilde{S}$ a constant below about $E_{cm} = 9$ MeV. The $^{16}O + ^{16}O$ gamma yield in Figure 12 uses the same value of g and exhibits an energy dependence similar to that for the total reaction cross section. On the other hand, a constant $\tilde{S}$ was not expected. The measurements were made at energies close to the Coulomb barrier and there is a large angular momentum probably involved, neither of which are properly accounted for by the simple expression

$$\sigma \simeq \frac{\tilde{S}}{E} \exp\left(-\frac{179.1}{\sqrt{E}} - gE\right) .$$

Furthermore, the variation in $\tilde{S}$ is less than a factor of 5, whereas the measured cross section changes by nearly a factor of 10^5 !

Figure 41

$^{16}O + ^{16}O$ Total Reaction Cross Sections.

The total reaction cross sections for $^{16}O + ^{16}O$ and the total errors are plotted from Table 15. The barrier penetration factor has been factored out (see the text page 173). The value of g corresponds to an interaction radius of R = 7.24 fm. Energy losses have been taken into account, resulting in an overall uncertainty in the energy scale of ± 50 keV (C.M.).

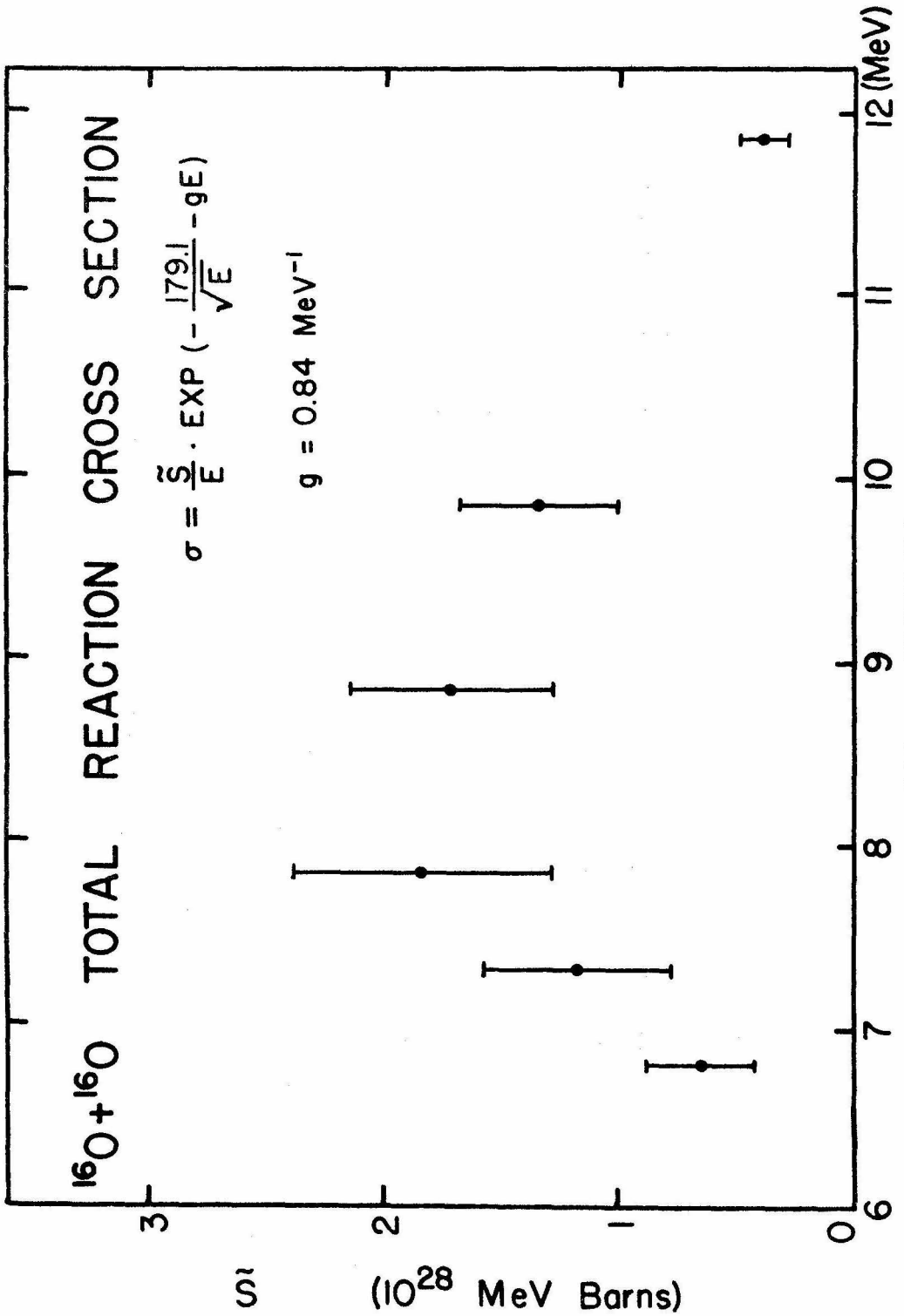
$^{16}O+^{16}O$ TOTAL REACTION CROSS SECTION
$\sigma = \frac{\tilde{S}}{E} \cdot EXP\left(-\frac{179.1}{\sqrt{E}} - gE\right)$
g = 0.84 MeV^{-1}
$\tilde{S}$ (10^{28} MeV Barns)
0
1
2
3
6
7
8
9
10
11
12 (MeV)
CM ENERGY

Attempts were also made to fit the cross sections with the expressions

$$\sigma \approx \frac{1}{E}\left[S(0)+S'(0)\cdot E+S''(0)\cdot E^2/2\right] \exp\left(-\frac{179.1}{\sqrt{E}}\right)$$

and

$$\sigma \approx \frac{\hat{S}(E)}{E} \exp\left\{-\frac{2\sqrt{2\mu}}{\hbar}\int_R^{Z_1Z_2e^2/E}\sqrt{V(r)-E}\ dr\right\} =$$

$$\frac{\hat{S}(E)}{E} \exp\left\{-\frac{179.1}{\sqrt{E}}\left[1-\frac{2}{\pi}\sin^{-1}\sqrt{\frac{E}{E_c}}-\frac{2}{\pi}\sqrt{\frac{E}{E_c}}\sqrt{1-\frac{E}{E_c}}\right]\right\}$$

(The latter is the correct WKB approximation expression for angular momentum L=0. Here $\mu = \frac{M_1 M_2}{M_1 + M_2}$, $E = E_{cm}$, R = interaction radius, $E_c = Z_1Z_2e^2/R$ and $V(r) = Z_1Z_2e^2/r$.) In no case was there an obvious method to reliably extrapolate the cross section down in energy to below E_{cm} = 6 MeV. On the other hand, the extrapolation is not so crucial since the measurements actually extend into the astrophysical region of interest. Therefore, much more detailed studies of nucleosynthesis during Oxygen burning should be permitted by the branching ratios and cross sections contained in Table 15. These are the first measurements of the total reaction cross section for $^{16}O + {}^{16}O$, the most complicated astrophysical nuclear reaction ever studied.

APPENDIX I

C + C AND C + O ELASTIC SCATTERING

The elastic scattering of $^{12}C + ^{12}C$ and $^{12}C + ^{16}O$ were measured at $\theta_{cm} = 90^{o}$ using the differentially pumped gas target and the same counters as for the $^{16}O + ^{16}O$ measurements. A mixture of high purity CH_4 and Ar gases was used at a chamber pressure of 2.5 - 3.1 torr. For the $^{12}C + ^{12}C$ scattering the energy loss to the ^{12}C beam before reaching the target was computed from the curves in Northcliffe (1963) to be 150 ± 100 keV (lab). The data are given in Table 16 and Figure 42. Most of the values in the region $E_{cm} = 3.9 - 6.4$ MeV consist of three or four different measurements. The minima in the curve correspond in energy to peaks in the total reaction cross section for $^{12}C + ^{12}C$ and in the γ yield (see Figure 12). The lack of such structure in $^{16}O + ^{16}O$ elastic scattering except for the anomaly near $E_{cm} = 10.5$ MeV suggests that the total reaction cross section for $^{16}O + ^{16}O$ is smoother than for $^{12}C + ^{12}C$. Almqvist et al. (1960, 1963) and Bromley et al. (1961) also took data on the $^{12}C + ^{12}C$ elastic scattering at $\theta_{cm} = 90^{o}$. The energies of maxima and minima agree within the uncertainties quoted above for the data of Figure 42. This is in contrast to the $^{16}O + ^{16}O$ elastic scattering (see the Elastic Scattering section, page 36).

The $^{16}O + ^{12}C$ elastic scattering was measured in steps of $E_{^{16}O} = 250$ keV (lab) at several angles. These data were mainly

Figure 42

$^{12}C + ^{12}C$ Elastic Scattering.

The ratio of the differential cross section for $^{12}C + ^{12}C$ elastic scattering at $\theta_{cm} = 90^{o}$ to the Mott scattering cross section is plotted. All errors are total errors (see Table 16 and Appendix I). Energy losses in the gas have been subtracted and produce an overall uncertainty in the energy scale of ± 50 keV (C.M.).

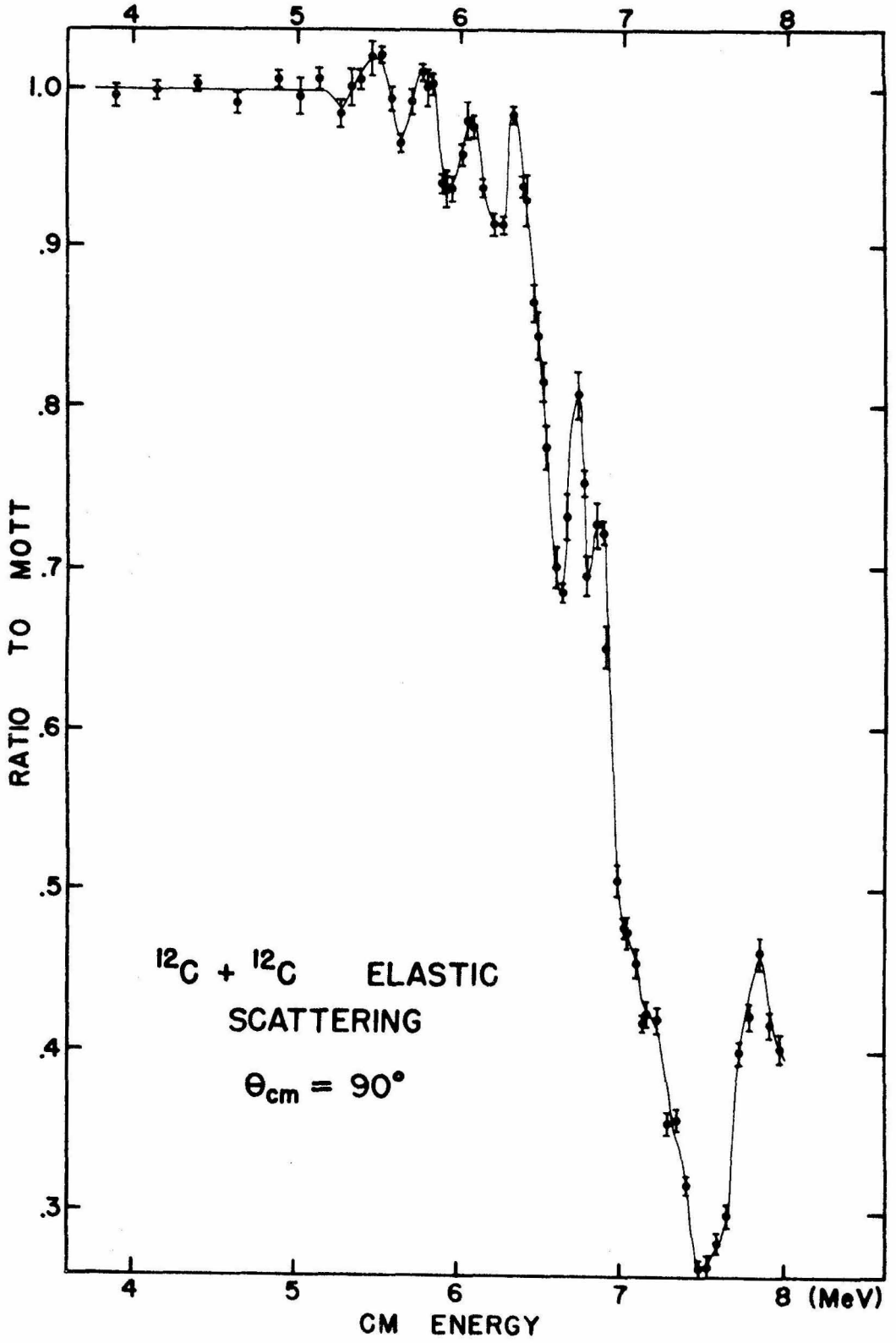
4
5
6
7
8
1.0
.9
.8
.7
.6
.5
.4
.3
RATIO TO MOTT
$^{12}C + ^{12}C$ ELASTIC
SCATTERING
$\theta_{cm} = 90°$
4
5
6
7
8 (MeV)
CM ENERGY

taken in order to normalize the $^{16}O + ^{12}C \rightarrow n + ^{27}Si$ cross section (see Activation Method, page132). The detectors were located at angles of $\theta_{lab} = 27.3^{o}$, 45.0^{o}, 55.0^{o}. The energy loss to the beam before reaching the target was estimated to be 230 ± 100 keV (lab). The results are given in Table 17.

APPENDIX II

THE $^{12}C + ^{12}C$ γ YIELD VS. E_{cm}

Using a Carbon foil 10 μ gm/cm^2 thick and Carbon beams of 0.6 μa ($^{12}C,3^+$), the $^{12}C + ^{12}C$ γ yield was measured as a function of energy in 40 - 50 keV C.M. steps from 3.7 - 7.5 MeV. The combined beam intensity and target thickness were monitored by elastic scattering at $\theta_{cm} = 90^o$, using the results of Appendix I. Only one discriminator cutoff was employed, $E_\gamma > 1.4$ MeV. The data were analyzed in the same way as in the Gamma Rays section (page 56), but the normalization was to 0.087 mb at $E_{cm} = 3.99$ MeV. This permitted a direct comparison of the $\tilde{S}$ variation with E_{cm} for the γ yield and for the charged particle measurements of Patterson, Winkler and Zaidins (1969) for the $^{12}C + ^{12}C$ reaction. The energy loss of the beam in the foil was estimated to be 60 keV (lab). The results are given in Table 18 and in Figure 12. The value of g used was taken from Patterson (1969). The agreement between the γ yield measurements and the charged particle data may have been poorer if some other discriminator cutoff had been used. For example, the strong 0.44 MeV γ line from ^{23}Na (1$\rightarrow$0) was left out by the discriminator cutoff. Significant changes in the relative intensities of lines in the γ spectrum were noted for $^{12}C + ^{12}C$ over changes in E_{cm} of roughly 100 keV as well. For a discussion of these results relative to the $^{16}O + ^{16}O$ reactions, see page 58.

BIBLIOGRAPHY

Ajzenberg-Selove, F., and Lauritsen, T., 1959, Nuc.Phys., 11, 1.

Allen, W.D., 1960, in Fast Neutron Physics part 1, edited by J.B. Marion and J.L. Fowler, (Interscience Publishers, New York), p361.

Almqvist, E., Bromley, D.A., and Kuehner, J.A., 1960, Phys.Rev.Lett., 4, 515.

Almqvist, E., Bromley, D.A., Kuehner, J.A., and Whalen, B., 1963, Phys.Rev., 130, 1140.

Arnett, W.D., 1969a, in Supernovae and Their Remnants, edited by P.J. Brancazio and A.G.W. Cameron, (Gordon and Breach, New York).

Arnett, W.D., 1969b, Astrophys. and Space Sci., 5, 180.

Blatt, J.M., and Weisskopf, V.F., 1952, Theoretical Nuclear Physics, (John Wiley and Sons, New York).

Block, B., and Malik, F.B., 1967, Phys.Rev.Lett., 19, 239.

Bohr, A., and Mottelson, B.R., 1969, Nuclear Structure volume 1, (W.A. Benjamin, New York).

Bromley, D.A., Kuehner, J.A., and Almqvist, E., 1960, Phys.Rev.Lett., 4, 365.

Bromley, D.A., Kuehner, J.A., and Almqvist, E., 1961, Phys.Rev., 123, 878.

Brueckner, K.A., Buchler, J.R., and Kelly, M.M., 1968, Phys.Rev., 173, 944.

Buchler, J.R., 1969, Ph.D. thesis, University of California at San Diego.

Cameron, A.G.W., 1959, Ap.J., 130, 895.

Carter, E.B., Stelson, P.H., Mehta, M.K., and Bernard, D.L., 1965, Nuc.Phys., 63, 575.

Chatwin, R.A., Eck, J.S., Richter, A., and Robson, D., 1969, Phys.Rev., 180, 1049.

Chatwin, R.A., Eck, J.S., Robson, D., and Richter, A., 1970, Phys.Rev.C, 1, 795.

Chiu, H.Y., 1966, in Stellar Evolution, edited by R.F. Stein and A.G.W. Cameron, (Plenum Press, New York).

Chiu, H.Y., 1968, in Nucleosynthesis, edited by W.D. Arnett, C.J. Hansen, J.W. Truran and A.G.W. Cameron, (Gordon and Breach, New York).

Curran, S.C., 1958, in Handbuch der Physik, volume 45, edited by S. Flügge and E. Creutz, (Springer - Verlag, Berlin).

Davis, R.H., 1960, Phys.Rev.Lett., 4, 521. Also, see Proceedings of the Second Conference on Reactions Between Complex Nuclei, Gatlinburg, (John Wiley and Sons, New York), p297.

DeBenedetti, S., 1964, Nuclear Interactions, (John Wiley and Sons, New York).

Dwarakanath, M.R., 1968, Ph.D. thesis, California Institute of Technology.

Endt, P.M., and van der Leun, C., 1967, Nuc.Phys., A105, 1.

Fowler, W.A. and Hoyle, F., 1964a, Ap.J.Supp number 91, 9, 201.

Fowler, W.A. and Vogl, J.L., 1964b, in Lectures in Theoretical Physics, number VI, (University of Colorado Press, Boulder), p379.

Fowler, W.A., Caughlan, G.R., and Zimmerman, B.A., 1967, Ann.Rev.Astr.and Astr., 5, 525.

Gadioli-Erba, E. and Sona, P.G., 1969, Phys.Rev.Lett., 22, 406.

Hanson, A.C. and McKibben, J.L., 1947, Phys.Rev., 72, 673.

Huang, F.C.P., Osman, C.H., and Ophel, T.R., 1969, Nuc.Instr.and Meth., 68, 141.

Imanishi, B., 1969, Nuc.Phys., A125, 33.

Kompaneets, A.S., 1961, JETP, 12, 1196.

Landau, L., 1944, J.Phys,USSR, 8, 201.

Maher, J.V., Sachs, M.W., Siemssen, R.H., Weidinger, A., and Bromley, D.A., 1969, Phys.Rev., 188, 1665.

Marion, J.B. and Zimmerman, B.A., 1967, Nuc.Instr.and Meth., 51, 93.

Marion, J.B. and Young, F.C., 1968, Nuclear Reaction Analysis - Graphs and Tables, (John Wiley and Sons, New York).

Mattauch, J.H.E., Thiele, W., and Wapstra, A.H., 1965, Nuc.Phys., 67, 1.

Michaud, G. and Vogt, E.W., 1969, Phys.Lett., 30B, 85.

Moyal, J.E., 1955, Phil.Mag., 46, 263.

Northcliffe, L.C., 1963, Ann.Rev.Nuc.Sci., 13, 67.

Paradellis, T. and Hontzias, S., 1969, Nuc.Instr.and Meth., 73, 210.

Patterson, J.R., Winkler, H., and Zaidins, C.S., 1969, Ap.J., 157, 367.

Rakavy, G., 1967a, in High Energy Physics and Nuclear Structure, edited by G. Alexander, (North Holland, Amsterdam).

Rakavy, G. and Shaviv, G., 1967b, Ap.J., 148, 803.

Rakavy, G., Shaviv, G., and Zinamon, Z., 1967c, Ap.J., 150, 131.

Rickertsen, L., Block, B., Clark, J.W., and Malik, F.B., 1969, Phys.Rev.Lett., 22, 951.

Rossi, B.B. and Staub, H.H., 1949, Ionization Chambers and Counters; Experimental Techniques, (McGraw-Hill, New York).

Siemssen, R.H., Maher, J.V., Weidinger, A., and Bromley, D.A., 1967, Phys.Rev.Lett., 19, 369.

Truran, J.W. and Arnett, W.D., 1970, Ap.J., 160, 181.

Tsuda, H., 1963, Prog.Theor.Phys., 29, 29.

Vogt, E.W. and McManus, H., 1960, Phys.Rev.Lett., 4, 518. Also, see Proceedings of the Second Conference on Reactions Between Complex Nuclei, Gatlinburg, (John Wiley and Sons, New York), p291.

Whaling, W., 1958, in Handbuch der Physik, volume 34, edited by S.Flügge and E. Creutz, (Springer - Verlag, Berlin).

Wildermuth, K. and Caravillano, R.L., 1961, Nuc.Phys., 28, 636.

Table 1

The Ratio of the Elastic Scattering to the Mott Scattering Cross Section for $^{16}O + ^{16}O$

Energy losses have been included, but there is an overall uncertainty in the c. m. energy scale of ± 50 keV (c. m.) (See the text page 36 and figure 9).

E_{cm}	Ratio to Mott	E_{cm}	Ratio to Mott
7.34 MeV	0.989 ± .006	10.35	0.961 ± .004
7.44	.982 ± .018	10.45	.958 ± .004
7.54	.995 ± .018	10.55	.966 ± .005
7.64	.996 ± .017	10.65	.966 ± .005
7.74	1.012 ± .018	10.75	.963 ± .005
7.84	.991 ± .006	10.85	.967 ± .005
7.94	1.016 ± .017	10.95	.956 ± .005
8.04	.984 ± .016	11.05	.948 ± .005
8.14	1.002 ± .015	11.15	.915 ± .005
8.24	1.006 ± .015	11.25	.908 ± .006
8.34	1.000 ± .004	11.36	.886 ± .005
8.44	1.019 ± .015	11.46	.862 ± .006
8.54	1.008 ± .014	11.56	.833 ± .006
8.59	1.002 ± .006	11.66	.774 ± .005
8.64	.974 ± .013	11.76	.735 ± .006
8.74	.977 ± .014	11.86	.704 ± .006
8.85	.995 ± .004	11.96	.663 ± .006
8.95	1.006 ± .008	12.06	.608 ± .006
9.05	.990 ± .008	12.16	.579 ± .005
9.10	.994 ± .005	12.26	.544 ± .005
9.15	1.004 ± .008	12.36	.498 ± .006
9.25	1.003 ± .007	12.61	.416 ± .005
9.35	1.003 ± .004	12.86	.363 ± .005
9.45	.998 ± .005	13.11	.318 ± .005
9.55	1.000 ± .005	13.37	.280 ± .005
9.65	1.005 ± .005	13.62	.223 ± .004
9.75	1.003 ± .004	13.87	.198 ± .004
9.85	1.003 ± .004	14.12	.149 ± .003
9.95	1.003 ± .004	14.37	.115 ± .003
10.05	.995 ± .004		
10.15	.986 ± .004		
10.25	.975 ± .004		

Table 2

Relative Number of Counts in Gamma Spectrum Peaks (all numbers are normalized to 1000 at E_γ = 2.23 MeV). E_{cm} = 12 MeV and all ratios are ± 20 %. See figures 10 and 11.

E_γ	Relative Counter Efficiency	Nucleus	O_2 gas	NiO	Quartz	SiO[a]
0.511	5.86	Annihilation	7700	1000	10000	2300
.71	3.94	^{30}P	870	920	550	530
.85	3.18	^{27}Al	270	170	220	400
1.01	2.55	^{27}Al	480	400	220	420
1.27	1.96	$^{31}P, ^{30}Si, ..$	920	630	650	840
1.37	1.79	^{24}Mg	350	350	240	660
1.46	1.66	^{30}P	320	340	260	280
1.78	1.31	^{28}Si	670	390	500	710
2.23	1.00	$^{31}P, ^{30}Si, ..$	1000	1000	1000	1000
Total counts in 2.23 MeV peak			20700	13400	13100	3800

a) A 20 μgm/cm^2 SiO foil was also used under the same conditions as the other solid targets (see page 50 of the text). Its spectrum is not shown.

Table 3

Identification of γ Lines in the ^{16}O + Quartz Spectrum.

The γ energies are from Figure 11 and the energy calibration is good to ± 5 KeV. Transition energies are from Endt and van der Leun (1967). See the text page 50 .

E_γ	Identification	Other Transitions
0.511 ± .005 MeV	Annihilation Radiation = .511	
.680	^{30}P (1 → 0) = .678 ± .001	
.696	?	
.711	^{30}P (2 → 0) = .709 ± .001	
.757	(1.779 - 1.022 = .757)	
.849	^{27}Al (1 → 0) = .8429 ± .003	
1.020	^{27}Al (2 → 0) = 1.0130 ± .0003	
1.135	?	
1.213	(2.235 - 1.022 = 1.213)	
1.248	^{31}S (1 → 0) = 1.242 ± .020	
1.265	^{31}P (1 → 0) = 1.2661 ± .0002	^{30}P (4 → 2) = 1.267 ± .002
	^{30}Si (2 → 1) = 1.275 ± .009	^{29}Si (1 → 0) = 1.2730 ± .0005
	(1.779 - .511 = 1.268)	

Table 3 con't.

E_γ	Identification	Other Transitions
1.372	^{24}Mg (1 → 0) = 1.36857 ± .00004	
	^{29}P (1 → 0) = 1.381 ± .005	
1.457	^{30}P (3 → 0) = 1.455 ± .002	
1.533	?	^{32}S (2 → 1) = 1.543 ± .009
		^{30}Si (3 → 1) = 1.535 ± .009
1.727	(2.235 - .511 = 1.724)	^{29}P (4 → 1) = 1.721 ± .007
		^{27}Al (4 → 2) = 1.7190 ± .0009
1.783	^{28}Si (1 → 0) = 1.7787 ± .0002	
1.976	^{30}P (4 → 0) = 1.976 ± .002	
2.03	^{31}P (4 → 1) = 2.0288 ± .0005	^{31}S (4 → 1) = 2.045 ± .025
	(3.05 - 1.02 = 2.03)	^{29}Si (2 → 0) = 2.0317 ± .0010
2.15	^{31}P (5 → 1) = 2.1481 ± .0006	^{27}Si (3 → 0) = 2.165 ± .009
2.20	^{27}Al (3 → 0) = 2.2089 ± .0006	
2.235	^{31}P (2 → 0) = 2.2338 ± .0005	^{31}P (6 → 1) = 2.239 ± .010
	^{30}Si (1 → 0) = 2.232 ± .006	
	^{31}S (2 → 0) = 2.232 ± .015	
	^{32}S (1 → 0) = 2.237 ± .004	

Table 3 con't.

E_γ	Identification	Other Transitions
2.49	(3.505 - 1.022 = 2.493)	
2.535	?	^{30}P (5 → 0) = 2.539 ± .002
2.56	?	(3.05 - .51 = 2.54)
2.845	^{28}Si (2 → 1) = 2.835 ± .006	
3.005	(3.505 - .511 = 2.996)	
3.05	?	
3.505	^{30}Si (2 → 0) = 3.507 ± .006 ^{31}P (6 → 0) = 3.5055 ± .0010	

Table 4

Estimated Branching Ratios for the Production of Heavy Nuclei. All results are normalized to the ^{28}Si yield = 1.00 (see the text page 55).

γ Decaying Nucleus	Relative Strengths		
E_{lab} =	24	20	18 MeV
^{28}Si	1.00	1.00	1.00
^{24}Mg	$\lesssim$.4	$\lesssim$.1	$\lesssim$.2
^{27}Al	$\lesssim$.5	$\lesssim$.3	$\lesssim$.2
^{30}P	1.0	.5	.2
^{27}Si	<.05		
^{29}P	$\lesssim$.03		
^{31}S	.06	.1	.1
$^{31}P + ^{30}Si$	3.5	2.9	1.7
$^{12}C, ^{20}Ne, ^{26}Mg, ^{29}Si, ^{32}S$	No Conclusions		

Table 5

$^{16}O + {}^{16}O$ γ Yield as a Function of Energy.

The yields and relative errors of γ's with energy above the indicated cutoffs are normalized to 100.0 at E_{cm} = 10.0 MeV. The energies are corrected for losses in the gas and there is a ± 50 KeV (c.m.) uncertainty associated with this correction. See the text page 57.

E_{cm}	Normalized Gamma Yields $E_\gamma > 0.6$ MeV	$E_\gamma > 1.6$ MeV	$E_\gamma > 2.2$ MeV
7.01		.037 ± 5%	
.06		.048 ± 5%	
.11		.062 ± 5%	
.16	.057 ± 5%	.074 ± 4%	.080 ± 5%
.21	.073 ± 5%	.097 ± 4%	.106 ± 5%
.26	.094 ± 5%	.125 ± 4%	.126 ± 5%
.31	.122 ± 5%	.157 ± 4%	.159 ± 5%
.36	.154 ± 5%	.181 ± 4%	.204 ± 5%
.41	.179 ± 5%	.224 ± 4%	.240 ± 5%
.46	.212 ± 5%	.264 ± 4%	.284 ± 5%
7.51	.269 ± 5%	.336 ± 4%	.321 ± 5%
.56	.345 ± 5%	.404 ± 4%	.414 ± 5%
.61	.41 ± 5%	.484 ± 3%	.445 ± 5%
.66	.51 ± 5%	.60 ± 4%	.60 ± 5%
.71	.60 ± 5%	.71 ± 4%	.70 ± 5%
.76	.68 ± 5%	.83 ± 4%	.82 ± 5%
.81	.85 ± 4%	.97 ± 4%	1.04 ± 4%
.86	.99 ± 5%	1.16 ± 3%	1.17 ± 5%
.91	1.19 ± 5%	1.36 ± 4%	1.48 ± 5%
.96	1.35 ± 5%	1.62 ± 4%	1.71 ± 5%
8.01	1.72 ± 5%	1.91 ± 4%	2.11 ± 5%
.06	1.94 ± 5%	2.13 ± 4%	2.28 ± 5%
.11	2.15 ± 5%	2.40 ± 3%	2.54 ± 5%
.16	2.49 ± 5%	2.67 ± 4%	3.03 ± 5%
.21	2.85 ± 5%	3.06 ± 4%	3.38 ± 5%
.26	3.15 ± 5%	3.33 ± 3%	3.58 ± 5%
.31	3.47 ± 3%	3.83 ± 3%	4.07 ± 3%
.36	3.90 ± 4%	4.34 ± 3%	4.66 ± 4%
.41	4.50 ± 4%	5.0 ± 3%	5.2 ± 4%
.46	4.97 ± 4%	6.0 ± 3%	5.8 ± 4%

Table 5 con't.

Normalized Gamma Yields

E_{cm}	$E_\gamma > 0.6$ MeV	$E_\gamma > 1.6$ MeV	$E_\gamma > 2.2$ MeV
8.51	5.8 ± 4%	6.7 ± 3%	6.8 ± 4%
.56	7.1 ± 4%	7.6 ± 4%	8.3 ± 4%
.61	7.8 ± 4%	8.4 ± 4%	9.3 ± 4%
.66	8.1 ± 4%	9.4 ± 4%	9.4 ± 4%
.71	9.0 ± 4%	10.4 ± 4%	10.7 ± 4%
.76	9.8 ± 4%	12.2 ± 4%	11.4 ± 4%
.81	12.2 ± 3%	13.8 ± 4%	13.8 ± 3%
.86	14.8 ± 4%	15.7 ± 4%	16.9 ± 4%
.91	17.0 ± 4%	17.7 ± 4%	19.3 ± 4%
.96	18.5 ± 4%	19.5 ± 4%	21.0 ± 4%
9.02	16.7 ± 4%	21.0 ± 4%	22.2 ± 4%
.07	21.8 ± 4%	23.6 ± 4%	24.2 ± 4%
.12	23.9 ± 4%	24.9 ± 4%	26.5 ± 4%
.17	27.1 ± 4%	27.4 ± 4%	29.9 ± 4%
.22	29.2 ± 4%	30.1 ± 4%	31.8 ± 4%
.27	32.7 ± 4%	33.4 ± 4%	35.0 ± 4%
.32	35.3 ± 3%	35.5 ± 4%	37.7 ± 3%
.37	38.7 ± 4%	39.0 ± 4%	41.0 ± 4%
.42	44.4 ± 4%	42.5 ± 4%	47.3 ± 4%
.47	45.8 ± 4%	45.7 ± 4%	48.8 ± 4%
9.52	49 ± 4%	49 ± 4%	52 ± 4%
.57	56 ± 4%	52 ± 4%	59 ± 4%
.62	56 ± 4%	58 ± 4%	58 ± 4%
.67	60 ± 4%	61 ± 5%	63 ± 4%
.72	68 ± 4%	66 ± 5%	70 ± 4%
.77	74 ± 4%	71 ± 5%	77 ± 4%
.82	83 ± 4%	80 ± 5%	86 ± 4%
.82	80 ± 4%		84 ± 4%
.82	80 ± 4%		83 ± 4%
.82	81 ± 3%		84 ± 3%
.82	79 ± 4%		81 ± 4%
.87	84 ± 4%	86 ± 5%	85 ± 4%
.92	94 ± 4%	93 ± 5%	96 ± 4%
.97	99 ± 4%	96 ± 5%	100 ± 4%

Table 5 con't.

E_{cm}	Normalized Gamma Yields $E_\gamma > 0.6$ MeV	$E_\gamma > 1.6$ MeV	$E_\gamma > 2.2$ MeV
10.02	100.0 ± 4%	100.0 ± 5% (normalization point)	100.0 ± 4%
.07	115 ± 4%	107 ± 5%	116 ± 4%
.07		120 ± 5%	
.12	121 ± 4%	126 ± 5%	120 ± 4%
.17	127 ± 4%	113 ± 5%	126 ± 4%
.22	136 ± 4%	121 ± 5%	134 ± 4%
.27	143 ± 4%	134 ± 5%	141 ± 4%
.32	150 ± 4%	140 ± 5%	148 ± 4%
.37	152 ± 4%	147 ± 5%	150 ± 4%
.42	166 ± 4%	158 ± 5%	164 ± 4%
.47	174 ± 4%	158 ± 5%	171 ± 4%
10.52	194 ± 4%	178 ± 5%	189 ± 4%
.57	194 ± 4%	209 ± 5%	190 ± 4%
.62	206 ± 4%	203 ± 5%	201 ± 4%
.67	226 ± 4%	206 ± 5%	220 ± 4%
.72	230 ± 4%	204 ± 5%	221 ± 4%
.77	250 ± 4%	239 ± 5%	240 ± 4%
.82	258 ± 3%	254 ± 5%	244 ± 3%
.87	280 ± 4%	265 ± 5%	263 ± 4%
.92	293 ± 4%	280 ± 5%	277 ± 4%
.97	300 ± 4%	302 ± 5%	283 ± 4%
11.02	308 ± 4%	302 ± 5%	289 ± 4%
.07	338 ± 4%	319 ± 5%	318 ± 4%
.12	356 ± 4%	329 ± 5%	331 ± 4%
.17	374 ± 4%	346 ± 5%	347 ± 4%
.22	388 ± 4%	342 ± 5%	359 ± 4%
.27	398 ± 4%	353 ± 5%	362 ± 4%
.33	396 ± 4%	375 ± 5%	359 ± 4%
.38	424 ± 4%	409 ± 5%	381 ± 4%
.43	468 ± 4%	413 ± 5%	387 ± 4%
.48	461 ± 4%	409 ± 5%	404 ± 4%
11.53	507 ± 4%	442 ± 5%	443 ± 4%
.58	496 ± 4%	442 ± 5%	429 ± 4%
.63	491 ± 4%	457 ± 5%	426 ± 4%
.68	508 ± 4%		437 ± 4%
.73	540 ± 4%		462 ± 4%
.78	538 ± 4%		460 ± 4%
.83	525 ± 4%		448 ± 4%

Table 6

C.M. Differential Cross Sections for Charged Particle Production.

The coefficient A of $P_0(\cos\theta)$ in a least squares fit to the angular distribution with Legendre polynomials of even order is also given for each interval in excitation energy. The errors given are relative errors only (see page 97 of the text).

$\theta_{c.m.,p}$	$\frac{d\sigma}{d\Omega})_{c.m.,p}$	$\theta_{c.m.,\alpha}$	$\frac{d\sigma}{d\Omega})_{c.m.,\alpha}$
	$E_{c.m.}$ = 11.85 MeV	E_{exc} = 0 - 5 MeV	
		25.9°	0.240 ± .032 mb/sr
		38.7	0.103 ± .016
		51.0	0.112 ± .018
		63.5	0.053 ± .011
67.9°	0.130 ± .038 mb/sr	75.0	0.036 ± .009
78.5	0.102 ± .023	86.4	0.100 ± .017
88.8	0.140 ± .026	97.2	0.078 ± .014
98.8	0.126 ± .025	107.6	0.063 ± .012
108.6	0.099 ± .019	117.2	0.081 ± .015
118.2	0.110 ± .023	126.1	0.103 ± .021
127.6	0.131 ± .027	134.9	0.076 ± .016
136.7	0.145 ± .045	143.3	0.104 ± .034
145.6	0.180 ± .038	151.0	0.205 ± .051
154.4	0.204 ± .046	158.6	0.174 ± .040
A =	0.140 ± .012	A =	0.087 ± .007
	$E_{c.m.}$ = 11.85 MeV	E_{exc} = 5 - 7.5 MeV	
23.4°	0.57 ± .10 mb/sr	26.6°	0.34 ± .05 mb/sr
34.9	0.54 ± .09	39.7	0.27 ± .04
46.3	0.46 ± .07	52.6	0.27 ± .04
57.6	0.41 ± .08	64.9	0.29 ± .06
68.7	0.33 ± .06	77.0	0.21 ± .03
79.3	0.36 ± .07	88.3	0.18 ± .04
89.8	0.39 ± .07	99.5	0.26 ± .05
100.0	0.36 ± .07	109.6	0.25 ± .06
109.8	0.34 ± .06	119.3	0.24 ± .07
119.4	0.37 ± .08	128.5	0.30 ± .06
128.5	0.35 ± .06	137.0	0.31 ± .05
137.6	0.41 ± .10	144.9	0.29 ± .09
146.4	0.41 ± .08	152.5	0.25 ± .07
154.9	0.43 ± .09	159.6	0.27 ± .13

Table 6 cont.

A = 0.42 ± .03

$E_{c.m.}$ = 11.85 MeV

23.8°	1.77 ± .31 mb/sr
35.5	1.54 ± .24
47.0	1.27 ± .19
58.3	1.21 ± .25
69.3	1.09 ± .17
80.2	1.09 ± .23
90.8	1.01 ± .18
101.1	1.17 ± .26
111.0	1.06 ± .17
120.5	1.15 ± .25
129.6	1.07 ± .19
138.5	1.21 ± .27
147.1	1.20 ± .23
155.5	1.24 ± .24

A = 1.19 ± .07

A = 0.26 ± .015

E_{exc} = 7.5 - 10 MeV

27.2°	1.00 ± .22 mb/sr
40.5	0.79 ± .12
53.8	0.66 ± .10
66.4	0.67 ± .11
78.7	0.58 ± .12
90.3	0.43 ± .12
101.3	0.61 ± .16
111.6	0.73 ± .15
121.4	0.70 ± .14
130.2	0.67 ± .16
138.6	0.52 ± .09
146.3	0.54 ± .20
153.6	0.55 ± .20
160.7	0.53 ± .28

A = 0.65 ± .05

$E_{c.m.}$ = 11.85 MeV

24.3°	4.0 ± .7 mb/sr
36.3	3.5 ± .5
48.2	3.1 ± .5
59.7	3.1 ± .6
70.9	2.9 ± .4
81.7	2.9 ± .5
92.5	2.8 ± .5
102.6	2.9 ± .6
112.3	2.7 ± .4
121.7	2.9 ± .6
131.0	2.7 ± .4
139.8	2.9 ± .7
148.0	3.0 ± .5
156.3	3.1 ± .6

A = 3.00 ± .16

E_{exc} = 10 - 12.5 MeV

28.2°	2.7 ± .5 mb/sr
41.8	2.3 ± .3
55.3	1.8 ± .3
68.3	1.6 ± .3
81.0	1.6 ± .3
93.0	1.6 ± .3
103.9	1.5 ± .3
114.3	1.4 ± .3
123.6	1.6 ± .3
133.1	1.6 ± .3
140.7	1.5 ± .3
148.5	1.6 ± .4
155.4	1.9 ± .4
161.9	2.2 ± .5

A = 1.66 ± .10

Table 6 cont.

	$E_{c.m.}$ = 11.85 MeV	E_{exc} = 12.5 - 15 MeV	
25.3°	8.3 ± 1.4 mb/sr	29.3°	5.0 ± .8 mb/sr
37.3	7.2 ± 1.1	43.9	4.1 ± .6
49.7	6.5 ± .9	58.1	3.5 ± .6
61.7	6.6 ± 1.1	71.5	3.3 ± .5
73.2	6.1 ± .9	84.3	3.1 ± .5
83.7	6.5 ± 1.1	96.9	2.9 ± .5
94.9	5.9 ± .9	108.2	2.7 ± .5
105.7	6.4 ± 1.2	118.2	2.7 ± .5
114.8	6.2 ± .9	128.4	2.7 ± .5
124.2	6.5 ± 1.3	136.1	3.0 ± .4
133.2	6.5 ± .9		
141.9	6.7 ± 1.4		
149.7	6.7 ± 1.5		
157.7	6.9 ± 1.5		
	A = 6.5 ± .3		A = 3.14 ± .18

	$E_{c.m.}$ = 11.85 MeV	E_{exc} = 15 - 17.5 MeV	
26.8°	14.3 ± 2.1 mb/sr	31.4°	6.7 ± .9 mb/sr
40.7	13.1 ± 1.7	46.7	5.4 ± .8
52.6	12.4 ± 1.6	62.4	4.4 ± .6
66.0	10.8 ± 1.6	76.4	3.9 ± .6
77.6	10.5 ± 1.6	89.9	4.0 ± .6
89.3	10.3 ± 1.6	102.7	3.9 ± .6
100.6	10.0 ± 1.6	115.1	4.0 ± .6
111.3	9.9 ± 1.5		
119.7	9.8 ± 1.6		
129.4	9.5 ± 1.5		
137.0	8.4 ± 1.2		
145.1	10.6 ± 1.8		
152.8	10.4 ± 1.7		
160.1	9.9 ± 1.7		
	A = 10.6 ± .5		A = 4.1 ± .4 *

* 4 parameter fit

Table 6 cont.

$E_{c.m.}$ = 9.85 MeV		E_{exc} = 0 - 5 MeV	
23.1°	0.075 ± .010 mb/sr	25.7°	0.033 ± .004 mb/sr
28.6	0.070 ± .010	32.0	0.027 ± .004
34.5	0.054 ± .008	38.5	0.019 ± .003
45.7	0.064 ± .008	50.7	0.030 ± .004
67.4	0.041 ± .006	74.4	0.010 ± .002
88.4	0.041 ± .006	96.6	0.016 ± .003
108.5	0.035 ± .009	116.9	0.015 ± .007
127.3	0.053 ± .011	134.3	0.029 ± .011
145.4	0.069 ± .013	150.7	0.035 ± .011
154.2	0.082 ± .012	158.3	0.033 ± .006
	A = 0.057 ± .0045		A = 0.020 ± .003 *

$E_{c.m.}$ = 9.85 MeV		E_{exc} = 5 - 7.5 MeV	
23.4°	0.144 ± .019 mb/sr	26.5°	0.140 ± .018 mb/sr
29.0	0.130 ± .019	33.0	0.105 ± .014
34.9	0.128 ± .018	39.5	0.076 ± .010
46.4	0.123 ± .016	52.2	0.043 ± .005
68.4	0.104 ± .015	76.5	0.056 ± .008
89.8	0.095 ± .015	98.8	0.049 ± .008
109.7	0.099 ± .019	118.8	0.030 ± .011
128.5	0.103 ± .021	136.4	0.055 ± .020
146.4	0.110 ± .023	152.2	0.101 ± .028
154.9	0.125 ± .021	159.5	0.088 ± .018
	A = 0.114 ± .007		A = 0.052 ± .005 *

* 3 parameter fit

Table 6 cont.

	$E_{c.m.}$ = 9.85 MeV		E_{exc} = 7.5 - 10 MeV
23.8°	0.39 ± .05 mb/sr	27.2°	0.215 ± .028 mb/sr
29.5	0.34 ± .05	33.9	0.202 ± .027
35.6	0.33 ± .05	40.6	0.149 ± .021
47.1	0.34 ± .04	53.7	0.194 ± .024
69.7	0.30 ± .04	78.5	0.136 ± .022
90.9	0.30 ± .05	101.2	0.110 ± .025
111.1	0.29 ± .05	121.2	0.116 ± .026
129.5	0.31 ± .06	138.0	0.166 ± .053
147.1	0.32 ± .06	153.6	0.123 ± .034
155.6	0.34 ± .05	160.5	0.119 ± .022
	A = 0.333 ± .018		A = 0.146 ± .014

	$E_{c.m.}$ = 9.85 MeV		E_{exc} = 10 - 12.5 MeV
24.5°	0.90 ± .11 mb/sr	28.2°	0.40 ± .05 mb/sr
30.3	0.80 ± .11	35.2	0.38 ± .05
36.6	0.78 ± .11	42.0	0.29 ± .04
48.4	0.81 ± .10	55.6	0.33 ± .04
71.4	0.75 ± .10	81.3	0.34 ± .06
93.0	0.76 ± .11	104.6	0.32 ± .06
113.2	0.71 ± .10	124.2	0.29 ± .05
131.6	0.78 ± .13	141.2	0.29 ± .07
148.3	0.83 ± .15		
156.5	0.86 ± .14		
	A = 0.80 ± .06		A = 0.318 ± .021

Table 6 cont.

	$E_{c.m.}$ = 9.85 MeV		E_{exc} = 12.5 - 15 MeV	
25.9°	1.85 ± .23	mb/sr	30.0°	0.60 ± .08 mb/sr
32.4	1.71 ± .23		44.7	0.44 ± .06
39.0	1.53 ± .20		58.9	0.46 ± .06
50.9	1.59 ± .19		86.0	0.46 ± .08
75.4	1.59 ± .20		109.8	0.41 ± .07
96.9	1.36 ± .18			
117.4	1.41 ± .22			
135.1	1.58 ± .29			
151.4	1.59 ± .29			
159.0	1.40 ± .22			
	A = 1.60 ± .11		A = 0.49 ± .03	

Table 6 cont.

$E_{c.m.}$ = 8.85 MeV E_{exc} = 0 - 5 MeV

22.9°	0.0074 ± .0017 mb/sr	25.5°	0.0086 ± .0012 mb/sr
28.5	0.0124 ± .0018	32.0	0.0045 ± .0008
34.3	0.0120 ± .0024	38.1	0.0055 ± .0013
45.5	0.0156 ± .0023	50.5	0.0030 ± .0005
56.5	0.0158 ± .0026	62.7	0.0028 ± .0007
67.4	0.0133 ± .0021	74.0	0.0018 ± .0004
77.9	0.0112 ± .0020	85.3	0.0019 ± .0006
88.4	0.0101 ± .0018	96.1	0.0019 ± .0005
98.5	0.0093 ± .0022	106.6	0.0022 ± .0009
117.8	0.0110 ± .0024	125.3	0.0035 ± .0015
136.5	0.0149 ± .0030	142.5	0.0037 ± .0012
145.4	0.0134 ± .0026	150.5	0.0060 ± .0017
154.2	0.0137 ± .0026	158.1	0.0077 ± .0020
	A = 0.0108 ± .0007		A = 0.0032 ± .0005

$E_{c.m.}$ = 8.85 MeV E_{exc} = 5 - 7.5 MeV

23.3°	0.030 ± .005 mb/sr	26.4°	0.0166 ± .0023 mb/sr
29.0	0.026 ± .004	32.9	0.0148 ± .0021
34.9	0.028 ± .005	39.3	0.0109 ± .0022
46.4	0.027 ± .004	52.0	0.0136 ± .0019
57.4	0.028 ± .004	64.4	0.0093 ± .0016
68.5	0.026 ± .004	76.2	0.0064 ± .0014
79.3	0.029 ± .005	87.8	0.0070 ± .0020
89.6	0.026 ± .005	98.6	0.0062 ± .0018
99.7	0.026 ± .006	108.8	0.0050 ± .0017
119.3	0.027 ± .006	127.8	0.0115 ± .0032
137.4	0.027 ± .006	144.4	0.0066 ± .0023
146.3	0.023 ± .004	152.0	0.0138 ± .0033
154.9	0.024 ± .005	159.5	0.0149 ± .0058
	A = 0.0263 ± .0018		A = 0.0102 ± .0015

Table 6 cont.

$E_{c.m.}$ = 8.85 MeV		E_{exc} = 7.5 - 10 MeV	
23.9°	0.075 ± .010 mb/sr	27.2°	0.043 ± .006 mb/sr
29.6	0.067 ± .009	33.9	0.048 ± .006
35.7	0.074 ± .012	40.5	0.030 ± .005
47.3	0.063 ± .008	53.6	0.026 ± .005
58.8	0.060 ± .009	66.3	0.030 ± .005
69.8	0.065 ± .009	78.6	0.027 ± .005
80.7	0.060 ± .009	90.0	0.030 ± .006
91.2	0.067 ± .009	101.3	0.029 ± .005
101.5	0.069 ± .011	111.6	0.029 ± .005
120.7	0.071 ± .013	130.3	0.019 ± .005
138.8	0.063 ± .011	146.2	0.024 ± .005
147.2	0.075 ± .014	153.7	0.020 ± .004
155.6	0.066 ± .014	160.5	0.026 ± .007
A = 0.067 ± .003		A = 0.0315 ± .0020	

$E_{c.m.}$ = 8.85 MeV		E_{exc} = 10 - 12.5 MeV	
24.7°	0.146 ± .019 mb/sr	28.4°	0.066 ± .010 mb/sr
30.7	0.134 ± .018	42.3	0.060 ± .009
36.8	0.148 ± .024	56.0	0.060 ± .009
49.1	0.133 ± .017	69.1	0.067 ± .010
60.5	0.131 ± .018	81.5	0.054 ± .008
72.2	0.124 ± .016	93.9	0.055 ± .009
83.2	0.125 ± .018	105.2	0.051 ± .009
93.8	0.122 ± .016	115.1	0.049 ± .008
104.0	0.135 ± .022	133.7	0.061 ± .010
123.2	0.138 ± .025		
140.5	0.145 ± .027		
148.6	0.142 ± .027		
156.9	0.135 ± .028		
A = 0.133 ± .007		A = 0.057 ± .006	

Table 6 cont.

	$E_{c.m.}$ = 8.85 MeV		E_{exc} = 12.5 - 15 MeV
26.9°	0.28 ± .04 mb/sr	30.5°	0.054 ± .008 mb/sr
39.7	0.26 ± .04	45.4	0.051 ± .007
52.3	0.23 ± .04	60.1	0.048 ± .007
64.8	0.22 ± .03	74.1	0.047 ± .007
77.0	0.21 ± .03	87.6	0.049 ± .007
88.6	0.22 ± .03	100.8	0.053 ± .008
99.0	0.21 ± .03	112.3	0.052 ± .009
109.2	0.19 ± .03		
128.7	0.20 ± .03		
145.4	0.20 ± .03		
152.4	0.20 ± .03		
	A = 0.226 ± .012		A = 0.050 ± .003

Table 6 cont.

$E_{c.m.}$ = 7.85 MeV		E_{exc} = 0 - 5 MeV	
22.8°	0.00151 ± .00023 mb/sr	25.3°	0.00058 ± .00011 mb/sr
34.1	0.00182 ± .00034	37.9	0.00038 ± .00012
45.4	0.00088 ± .00018	50.1	0.00054 ± .00012
67.1	0.00117 ± .00023	73.8	0.00030 ± .00008
88.3	0.00128 ± .00024	96.0	0.00033 ± .00011
108.0	0.00117 ± .00041	116.1	0.00047 ± .00026
127.1	0.00131 ± .00046	133.5	0.00038 ± .00026
145.2	0.00179 ± .00055	150.1	0.00061 ± .00034
154.1	0.00189 ± .00056	158.0	0.00046 ± .00029
A =	0.00127 ± .00010	A =	0.00040 ± .00014

$E_{c.m.}$ = 7.85 MeV		E_{exc} = 5 - 7.5 MeV	
24.8°	0.0032 ± .0005 mb/sr	26.3°	0.0010 ± .0002 mb/sr
36.8	0.0036 ± .0007	39.2	0.0010 ± .0002
49.0	0.0028 ± .0005	52.0	0.0011 ± .0002
73.3	0.0024 ± .0004	76.1	0.0013 ± .0003
93.9	0.0028 ± .0005	98.2	0.0015 ± .0003
113.9	0.0027 ± .0008	118.4	0.0007 ± .0004
132.8	0.0030 ± .0011	136.1	0.0006 ± .0004
149.3	0.0032 ± .0009	151.9	0.0005 ± .0003
157.3	0.0029 ± .0009	159.3	0.0004 ± .0003
A =	0.0030 ± .0003	A =	0.0013 ± .0002 *

$E_{c.m.}$ = 7.85 MeV		E_{exc} = 7.5 - 10 MeV	
23.3°	0.0066 ± .0009 mb/sr	27.1°	0.0032 ± .0005 mb/sr
34.9	0.0086 ± .0016	40.6	0.0027 ± .0004
46.2	0.0064 ± .0010	53.5	0.0025 ± .0004
68.4	0.0068 ± .0011	78.2	0.0027 ± .0006
89.6	0.0070 ± .0011	101.2	0.0024 ± .0005
109.5	0.0065 ± .0016	121.1	0.0023 ± .0008
128.4	0.0077 ± .0022	138.3	0.0012 ± .0007
146.2	0.0058 ± .0016	153.4	0.0017 ± .0007
154.8	0.0057 ± .0017	160.5	0.0027 ± .0009
A =	0.0067 ± .0005	A =	0.0026 ± .0003

* 3 parameter fit

Table 6 cont.

$E_{c.m.}$ = 7.85 MeV		E_{exc} = 10 - 12.5 MeV	
23.7°	0.0135 ± .0018 mb/sr	28.5°	0.0049 ± .0007 mb/sr
35.5	0.0158 ± .0026	42.6	0.0040 ± .0006
47.2	0.0129 ± .0018	56.2	0.0045 ± .0007
69.8	0.0124 ± .0018	81.5	0.0039 ± .0007
91.2	0.0128 ± .0019	104.9	0.0033 ± .0006
111.3	0.0126 ± .0026	125.5	0.0044 ± .0011
130.0	0.0125 ± .0029		
147.4	0.0132 ± .0027		
155.7	0.0143 ± .0033		
A =	0.0133 ± .0010	A =	0.0036 ± .0007

$E_{c.m.}$ = 7.85 MeV		E_{exc} = 12.5 - 15 MeV	
		31.2°	0.0021 ± .0004 mb/sr
		46.6	0.0015 ± .0003
		61.6	0.0016 ± .0003
		A =	0.0017 ± .0004

Table 6 cont.

$E_{c.m.}$ = 9.35 MeV E_{exc} = 0 - 5 MeV

23.0°	0.052 ± .007 mb/sr	25.6°	0.014 ± .002 mb/sr
45.4	0.046 ± .007	50.6	0.008 ± .002
67.3	0.039 ± .006	74.4	0.014 ± .003
88.2	0.034 ± .006	96.3	0.018 ± .004
A = 0.042 ± .003		A = 0.0117 ± .0010	

$E_{c.m.}$ = 9.35 MeV E_{exc} = 5 - 7.5 MeV

23.4°	0.082 ± .011 mb/sr	26.4°	0.049 ± .006 mb/sr
46.3	0.071 ± .012	52.1	0.039 ± .006
68.5	0.066 ± .011	76.5	0.045 ± .007
89.7	0.064 ± .011		
A = 0.071 ± .006		A = 0.044 ± .009	

$E_{c.m.}$ = 9.35 MeV E_{exc} = 7.5 - 10 MeV

23.8°	0.23 ± .03 mb/sr	27.1	0.100 ± .013
47.2	0.21 ± .03	53.6	0.111 ± .016
69.6	0.21 ± .03		
91.2	0.19 ± .03		
A = 0.209 ± .015		A = 0.105 ± .021	

$E_{c.m.}$ = 9.35 MeV E_{exc} = 10 - 12.5 MeV

24.7°	0.46 ± .06 mb/sr
48.7	0.41 ± .06
71.8	0.39 ± .06
93.3	0.37 ± .05
A = 0.41 ± .03	

$E_{c.m.}$ = 9.35 MeV E_{exc} = 12.5 - 15 MeV

26.5°	0.90 ± .11 mb/sr
52.2	0.84 ± .12
A = 0.86 ± .17	

Table 6 cont.

$E_{c.m.}$ = 8.35 MeV E_{exc} = 0 - 5 MeV

22.9°	0.0051 ± .0008 mb/sr	25.6°	0.0016 ± .0003 mb/sr
45.3	0.0044 ± .0009	50.4	0.0009 ± .0003
66.8	0.0040 ± .0009	74.0	0.0013 ± .0004
88.2	0.0043 ± .0009		
A =	0.0045 ± .0005	A =	0.0013 ± .0003

$E_{c.m.}$ = 8.35 MeV E_{exc} = 5 - 7.5 MeV

23.3°	0.0095 ± .0014 mb/sr	26.4°	0.0032 ± .0005 mb/sr
46.3	0.0098 ± .0017	51.9	0.0052 ± .0010
68.2	0.0099 ± .0018		
89.5	0.0072 ± .0014		
A =	0.0089 ± .0008	A =	0.0042 ± .0010

$E_{c.m.}$ = 8.35 MeV E_{exc} = 7.5 - 10 MeV

23.8°	0.026 ± .004 mb/sr	27.2°	0.015 ± .002 mb/sr
47.2	0.025 ± .004		
69.8	0.023 ± .004		
90.9	0.024 ± .004		
A +	0.025 ± .002		

$E_{c.m.}$ = 8.35 MeV E_{exc} = 10 - 12.5 MeV

24.5°	0.053 ± .007 mb/sr
49.0	0.047 ± .007
72.3	0.045 ± .007
94.0	0.046 ± .007
A =	0.048 ± .005

Table 6 cont.

$E_{c.m.}$ = 7.32 MeV		E_{exc} = 0 - 5 MeV	
22.7°	0.00019 ± .00004 mb/sr	25.3°	0.00012 ± .00002 mb/sr
45.2	0.00020 ± .00004	50.0	0.00009 ± .00002
66.9	0.00009 ± .00003	73.6	0.00014 ± .00004
A =	0.00015 ± .00006	A =	0.00011 ± .00003

$E_{c.m.}$ = 7.32 MeV		E_{exc} = 5 - 7.5 MeV	
23.2°	0.00040 ± .00007 mb/sr	26.2°	0.00037 ± .00006 mb/sr
46.5	0.00029 ± .00005	51.7	0.00024 ± .00004
68.5	0.00033 ± .00008		
A =	0.00033 ± .00007	A =	0.00028 ± .00009

$E_{c.m.}$ = 7.32 MeV		E_{exc} = 7.5 - 10 MeV	
23.8°	0.00102 ± .00014 mb/sr	27.1°	0.00028 ± .00005 mb/sr
47.3	0.00074 ± .00012	53.3	0.00032 ± .00006
69.9	0.00102 ± .00018		
A =	0.00088 ± .00018	A =	0.00030 ± .00006

$E_{c.m.}$ = 7.32 MeV		E_{exc} = 10 - 12.5 MeV	
25.1°	0.00161 ± .00022 mb/sr	28.4°	0.00032 ± .00005 mb/sr
49.5	0.00132 ± .00019	56.5	0.00028 ± .00006
73.2	0.00191 ± .00030		
A =	0.00153 ± .00038	A =	0.00030 ± .00006

Table 6 cont.

$E_{c.m.}$ = 6.80 MeV		E_{exc} = 0 - 5 MeV	
22.7°	0.000028 ± .000009 mb/sr	25.2°	0.000015 ± .000005 mb/sr
45.2	0.000017 ± .000006	49.8	0.000008 ± .000004
A =	0.000021 ± .000007	A =	0.000010 ± .000005

$E_{c.m.}$ = 6.80 MeV		E_{exc} = 5 - 7.5 MeV	
23.2°	0.000045 ± .000011 mb/sr	26.1°	0.000023 ± .000007 mb/sr
46.1	0.000020 ± .000008	51.5	0.000014 ± .000005
A =	0.000028 ± .000017	A =	0.000017 ± .000006

$E_{c.m.}$ = 6.80 MeV		E_{exc} = 7.5 - 10 MeV	
23.9°	0.000066 ± .000014 mb/sr	27.0°	0.000036 ± .000008 mb/sr
47.2	0.000060 ± .000015	53.2	0.000037 ± .000009
A =	0.000063 ± .000013	A =	0.000036 ± .000007

$E_{c.m.}$ = 6.80 MeV		E_{exc} = 10 - 12.5 MeV	
25.2°	0.000147 ± .000024 mb/sr	28.7°	0.000017 ± .000005 mb/sr
49.5	0.000106 ± .000023	56.6	0.000021 ± .000006
A =	0.000125 ± .000022	A =	0.000019 ± .000004

Table 6 cont.

(Deuterons)

$E_{c.m.}$ = 11.85 MeV E_{exc} = 0 - 7 MeV

35°	0.348 ± .008 mb/sr
56	0.324 ± .010
82	0.342 ± .010

A = 0.34 ± .07

$E_{c.m.}$ = 9.85 MeV E_{exc} = 0 - 5 MeV

34°	0.0565 ± .0018 mb/sr
54	0.0485 ± .0016
80	0.0516 ± .0018

A = 0.052 ± .010

Table 7

Total Production Cross Sections for Charged Particles.

The total cross sections for intervals in excitation energy are taken from Table 6. The method for determining the extrapolated cross section is described on page 103 of the text. σ_{tot} is the total production cross section obtained by evaluating the data in the C.M. frame. σ_{lab} is the total production cross section from Table 8 (obtained by evaluating the data in the Lab frame). All errors are total errors; thus, the error on σ_{tot} is not just the square root of the sum of the squares of the errors in the columes above it. All cross sections are in mb.

				PROTONS				
E_{exc}	E_{cm} = 11.85 MeV	9.85	9.35	8.85	8.35	7.85	7.32	6.80
0-5 MeV	1.8 ± .3	.72 ± .12	.53 ± .09	0.136 ± .023	0.056 ± .010	0.016 ± .003	0.0019 ± .0008	0.00026 ± .00010
5-7.5	5.3 ± .9	1.44 ± .23	.89 ± .15	0.33 ± .06	0.112 ± .020	0.037 ± .007	0.0041 ± .0010	0.00035 ± .00022
7.5-10	15.0 ± 2.4	4.2 ± .7	2.6 ± .5	0.84 ± .13	0.31 ± .05	0.084 ± .014	0.0111 ± .0028	0.00079 ± .00020
10-12.5	38 ± 6	10.1 ± 1.7	5.1 ± .9	1.68 ± .27	0.60 ± .10	0.167 ± .028	0.019 ± .006	0.0016 ± .0004
12.5-15	81 ± 13	20 ± 3	10.9 ± 2.7	2.8 ± .5				
15-17.5	133 ± 21							
SUM	274 ± 42	36.5 ± 5.7	20.0 ± 3.7	5.83 ± .89	1.08 ± .17	0.304 ± .048	0.0363 ± .0077	0.00297 ± .00060

Table 7 cont.

PROTONS

	E_{cm} = 11.85 MeV	9.85	8.85	7.85	7.32	6.80
SUM	274 ± 42 mb	36.5 ± 5.7	5.83 ± .89	0.304 ± .048	0.0363 ± .0077	0.00297 ± .00060
EXTRAP.	38 ± 13	12.8 ± 2.9	0.73 ± .20	0.16 ± .03	0.009 ± .004	0.0007 ± .0003
σ_{tot}	310 ± 44	49 ± 6	6.6 ± 1.0	0.46 ± .08	0.045 ± .010	0.0037 ± .0008
σ_{lab}	310 ± 47	45 ± 7	6.4 ± 1.0	0.45 ± .07		
Adopted Value	310 ± 50 mb	47 ± 7	6.5 ± 1.0	0.46 ± .08	0.045 ± .010	0.0037 ± .0008

Table 7 cont.

ALPHAS

E_{exc}	E_{cm} = 11.85 MeV	9.85	9.35	8.85	8.35	7.85	7.32	6.80
0-5 MeV	1.09 ± .19	0.26 ± .05	0.147 ± .025	0.040 ± .009	0.016 ± .005	0.0049 ± .0019	0.0014 ± .0004	0.00013 ± .00006
5-7.5	3.3 ± .5	0.66 ± .12	0.55 ± .14	0.128 ± .027	0.052 ± .014	0.017 ± .003	0.0035 ± .0012	0.00022 ± .00008
7.5-10	8.1 ± 1.4	1.8 ± .3	1.3 ± .3	0.40 ± .07	0.19 ± .05	0.032 ± .006	0.0037 ± .0010	0.00045 ± .00010
10-12.5	21 ± 3	4.0 ± .7		0.72 ± .14		0.045 ± .011	0.0038 ± .0010	0.00024 ± .00006
12.5-15	39 ± 6	6.2 ± 1.0		0.63 ± .10		0.021 ± .006		
15-17.5	51 ± 9							
SUM	124 ± 20	13.0 ± 2.0		1.91 ± .30		0.120 ± .021	0.0124 ± .0025	0.00104 ± .00020

Table 7 cont.

ALPHAS

	E_{cm} = 11.85 MeV	9.85	8.85	7.85	7.32	6.80
SUM	124 ± 20 mb	13.0 ± 2.0	1.91 ± .30	0.120 ± .021	0.0124 ± .0025	0.00104 ± .00020
EXTRAP.	25 ± 5	4.6 ± 1.1	0.40 ± .10	0.033 ± .010	0.0045 ± .0015	0.00008 ± .00008
σ_{tot}	149 ± 24	17.6 ± 2.9	2.31 ± .38	0.153 ± .028	0.0169 ± .0034	0.00112 ± .00023
σ_{lab}	152 ± 24	15.9 ± 2.5	2.17 ± .34	0.132 ± .021		
Adopted Value	150 ± 25	17 ± 3	2.2 ± .4	0.14 ± .025	0.017 ± .0035	0.00112 ± .00023

Table 7 cont.

DEUTERONS

E_{exc}	E_{cm} = 11.85 MeV	9.85
0 - 5 MeV		0.65 ± .16 mb
0 - 7	4.3 ± 1.1 mb	
EXTRAP.	1.1 ± 1.1	0.10 ± .10
σ_{tot}	5.4 ± 1.5 mb	0.75 ± .18 mb

^3H and ^3He

E_{cm}	$\sigma(^3H)$ *	$\sigma(^3He)$ *
11.85 MeV	< 3 mb	< 6 mb
9.85	< 0.2	< 0.5
8.85	< 0.05	< 0.1
7.85	< 0.002	< 0.003

* Three standard deviation upper limits.

Table 8

Laboratory Differential Cross Sections for Charged Particle Production.

All errors listed are relative errors only (see page 104 of the text). The coefficient A of P_0 (cos θ) in a least squares fit to the angular distribution with Legendre polynomials is also given.

θ_{lab}	$\frac{d\sigma}{d\Omega})^{*}_{lab,p+d}$	$\frac{d\sigma}{d\Omega})^{*}_{lab,\alpha}$
	$E_{c.m.}$ = 11.85 MeV	
20°	55.8 ± .4 mb/sr	41.7 ± 1.4 mb/sr
30	47.7 ± .5	31.4 ± 1.3
40	40.5 ± .6	23.9 ± 1.5
50	35.1 ± .4	19.4 ± 1.1
60	31.0 ± .6	17.1 ± 1.9
70	27.6 ± .8	13.6 ± 1.8
80	24.4 ± .8	11.5 ± 2.0
90	21.5 ± .8	9.1 ± 2.1
100	18.8 ± .9	7.2 ± 2.1
110	16.8 ± 1.0	5.1 ± 1.5
120	13.5 ± .9	3.8 ± 1.4
120	14.8 ± .6	4.0 ± 1.4
130	14.5 ± .6	3.4 ± 1.2
140	13.6 ± .7	3.0 ± 1.2
150	12.8 ± .6	2.9 ± 1.2
	A = 24.8 ± 0.2	A = 12.2 ± 0.5

* The extrapolated counts are included in the calculation of these cross sections and the errors quoted.

Table 8 cont.

$E_{c.m.}$ = 9.85 MeV

20°	7.62 ± .16 mb/sr	3.79 ± .15 mb/sr
20	8.02 ± .08	3.97 ± .19
30	7.04 ± .18	3.17 ± .19
30	6.13 ± .14	2.68 ± .23
30	5.52 ± .12	2.37 ± .19
40	6.36 ± .19	2.56 ± .21
40	5.92 ± .16	2.38 ± .23
60	4.91 ± .19	1.87 ± .13
80	3.58 ± .07	1.26 ± .18
100	2.81 ± .09	0.77 ± .16
120	2.44 ± .14	0.50 ± .13
140	2.03 ± .10	0.38 ± .13
150	1.90 ± .10	0.34 ± .13
150	1.80 ± .20	0.26 ± .10
	A = 3.58 ± .04	A = 1.26 ± .05

$E_{c.m.}$ = 8.85 MeV

20°	1.053 ± .027 mb/sr	0.432 ± .025 mb/sr
30	0.901 ± .037	0.392 ± .048
40	0.788 ± .023	0.325 ± .023
50	0.758 ± .018	0.309 ± .033
60	0.740 ± .060	0.256 ± .037
70	0.600 ± .021	0.220 ± .036
80	0.516 ± .013	0.171 ± .023
90	0.441 ± .015	0.136 ± .024
110	0.372 ± .016	0.100 ± .028
130	0.313 ± .016	0.066 ± .026
140	0.293 ± .016	0.044 ± .012
150	0.258 ± .017	0.051 ± .018
	A = 0.514 ± .006	A = 0.173 ± .008

Table 8 cont.

$E_{c.m.}$ = 7.85 MeV

20°	0.066* ± .019 mb/sr	0.0256 ± .0025 mb/sr
30	0.065* ± .014	0.0198 ± .0022
40	0.054* ± .010	0.0195 ± .0019
60	0.0456* ± .0044	0.0145 ± .0013
80	0.0361 ± .0015	0.0102 ± .0011
100	0.0291 ± .0015	0.0086 ± .0020
120	0.0251 ± .0015	0.0059 ± .0021
140	0.0207 ± .0013	0.0036 ± .0014
150	0.0206 ± .0014	0.0032 ± .0013
	A = 0.0362 ± .0016	A = 0.0105 ± .0006

* These values have such large errors because of the large number of Hydrogen recoils contaminating the spectra.

Table 9

Limits on the Reaction Cross Sections.

Limits for the reaction cross section for $^{16}O + ^{16}O$ to exit channels emitting alphas or protons are given. The upper limit is the production cross section. Lower limits were determined by counting all protons or alphas as coming from three body breakup reactions except those which were definitely from two body exit channels (see the text page 107). Typical total errors are 15 - 20 %.

E_{cm} = 11.85 MeV	9.85	8.85	7.85
Protons			
Upper Limit	312 mb	45.0 mb	6.45 mb	0.455 mb
Lower Limit I	160	23.7	3.57	.261
Lower Limit II	161	24.0	3.59	.270
Alphas			
Upper Limit	153	15.9	2.17	.132
Lower Limit I	92	10.8	1.63	.112
Lower Limit II	93	11.0	1.66	.115

Table 10

Total Cross Section for $^{16}O + ^{12}C \rightarrow n + ^{27}Si$.

Cross sections and total errors for $^{16}O + ^{12}C \rightarrow n + ^{27}Si$ were determined using the activation method (see the Activation Method Section). Energy losses have been subtracted and produce an overall uncertainty in the energy of ± 100 keV (lab).

$E_{^{16}O,lab}$	E_{cm}	$E_{\beta\ cutoff}$	$\sigma(^{27}Si)$
23.9 ± .1 MeV	10.24 ± .04 MeV	0.5 MeV	36 ± 7 mb
21.9	9.38	.5	29 ± 6
19.9	8.53	.5	16 ± 3
"	"	"	19 ± 4
"	"	.8	19 ± 4
18.9	8.10	.5	10.4 ± 2.1
17.9	7.67	.5	7.5 ± 1.5
16.9	7.24	.5	2.8 ± .6
15.9	6.81	.5	1.23 ± .27
14.9	6.39	.5	0.36 ± .09
13.9	5.96	.5	0.084 ± .021
12.9	5.53	.5	0.016 ± .005

Table 11

Total Cross Sections for the Production of ^{31}S and ^{30}P.

Cross sections and total errors for the production of ^{31}S and ^{30}P by $^{16}O + ^{16}O$ reactions were determined using the activation method (see the Activation Method Section). Energy losses have been subtracted and produce an uncertainty in the energy of each point of ± 50 keV (C.M.). The average cross sections are plotted in Figures 34 and 35.

		Individual Runs + Relative Errors		Averages + Total Errors	
E_{cm}	$E_{\beta\ cutoff}$	$\sigma(^{31}S)$	$\sigma(^{30}P)$	$\sigma(^{31}S)$	$\sigma(^{30}P)$
12.00 MeV	0.5 MeV	6.5 ± 1.1 mb	69 ± 11 mb	6.5 ± 1.4 mb	69 ± 14mb
11.98	1.4	6.7 ± 1.5	83 ± 17	6.7 ± 1.7	83 ± 19
11.96	1.3	5.0 ± 1.2	51 ± 10	5.0 ± 1.3	51 ± 12
11.95	.7	6.3 ± 1.6	95 ± 19	5.5 ± .7	63 ± 9
"	.5	6.0 ± 1.2	60 ± 10		
"	.5	4.7 ± 1.3	64 ± 10		
"	.5	5.5 ± 1.1	72 ± 12		
"	.4	-	59 ± 9		
"	.5	-	58 ± 9		
"	2.0	-	61 ± 15		
11.93	1.8	6.3 ± 1.6	91 ± 22	6.0 ± 1.1	70 ± 13
"	.3	5.9 ± 1.0	66 ± 10		
11.92	1.4	6.5 ± 1.4	69 ± 14	6.5 ± 1.6	69 ± 16
9.96	1.3	1.9 ± .4	7.6 ± 1.5	1.9 ± .5	7.6 ± 1.7
9.95	.4	-	8.2 ± 1.3	-	7.6 ± 1.2
"	1.1	-	7.0 ± 1.4		
"	2.0	-	7.4 ± 1.8		
9.92	.6	2.6 ± .5	8.8 ± 1.8	2.6 ± .6	8.8 ± 2.0

Table 11 cont.

E_{cm}	E_{β} cutoff	$\sigma(^{31}S)$	$\sigma(^{30}P)$	$\sigma(^{31}S)$	$\sigma(^{30}P)$
8.97 MeV	1.4 MeV	0.72 ± .18mb	1.4 ± .3 mb	0.72 ± .20 mb	1.4 ± .4
8.96	1.3	0.42 ± .16	0.9 ± .2	0.42 ± .17	1.0 ± .2
"	1.3	-	1.1 ± .2		
8.95	.4	-	1.2 ± .2	-	1.2 ± .2
8.91	1.4	0.67 ± .16	1.2 ± .3	0.63 ± .13	0.9 ± .2
"	1.3	0.59 ± .15	0.8 ± .2		
8.45	.5	0.11 ± .06	0.47 ± .09	0.11 ± .06	0.25 ± .10[a]
"	1.1	-	0.20 ± .05		
"	2.0	-	0.25 ± .07		
8.41	1.3	0.14 ± .04	0.20 ± .05	0.14 ± .04	0.20 ± .08[a]
"	1.3	0.15 ± .06	0.20 ± .05		
8.05	2.0	-	0.10 ± .03	-	0.07 ± .05[a]
			0.06 ± .02[b]		
			0.07 ± .02[c]		
7.95	.8	0.034 ± .018	0.091 ± .026	0.034 ± .018	<0.09[a]
"	1.1	0.037 ± .033	0.054 ± .015		
7.91	1.3	0.041 ± .017	0.039 ± .012	0.041 ± .018	<0.06[a]
7.45	.8	-	0.023 ± .008	0.019 ± .016	-
"	1.1	0.019 ± .016	0.010 ± .003		
7.41	1.3	0.011 ± .009	0.004 ± .003	0.011 ± .009	-

a) Variation in the cross section with the beta cutoff energy gives uncertain results. See the text page 139.

b) Same data analyzed with a contaminant of halflife 400 sec.

c) Same data analyzed with a contaminant of halflife 1200 sec.

Table 12

Angular Distribution of Neutrons at E_{cm} = 11.95 MeV.

All errors are relative errors. In addition there is a 20 % error associated with the monitor counter solid angle, the relative efficiency of the long counter, and the elastic scattering cross section on all points (see page 147 of the text).

θ_{lab}	$\frac{N}{NMON}$	$\left(\frac{d\sigma}{d\Omega}\right)_{lab}$ flat res.	Correction Factor	$\left(\frac{d\sigma}{d\Omega}\right)_{lab}$ corr.
0°	0.0373 ± .0028	10.7 ± .8 mb/sr	1.041	11.1 ± .8 mb/sr
28°	0.0294 ± .0030	8.4 ± .9	1.041	8.8 ± .9
45°	0.0272 ± .0019	7.8 ± .6	1.042	8.1 ± .6
90°	0.0135 ± .0012	3.9 ± .4	1.039	4.0 ± .4
130°	0.0096 ± .0011	2.8 ± .3	1.039	2.9 ± .3

Table 13

Differential Cross Sections for $^{16}O + {}^{16}O \rightarrow {}^{12}C + {}^{20}Ne$ at $E_{cm} = 11.95$ MeV.

$\theta\,{}^{12}C$, lab	$\theta\,{}^{20}Ne$, lab	θ_{cm}, ^{12}C	$\left(\frac{d\sigma}{d\Omega}\right)_{cm}$ ± Relative Error	
^{12}C (g. s.) +	^{20}Ne (g. s.)			
20.0°	43.0°	37.3°	0.25 ± .05 mb/sr	(18%)
25.0°	43.8°	46.5°	.53 ± .09	(17%)
30.0°	43.1°	55.7°	.66 ± .12	(18%)
35.0°	41.6°	64.9°	.24 ± .05	(19%)
40.0°	39.4°	73.9°	.13 ± .03	(21%)
45.0°	36.9°	82.9°	.78 ± .14	(18%)
50.0°	34.1°	91.7°	1.43 ± .23	(16%)
55.0°	31.2°	100.3°	.47 ± .08	(17%)
57.0°	30.0°	103.7°	.23 ± .04	(19%)
60.0°	28.2°	108.8°	.12 ± .03	(21%)
65.0°	25.2°	116.9°	.33 ± .06	(17%)
70.0°	22.2°	124.7°	.51 ± .09	(17%)
75.0°	19.4°	132.0°	.59 ± .10	(17%)
80.0°	16.7°	138.7°	.48 ± .09	(18%)
85.0°	14.3°	144.8°	.13 ± .03	(21%)
(spectrometer data)				
-	7.0°	162.8°	< 6.5	
^{12}C (g. s.) +	$^{20}Ne^*$ (1.63)			
40.8°	35.0°	79.4°	.07 ± .02	(29%)
^{12}C (g. s.) +	$^{20}Ne^*$ (4.25) and	$^{12}C^*$ (4.43) +	^{20}Ne (g. s.)	
44.5°	25.0°	99.9°	< .03	

Table 14

Best Fits to the $^{16}O + {}^{16}O \rightarrow {}^{12}C + {}^{20}Ne$ Angular Distributions at $E_{cm} = 11.95$ MeV.

L Values	χ^2	σ_{TOT} ± Fitted Error
0, 4	28	6.6 ± .4 mb
4, 8	32	7.4 ± .4
2, 4	46	7.9 ± .6
2, 4, 6	4.4	2.5 ± 6
0, 4, 10	4.4	7.8 ± .5
4, 8, 10	24.5	7.5 ± .5

Table 15

$^{16}O + ^{16}O$ Total Reaction Cross Sections.

All cross sections are given in mb and the errors on the measured cross sections are given in Tables 7 and 11. $\sigma_{II}(p)$ and $\sigma_{II}(\alpha)$ are the values of Lower Limit II from Table 9. The total cross sections are averages of σ_{lower} and σ_{upper} (see the text page 107 and Figure 41) and they are tabulated below. The errors on the total cross sections were estimated from the uncertainties in the three body reaction percentage, errors on the measured cross sections, and uncertainties in the extrapolated cross sections.

E_{cm}	$\sigma_{prod}(p)$	$\sigma_{II}(p)$	$\sigma_{prod}(\alpha)$	$\sigma_{II}(\alpha)$	$\sigma(^{30}P)$	$\sigma(^{31}S)$	$\sigma(C+Ne)$	$\sigma(^{3}H)$	$\sigma(^{3}He)$
11.85 MeV	310	161	150	93	58	5.7	10	< 3	< 6
9.85	47	24	17	11	6.6	1.9	1*	< .2	< .5
8.85	6.5	3.6	2.2	1.7	.82	.48	.2*	<.05	< .1
7.85	.46	.27	.14	.12	.03*	.029	.01*	<.002	<.003
7.32	.045		.017		.004*	.004*	.002*		
6.80	.0037		.0011		.0003*	.0003*	.0001*		

* Extrapolated or estimated cross sections (see the text page 169).

Table 15 cont.

E_{cm}	σ_{lower}	σ_{upper}	σ_{total}	$\frac{\sigma_{prod}(p)}{\sigma_{total}}$	$\frac{\sigma_{prod}(\alpha)}{\sigma_{total}}$	$\frac{\sigma_{prod}(n+d)}{\sigma_{total}}$	$\frac{\sigma_{3\ body}}{\sigma_{total}}$
11.85 MeV	328	476	400 ± 100 mb	.78	.38	.16	.34
9.85	45	67	56 ± 14	.84	.30	.15	.31
8.85	6.8	9.4	8.1 ± 2.0	.80	.27	.16	.26
7.85	.46	.64	0.55 ± .17	.84	.25	.11	.22
7.32		.068	0.060 ± .021	.75	.28	.13	.20*
6.80		.0052	0.0047 ± .0017	.79	.23	.13	.17*

* σ_{total} at two energies was obtained from σ_{upper} and the estimated values of the three body percentage.

Table 16

The Ratio of the Elastic Scattering to the Mott Scattering Cross Section for $^{12}C + ^{12}C$

Energy losses have been included, but there is an overall uncertainty in the c.m. energy scale of ± 50 KeV (c.m.) (See the text page 177 and figure 42).

E_{cm}	Ratio to Mott	E_{cm}	Ratio to Mott
3.89 ± .05 MeV	0.996 ± .007	6.54	.776 ± .014
4.14	1.000 ± .006	6.60	.701 ± .013
4.39	1.004 ± .005	6.64	.685 ± .006
4.64	.992 ± .007	6.66	.733 ± .014
4.89	1.007 ± .006	6.73	.808 ± .015
5.02	.996 ± .012	6.77	.753 ± .008
5.14	1.008 ± .007	6.79	.696 ± .013
5.27	.985 ± .009	6.85	.728 ± .014
5.33	1.002 ± .012	6.89	.723 ± .007
5.39	1.007 ± .007	6.91	.651 ± .013
5.46	1.021 ± .012	6.98	.506 ± .010
5.52	1.024 ± .007	7.02	.477 ± .006
5.58	.995 ± .008	7.04	.474 ± .010
5.64	.967 ± .006	7.10	.455 ± .009
5.71	.993 ± .008	7.14	.418 ± .005
5.77	1.012 ± .006	7.16	.424 ± .008
5.80	1.002 ± .012	7.23	.420 ± .008
5.83	1.004 ± .007	7.29	.356 ± .007
5.89	.940 ± .006	7.35	.358 ± .007
5.92	.937 ± .012	7.41	.317 ± .006
5.96	.937 ± .008	7.48	.265 ± .006
6.02	.959 ± .007	7.54	.267 ± .007
6.05	.981 ± .012	7.60	.281 ± .006
6.08	.977 ± .007	7.66	.298 ± .007
6.14	.938 ± .006	7.73	.400 ± .007
6.21	.914 ± .007	7.79	.422 ± .008
6.27	.914 ± .006	7.85	.461 ± .010
6.33	.985 ± .006	7.91	.417 ± .008
6.39	.939 ± .007	7.98	.402 ± .009
6.41	.930 ± .017		
6.46	.865 ± .012		
6.48	.845 ± .015		
6.52	.816 ± .012		

Table 17

The Ratio of the Elastic Scattering to the Rutherford Scattering Cross Section for $^{16}O + ^{12}C$.

Energy losses have been subtracted from the quoted energies and result in an overall uncertainty in the energy scale of ± 50 keV (C.M.) (see Appendix I).

$E_{^{16}O,lab}$	Ratios to Rutherford				
	$\theta_{cm} = 65^\circ$	70°	90°	116°	125°
12.77 MeV	1.005 ± .005	1.011 ± .007			1.015 ± .012
12.81			1.008 ± .018	1.037 ± .019	
13.27	.996 ± .003	.987 ± .007	1.000 ± .009	1.017 ± .009	.997 ± .008
13.77	1.004 ± .003	1.002 ± .012	.992 ± .009	1.002 ± .009	1.012 ± .008
13.81			1.011 ± .020	1.004 ± .021	
13.81			1.021 ± .018	.992 ± .019	
14.27	1.001 ± .003	1.000 ± .008	.997 ± .009	1.006 ± .009	1.005 ± .008
14.52	.993 ± .004	1.005 ± .008	.988 ± .009	.992 ± .009	.992 ± .008
14.77	1.002 ± .004	.999 ± .008	1.003 ± .009	.980 ± .009	.998 ± .008
14.81			.968 ± .015	.967 ± .016	
15.02	.999 ± .003	.995 ± .008	1.012 ± .009	1.004 ± .009	.993 ± .008
15.27	1.001 ± .004	1.001 ± .008	1.008 ± .009	.998 ± .010	.987 ± .008
15.52	1.002 ± .004	1.001 ± .008	1.001 ± .009	.988 ± .010	.982 ± .008
15.77	1.008 ± .004	1.011 ± .008	.994 ± .009	.990 ± .010	.980 ± .008
15.81			1.028 ± .018	1.014 ± .019	
16.02	1.000 ± .004	1.000 ± .008	.981 ± .009	.981 ± .010	.980 ± .008
16.27	1.004 ± .004	1.000 ± .008	.979 ± .009	.970 ± .009	.973 ± .008
16.52	1.007 ± .004	1.006 ± .008	.968 ± .009	.967 ± .010	.936 ± .008

Table 17 cont.

E_{lab}	65°	70°	90°	116°	125°
16.77 MeV	1.006 ± .004	1.007 ± .008	.964 ± .010	.968 ± .010	.927 ± .008
16.81			.964 ± .016	.985 ± .017	
17.02	1.005 ± .004	1.009 ± .008	.965 ± .009	.950 ± .010	.889 ± .008
17.27	1.006 ± .004	1.017 ± .008	.983 ± .010	.921 ± .010	.856 ± .008
17.52	1.007 ± .004	1.009 ± .008	.969 ± .010	.904 ± .009	.844 ± .008
17.77	1.009 ± .004	.992 ± .008	.934 ± .010	.898 ± .010	.821 ± .008
17.81			.960 ± .018	.846 ± .016	
18.02	1.017 ± .004	1.008 ± .009	.948 ± .010	.861 ± .009	.777 ± .008
18.27	1.006 ± .004	1.031 ± .009	.939 ± .010	.805 ± .009	.739 ± .008
18.52	1.007 ± .004	1.032 ± .009	.911 ± .010	.768 ± .009	.699 ± .007
18.77	1.010 ± .004	1.045 ± .009	.868 ± .009	.762 ± .009	.694 ± .007
18.81			.899 ± .015	.767 ± .015	
19.02	1.015 ± .004	1.039 ± .009	.872 ± .009	.732 ± .009	.653 ± .007
19.27	1.026 ± .004	1.027 ± .009	.843 ± .009	.643 ± .008	.573 ± .007
19.52	1.022 ± .004	1.043 ± .009	.837 ± .009	.624 ± .007	.581 ± .007
19.77	1.029 ± .004	1.034 ± .009	.760 ± .008	.637 ± .007	.548 ± .006
19.81			.761 ± .015	.578 ± .014	
20.02	1.026 ± .004	.999 ± .008	.773 ± .008	.576 ± .007	.530 ± .006
20.27	1.013 ± .004	1.001 ± .008	.757 ± .008	.540 ± .007	.510 ± .006
20.52	1.010 ± .004	1.015 ± .008	.715 ± .007	.495 ± .006	.424 ± .005
20.77	1.027 ± .004	1.014 ± .008	.699 ± .008	.449 ± .005	.381 ± .005
21.81			.601 ± .012	.244 ± .008	
23.81			.443 ± .009	.169 ± .006	

Table 18

$^{12}C + ^{12}C$ Gamma Yield as a Function of Energy.

The yield and relative error of γ's with energy $E_\gamma > 1.4$ MeV is normalized at $E_{cm} = 3.99$ MeV to the data of Patterson, Winkler and Zaidins (1969). The energies are corrected for losses in the gas and there is a ± 50 keV (C.M.) uncertainty in the energy scale associated with this correction (see Appendix II).

E_{cm}	Normalized Yield	E_{cm}	Normalized Yield
7.485 MeV	420 ± 4%	6.160 MeV	124 ± 4%
7.435	411 ± 4%	6.135	124 ± 4%
7.385	385 ± 4%	6.110	88.7 ± 4%
7.335	424 ± 4%	6.085	81.9 ± 4%
7.285	457 ± 4%	6.035	82.5 ± 4%
7.235	363 ± 4%	5.985	130 ± 4%
7.185	399 ± 4%	"	129 ± 4%
7.135	360 ± 4%	5.935	104 ± 4%
7.085	328 ± 4%	5.885	64.9 ± 4%
7.035	367 ± 4%	5.835	42.6 ± 4%
6.985	406 ± 4%	5.785	47.2 ± 4%
6.935	334 ± 4%	5.735	48.9 ± 4%
6.885	349 ± 4%	5.685	75.3 ± 4%
6.835	353 ± 4%	"	74.2 ± 4%
6.785	321 ± 4%	5.635	97.1 ± 4%
6.735	265 ± 4%	5.585	68.6 ± 4%
6.720	249 ± 4%	5.535	35.0 ± 5%
6.710	254 ± 4%	5.505	25.7 ± 4%
6.685	261 ± 4%	5.485	22.7 ± 5%
6.635	292 ± 4%	5.460	19.9 ± 4%
6.585	184 ± 4%	5.435	17.7 ± 5%
6.535	163 ± 4%	5.425	17.2 ± 4%
6.485	196 ± 4%	5.385	17.8 ± 5%
6.435	163 ± 4%	"	18.1 ± 5%
6.385	159 ± 4%	"	16.7 ± 4%
6.335	174 ± 4%	5.350	14.1 ± 4%
6.285	200 ± 4%	5.335	14.2 ± 5%
6.235	179 ± 4%	5.310	12.9 ± 4%
6.210	158 ± 4%	5.285	13.3 ± 5%
6.185	136 ± 4%	5.270	12.9 ± 4%

Table 18 cont.

E_{cm}	Normalized Yield
5.235 MeV	12.9 ± 5%
5.230	12.6 ± 4%
5.190	10.6 ± 4%
5.185	9.9 ± 5%
5.155	9.0 ± 4%
5.135	8.6 ± 5%
5.115	8.4 ± 4%
5.085	8.0 ± 5%
5.075	7.7 ± 4%
"	7.8 ± 4%
5.035	11.1 ± 4%
"	10.8 ± 5%
5.000	13.1 ± 4%
4.985	12.4 ± 5%
4.960	9.3 ± 4%
4.920	7.4 ± 4%
4.880	8.2 ± 4%
4.845	7.1 ± 4%
4.805	5.4 ± 5%
4.765	4.1 ± 5%
4.730	2.11 ± 5%
4.690	1.52 ± 5%
4.650	1.49 ± 5%
4.610	1.80 ± 5%
4.575	1.82 ± 5%
4.535	1.25 ± 5%
4.495	1.52 ± 5%
4.455	1.54 ± 5%
4.415	.91 ± 5%
4.375	.65 ± 5%
4.335 MeV	0.58 ± 5%
"	.58 ± 5%
4.300	.62 ± 5%
4.260	.54 ± 5%
4.220	.52 ± 5%
4.180	.369 ± 5%
4.145	.228 ± 5%
4.105	.148 ± 5%
4.065	.119 ± 5%
4.030	.113 ± 6%
3.990	.087 ± 6%
	(normalization point)
3.950	.052 ± 6%
3.910	.034 ± 6%
3.870	.0254 ± 7%
3.835	.0195 ± 7%
"	.0175 ± 7%
3.795	.0175 ± 7%
"	.0190 ± 7%
3.755	.0149 ± 7%
"	.0201 ± 7%
3.715	.0125 ± 7%
"	.0166 ± 7%
3.675	.0105 ± 7%